Olav Egaas Mortensen

Simulation of viscous flow around a curved cylinder in crossflow

Master's thesis in Marine Technology
Supervisor: Prof. Bjørnar Pettersen / Postdoc. Fengjian Jiang
June 2019

Master's thesis

NTNU
Norwegian University of
Science and Technology

Olav Egaas Mortensen

Simulation of viscous flow around a curved cylinder in crossflow

Master's thesis in Marine Technology
Supervisor: Prof. Bjørnar Pettersen / Postdoc. Fengjian Jiang
June 2019

Norwegian University of Science and Technology
Faculty of Engineering
Department of Marine Technology

NTNU
Norwegian University of
Science and Technology

MASTER THESIS IN MARINE HYDRODYNAMICS

SPRING 2019

FOR

Stud.techn. Olav Egaas Mortensen

SIMULATION OF VISCOUS FLOW AROUND A CURVED CYLINDER IN CROSSFLOW.

The candidate shall investigate viscous flow around a curved cylinder in crossflow using numerical simulation with FINE/Marine.
Initially a straight cylinder is going to be analyzed in order to investigate Reynolds number effects and effect of length of cylinder and boundary conditions. Different mesh configurations shall also be tested.
The main study will be with a curved cylinder in crossflow. Special focus should be on the computational domain, special symmetry conditions used and necessary length extensions of the curved cylinder part. The choice of Reynolds numbers, numerical parameters, boundary conditions and computational domain shall be documented. How the end-conditions influence the results must be detailed documented.
Visualization and documentation of the fluid flow results are important.

In the thesis the candidate shall present his personal contribution to the resolution of the problem within the scope of the thesis work. Theories and conclusions should be based on mathematical derivation and logic reasoning identifying the various steps in the deduction. The original contribution of the candidate and material taken from other sources shall be clearly defined. Work from other sources shall be properly referenced. The candidate should utilize the existing possibilities for obtaining relevant literature.
The thesis should be organized in a rational manner to give a clear exposition of results, assessments and conclusions. The text should be brief and to the point, with a clear language.

The thesis shall contain the following elements: A text defining the scope, preface, list of contents, summary, main body of thesis, conclusions with recommendations for further work, list of symbols and acronyms, references and appendices. All figures, tables and equations shall be numerated.
It is supposed that Department of Marine Technology, NTNU, can use the results freely in its research work by referring to the student's thesis.
The thesis shall be submitted June 11th, 2019.

Bjørnar Pettersen
Professor/supervisor

Co-supervisor: Postdoc Fengjian Jiang

Preface

This master thesis is the result of the work done during the spring term of 2019 as part of my M.Sc. degree in Marine Hydrodynamics at the Department of Marine Technology (IMT) at the Norwegian University of Science and Technology (NTNU).

The main motivation for my master thesis was to learn how to use computational fluid dynamics (CFD) as a research tool. As opposed to conventional approaches of solving hydrodynamic problems, CFD methods can capture nearly all fluid effects and non-linear flow features. This allows you to simulate real flow problems with very precise results. The idea of resolving all flow details and seeing what is actually going on within complex fluid problems was very appealing to me. The software FINE/Marine used in the present master thesis is specialized towards marine applications. Seeing that this software is being used by many of the researchers at both SINTEF and NTNU was reassuring for me in the choice of software, as well as the availability of guidance to follow up on my work. The present master thesis builds on the work done during the project thesis written during the fall of 2018, where I was first introduced to the FINE/Marine and performed simulations for some more fundamental flow cases.

The process of writing my master thesis has taught me a lot about conducting numerical research and writing a scientific report. As a beginner to working with CFD I have learned that this research tool requires patience, having faced several challenges along the way. All obstacles however lead to a better understanding of the both the numerical framework and the governing physics behind the flow problem under examination. Perseverance through the whole process has been a key trait, and the ultimate result and learning outcome is indeed very very rewarding.

Olav Egaas Mortensen
Trondheim, June 11, 2019

Acknowledgements

I would like to express my gratitude to my supervisor Professor Bjørnar Pettersen and my co-supervisor Postdoc. Fengjian Jiang for all the guidance and advice along the way. Our weekly meetings have been truly motivating and provided me with all the support I could ask for. I would also like to thank research scientist Eloïse Croonenborghs at SINTEF Ocean for software support and always being available and eager to help. At last I would like to thank my fellow students and friends in office C1.077 for good discussions and excellent company throughout the whole process in writing this master thesis.

Abstract

This master thesis presents numerical investigations of the three-dimensional viscous flow around a straight circular cylinder and a curved circular cylinder in cross-flow. Simulations have been prepared and executed in the Computational Fluid Dynamics (CFD) software FINE/Marine. Initial simulations of a straight cylinder were conducted in order to obtain experience in FINE/Marine with computational set-up of such flow problems, before performing simulations of more complex geometries. The main scope of the present thesis has been to provide preliminary characterizations of the transitional wake regime behind a curved circular cylinder in cross-flow. The work includes some recommendation for computational set-up for the present flow configuration, where emphasis has been on domain choice by application of straight extensions to the curved cylinder. The present analysis represent one of the first numerical studies that has been performed on this curved cylinder cross-flow configuration.

The straight cylinder simulations yielded results that were well in line with previous research on the field. Uniform inflow at Re = 200 and 300 is considered, revealing the characteristic transitional wake regimes of mode A and mode B within the respective simulations. Cylinder lengths of 4D, 8D and 12D were tested. The results showed that a spanwise length of 12D was clearly the preferred choice. Furthermore some variations in mesh configurations were discussed. The mesh resolution in the spanwise direction was found to successfully initiate three-dimensional flow features for even in the coarsest resolution that was adapted. The refinement level of the near wake region was found to be important in order to capture three-dimensional streamwise vortex formations, although the forces exerted to the cylinder were not sensitive to the size of the box refinements applied. Some discussion on choice of boundary conditions was provided.

The curved cylinder configuration consisted of a cylindrical quarter ring (torus) with a radius of curvature of 12.5 m and a diameter of 1 m subjected to an incoming flow perpendicular to the axis of curvature at Re = 200 and 300. The same distinctive transitional regimes of mode A and mode B were computed for the respective simulations also for this configuration. Mode B was more easy to initiate and appeared in a more uniform and stable manner, much like in the straight cylinder simulations. Mode A proved to be difficult to trigger. It is recommended to perform simulations with some perturbed initial conditions for this respective range of Reynolds numbers. Mode A vortex shedding also contained more features of instabilities in this curved cylinder cross-flow configuration, where frequent dislocations and changing patterns of oblique vortex shedding could be observed. A horizontal extension was provided in some of the simulations by application of spanwise lengths 8D and 16D respectively. The use of straight extension somewhat suppressed the amount of dislocations occurring during mode A. The extensions were also split into parts of 1 m lengths in order to monitor the forces exerted to the parts individually. An elevated drag force was measured on the curved cylinder compared to the straight extension. The drag forces on the curved body seemed to be reduced if extensions were enforced, more so by application of the 16D extension than the 8D extension. The curved cylinder also seem to have a lower vortex shedding frequency than the straight extension, which is believed to be connected to the occurrences of oblique vortex shedding. The described trends needs further investigation and longer simulation times to be further confirmed.

Abstrakt

Denne masteravhandlingen presenterer numeriske undersøkelser av den tredimensjonale viskøse strømningen rundt en rett sirkulær sylinder og en krum sirkulær sylinder i tverrstrøm. Simuleringer har blitt utarbeidet i programvaren FINE/Marine som utfører numeriske strømningsberegninger (CFD). Innledende simuleringer av en rett sylinder ble gjennomført for å få erfaring i bruken av FINE/Marine innen oppsett av slike strømningsproblemer, før simulering av mer komplekse geometrier kunne utføres. Hovedfokuset for denne avhandlingen har vært å gi foreløpige karakteriseringer av waken bak en krummet sirkulær sylinder i krysstrøm. Arbeidet inneholder anbefalinger for oppsett av denne type strømningsproblem, hvor det har blitt lagt vekt på valg av domene ved bruk av rette forlengelser til den buede sylinderen. Denne analysen representerer en av de første numeriske studiene som har blitt utført på en slik krum sylinder i tverrstrøm.

Simuleringene av en rett sylinder viste seg å gi resultater i tråd med tidligere forskning på feltet. Uniform innstrømning ved Re = 200 og 300 ble vurdert og avslørerte det karakteristiske overgangsgangsregimet av waken som i litteraturen er kjent mode A og mode B. Sylinderlengder av 4D, 8D og 12D ble testet. Resultatene viste at en lengde på 12D er foretrukne valget blant de som ble utprøvd. Videre ble noen variasjoner i grid-konfigurasjoner diskutert. Gridoppløsningen i på langs av sylinderen ble spesifikt undersøkt, hvor selv i den groveste blant de testede oppløsningene gav tredimensjonale strømnigsmønstre. Videre viste det seg at gridoppløsning av wake-området bak sylinderen er svært viktig for å fange de tredimensjonale strømningsformede virvelformasjoner, selv om kreftene som utøves på sylinderen ikke var nevneverdig følsomme for størrelsen på de anvendte gridstørrelsene. I tillegg inneholder rapporten noe diskusjon om valg av grensebetingelsers innvirking på strømningsmønsteret.

Den krumme sylinderkonfigurasjonen besto av en sylindrisk kvart ring (torus) med en krumningsradius på 12,5 m og en diameter på 1 m plassert i en innkommende strøm vinkelrett på krumningsaksen ved Re = 200 og 300. De samme karakteristiske overgangsregimene populært kalt mode A og modus B ble påvist i de respektive simuleringene også i disse simuleringene. Mode B var mer lett å framprovosere og dukket opp på en jevn og stabil måte, på samme måte som i simuleringene av en rett sylinder. Mode A viste seg å være vanskeligere å utløse. Det anbefales å utføre simuleringer med "forstyrrede" initialbetingelser for å få mode A til å oppstå. I tillegg viste det seg at waken i mode A innehar flere ustabile egenskaper i den krummede konfigurasjonen enn for den tilsvarende rette sylinderen. Hyppige dislokasjoner og varierende skrå virvelavløsning ble observert. En horisontal, rett forlengelse av henholdsvise lengder 8D og 16D ble inkludert i enkelte simuleringer. Bruken av slike rette forlengelser viste seg å undertrykke hyppigheten av forekomsten av dislokasjoner som oppstod under mode A. I tillegg ble de rette sylinderforlengelsene inndelt i deler på 1 m lengder for å overvåke kreftene som utøves på hver del individuelt. En noe forhøyet dragkraft ble målt på den krumme sylinderen i forhold til de rette forlengelsen. Dragkreftene på den buede sylinderen ser ut til å bli redusert dersom utvidelser blir brukt. Denne trenden var noe mer synlig ved anvendelse 16D-forlengelsen enn 8D-forlengelsen. Samtidig viser den krumme sylinderen seg å ha en generelt lavere virvelavløsningsfrekvens enn den rette forlengelsen. Ytterligere undersøkelser og lengre simuleringstider er nødvendig for å videre bekrefte de nevnte tendensene.

Contents

Nomenclature

Abbreviations

2D	Two Dimensional
3D	Three Dimensional
BC	Boundary Conditions
CV	Control Volume
FFT	Fast Fourier Transform
FDM	Finite Difference Method
FEM	Finite Element Method
FVM	Finite volume method
L	Laminar
lvl.ref.	Level of refinements
nb.	number
NS	Navier Stokes
ODE	Ordinary differential equations
PDE	Partial Differential Equations
PSD	Power Spectral Density
RANS	Reynolds Averaged Navier-Stokes
RMS	Root Mean Square
TrBL	Transition in Boundary Layers
TrSL	Transition in Shear Layers
TrW	Transition in Wake
VIV	Vortex Induced Vibrations

Symbollist

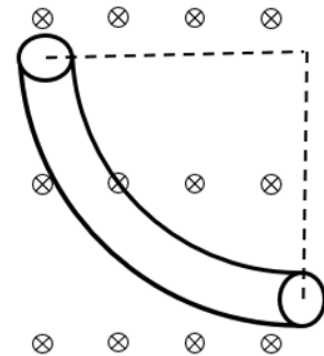|	
C_D	Drag coefficient
C_L	Lift coefficient
C_{pb}	Base pressure coefficient
$\Delta x_1,\ \Delta y_1,\ \Delta x_1$	Initial mesh size
f_0	Dominating frequency
L_E	Length of straight extension to curved cylinder simulation
L_Z	Length of cylinder in straight cylinder simulation
St	Strouhal number
Re	Reynolds number
p	Pressure (instantaneous)
u	Velocity component in x-direction (instantaneous)
v	Velocity component in y-direction (instantaneous)
w	Velocity component in z-direction (instantaneous)

1   Introduction

Exploration and exploitation of hydrocarbons is moving into locations of deeper water and harsher weather conditions. The offshore industry is in need of efficient riser solutions tailored for these rough conditions. There are many technical challenges to riser technology, one of them being vortex induced vibrations (VIV) and fatigue damage. VIV are produced by ocean currents flowing past the riser component, causing the phenomena of vortex shedding. This involves varying pressure gradients on the surface of the component which induces oscillating forces to the riser. If these oscillating forces have frequencies close to the natural frequency of the component, resonant motions of large amplitudes can occur leading to fatal fatigue and material damage. The three dimensional flow problem governing this phenomena is highly complex of nature. As of today there are still many questions that remains to be answered on the behaviour of fluid flow around risers governing the induction of vortex induced vibrations.

A common way to approach a practical engineering problems in research is to decompose it into simpler geometries. A basic model used to describe flows of this nature is the uniform flow past a straight circular cylinder. This configuration has already been widely studied in research, serving as a basis to understand flows around more complicated structures. In the context of flexible risers, the problem is well represented by the flow past a curved cylinder of circular cross-section. The curvature introduces significant complexity to flow regime. This configuration has received an increasing attention in research lately, but there are still many questions to be answered regarding this type of flow problem. Figure 1 illustrate a marine riser subjected to a current and how the geometry can be modeled to study the flow problem in detail.
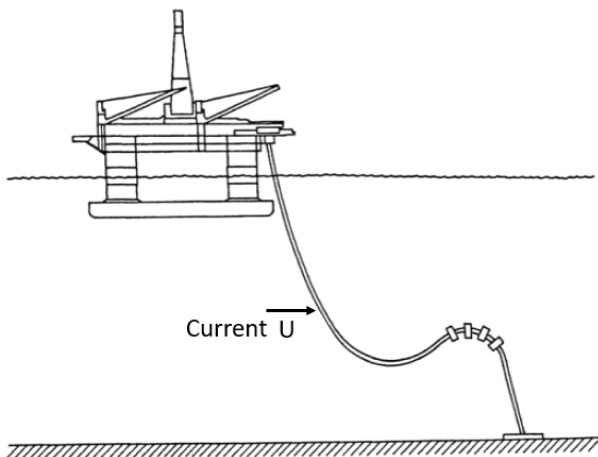
(a) Offshore unit with marine riser (Faltinsen [1990])   (b) Model of curved cylinder in cross flow

Figure 1: Marine riser subjected to a current and simplified riser geometries in cross flow

The scope of the master thesis work involves the study of both the above mentioned configurations, namely flow around a straight cylinder and curved cylinder in cross-flow. This is done by numerical simulations using the software FINE/Marine. There are many numerical parameters that require special attention and tuning in order to simulate the flow correctly. The straight cylinder simulations will involve investigation of different mesh and domain configurations, boundary conditions and effects of Reynolds numbers. These initial simulations will provide the groundwork for performing the more complex, curved cylinder simulations. The focus of these simulations will be to study the effect of curvature, special symmetry conditions and necessary length of straight extensions to the curved cylinder part, as well as some variations in Reynolds numbers. To clarify, the present analysis is performed on a rigid cylinder with no elastic properties. The development of the flow wake will be studied isolated, without the additional effects of a moving cylinder component.

The current simulations represent only a small fraction of the possible flow configurations that requires investigation in order to better understand the flow around curved cylinders. This master thesis can hopefully serve as a contribution to a wider resolution of the problem in all its complexity. The report also includes a presentation of the governing theoretical concepts behind the flow problems of said type, as well as a literature review on the existing research within the field of flow beyond straight and curved cylinders. The report is structured in the following manner:

- Section 2: Theoretical background. This chapter presents theoretical concepts on viscous fluid flow phenomena and numerical framework required in order to understand and interpret the results of the simulations. Important flow parameters are introduced to support the discussions to come in later stages of the report.

- Section 3: Literature review on what has been done within recent research on the field of flow around straight and curved cylinders, both in experimental and numerical studies.

- Section 4: Governing equations and numerical framework. Basic concepts and important aspects of CFD.

- Section 5: General guidelines to set-up of numerical simulations in FINE/Marine, choice of two dimensional mesh configuration, computational domain and time step.

- Section 6: Straight cylinder simulations set-up, results and discussions.

- Section 7: Curved cylinder simulations set-up, results and discussions.

- Section 8: Conclusions and summary of main findings, with suggestions to further work.

- Appendix: Additional figures and plots

The study of flow around circular cylinder is arguably best studied by flow visualization methods, plots and figures. To better illustrate key concepts occurring in the simulations, some flow-animations have been created and submitted along with the thesis. All simulations files, additional scripts in Matlab and Python, as well as the mentioned animations are exported to an external hard rive and delivered to my supervisor Bjørnar Pettersen for further work.

2   Theoretical background

2.1   Viscous flow

In the study of viscous fluid flow, several fluid properties are accounted for that otherwise are disregarded in conventional potential theory. As indicated by the name of this fluid theory, the effect of viscosity is included. Fluid viscosity introduces frictional effects leading to the phenomena known as no-slip. The no-slip condition involves that a fluid particle in direct contact with a physical wall will stick to it, meaning that all velocity components are equal zero at the surface of this wall. The velocity components will gradually develop moving away the wall and outwards through the fluid. This region close to the wall is called the boundary layer, and the form and behaviour is dependent on the flow properties. Separation is an important phenomena within the viscous world, where a fluid particle near a physical surface has a reversed velocity component and therefore separates from the face of the surface. Separation is the birthing place of what we regard as vortex shedding, leading to a vortex street in the wake of bluff bodies. Rotationality is also a feature of viscous fluid flow which is otherwise neglected in potential theory, allowing for the formation of such vortices. The flow around a circular cylinder exhibits all of the above mentioned flow features. Some further details and mathematical background on these viscous fluid flow phenomena are provided in the present section. This is included to communicate to the reader more efficiently, providing necessary terms and vocabulary required to discuss the observations and conclusions drawn from of the results from the upcoming CFD simulations.

2.2   Steady flow past a circular cylinder

When fluid flows towards a cylinder with a uniform velocity, the fluid domain surrounding the cylinder is affected by the presence of the cylinder. According to Zdravkovich [1997], the disturbed flow field can be divided into four main flow field regions: A narrow flow region in front of the cylinder with retarded flow velocity, a boundary layer region along the cylinder surface develops that eventually leads to separation, two sidewise regions of accelerated flow above and below the cylinder and a wide downstream region behind the cylinder called the wake. The development and characteristics of the flow regimes in these regions is dependent on the Reynolds number defined as

$$Re = \frac{\rho \cdot U \cdot D}{\mu} = \frac{U \cdot D}{\nu} \tag{1}$$

where U is the uniform flow velocity, D is a characteristic length of the geometry (the cylinder diameter) and ρ, μ and μ are density, dynamic and kinematic viscosity respectively. As the Reynolds number is increased starting from a low value, the flow starts as completely laminar, and then transitions to turbulence in different regions of the flow step by step. Other factors that will influence the development of the flow, which are often present in practical applications, are surface roughness, three-dimensional body form, free-surface effects, nearby walls such as sea bottom or other adjacent structures (Faltinsen [1990]). We will take a closer look at some of these influencing factors, for example the curvature in a three dimensional cylinder. Knowledge of flow regimes by Reynolds number around straight, smooth cylinders is nevertheless the starting point in order to investigate more complex variations to the flow and geometry set-up. The different flow states based on Reynolds number is described in detail in section 2.7.

2.3   Laminar and turbulent flow

In fluid mechanics there is a well known difference between laminar and turbulent flows. Laminar flows are smooth, predictable and flow in a streamwise manner, while turbulent flows are chaotic. It is common to distinguish the two flow states by magnitude of the Reynolds number. The characteristic length D in the definition of Reynolds number (see Equation 1) can be in general any geometrical parameter that represents the flow field. In the applications of flow around circular cylinder, we use the diameter of a cylinder, but D can also be the width of a pipe, the length of a ship hull or the length of a flat plate. In general, low Reynolds numbers are associated with laminar flows, while high Reynolds numbers describe turbulent flows.

Physically, laminar and turbulent flows exhibit very different behaviours and properties. Turbulent flow is characterized by the formation of so-called eddies, which are regions of swirling where the flow is rotation around as a centre. The fluid particles in turbulent flows experience velocity- and pressure fluctuations, which are deviations from the expected value of the velocity and pressure. These fluctuations arises from the acceleration term in the Navier-Stokes equations because of non-linear effects. Fluctuations are highly random and can only be expressed on a statistical basis, making it necessary to describe turbulence by empirical models rather than purely numerical approaches. In turbulent flows, there are a wide range of scales in length and time. Turbulent eddies are present at large and small scales, and energy is being transferred down to the smallest scales by means of an energy cascade Tennekes and Lumley [1972]. At the smallest scales, called Kolmogorov microscales, the kinetic energy in the eddies are transferred to internal heat energy through means of viscous dissipation. This means the effect of viscosity is highly important in turbulent flows. Knowledge about the properties of turbulence and the Kolmogorov microscales are relevant in the context of understanding why turbulence modelling is required in CFD computations of turbulent flows. The Kolmogorov microscales of length η, time τ and velocity v found by dimensional analysis and are given as

$$\eta = \left(\frac{\nu^3}{\epsilon}\right)^{1/4} \qquad \tau = \left(\frac{\nu}{\epsilon}\right)^{1/2} \qquad v = (\nu\epsilon)^{1/4} \qquad (2)$$

If we were to solve the Navier-Stokes equations for turbulent flows by direct numerical simulations (DNS), we would need a grid with very small cell sizes in order to resolve the smallest scales of turbulence. This means that the grid cell sizes would have to be smaller than η in the whole domain. The required computational power increases very rapidly as the Reynolds number increases, which is one of the reason why we need turbulence models in CFD computations. Some further insight on the different turbulence modelling approaches in CFD can be found in Section 4.

2.4   Boundary layers

Boundary layer is a phenomena arising in viscous fluid flow as the fluid experience a shear stress in close proximity of a wall due to the condition of no-slip. Boundary layers can be of both laminar and turbulent nature, which exhibit

different characteristics. An illustration of the transition of a laminar boundary layer to a fully turbulent boundary layer can be seen in figure 2.
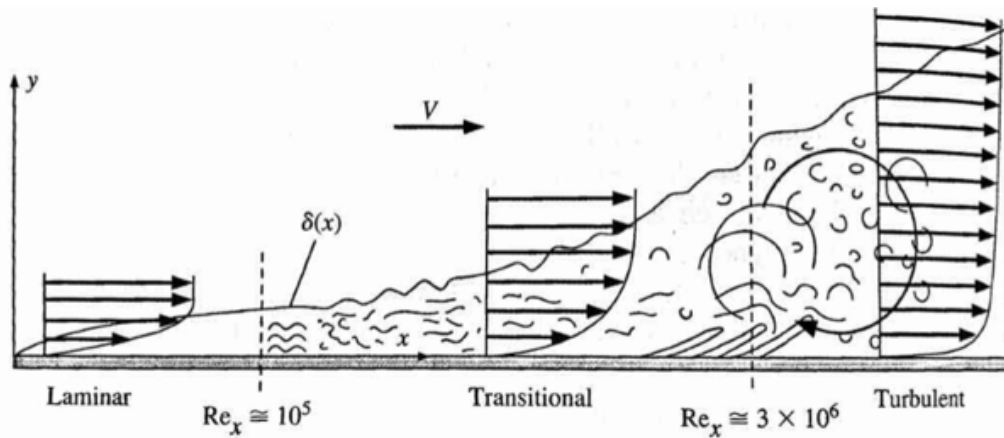

Figure 2: Transition from laminar- to turbulent boundary layer (Cengel [2014])

As we can see from the illustration above, the local Reynolds number Re_x is used to describe the location of where the boundary layer transitions from laminar to turbulent. Here, x is the position along the flat plate, and is in this context the characteristic length as described in Equation 1.

Knowledge of boundary layers are very important in CFD computations as it is necessary with fine enough grid close to surfaces to be able to resolve the boundary layer properly. In this section some approaches to derivation of laminar and turbulent boundary layers are presented. The essential part of the theory is to have some knowledge with the boundary layer thickness for surfaces with different geometries, in order to know how to create a mesh that resolve the boundary layer in CFD computations. For simplicity, the word boundary layer is in the following sometimes referred to as BL. It is important to note that the described boundary layer approximations were necessary to obtain flow solutions in the early 1900's in the absence of computers with strong computational power. Nowadays it is not necessary to divide the flow into an outer and inner flow region. Using CFD we solve the Navier-Stokes equations in the entire fluid. Nevertheless, the knowledge of boundary layer thickness and behaviour is critical with respect to meshing and understanding the characteristics of the flow.

Laminar boundary layer theory:

Ludwig Prandtl's was one of the pioneers within development of boundary layer theory, which was originally derived for flat plates. The common convention is to define the boundary layer thickness δ as the distance from the wall to the point in the flow where the velocity component is 99% of the velocity if the fluid outside the boundary layer (Cengel [2014]). For boundary layer theory to be valid, the local Reynolds number Re_x (see Figure 2) must be large. This comes from the assumption that the boundary layer is thin, $\delta \ll$ x. Prandtl derived boundary layer equations by simplifying the Navier-Stokes equations by an order-of-magnitude analysis or scaling analysis. This

involves comparing the terms of the equations to each other by orders of magnitude, in order to neglect terms minor terms based on assumptions and physical interpretations of the boundary layer. The order-of-magnitude analysis is an exercise that can be studied in detail in literature. The resulting equations for laminar boundary layer x- and y-momentum respectively are:

$$u\frac{\partial u}{\partial x} + v\frac{\partial u}{\partial y} = -\frac{1}{\rho}\frac{\partial p}{\partial x} + \nu\frac{\partial^2 u}{\partial y^2} \tag{3}$$

$$\frac{1}{\rho}\frac{\partial p}{\partial y} = 0 \tag{4}$$

The y-momentum equation (e.g Equation 4) imply that there is a constant pressure distribution in the direction normal to the wall throughout the boundary layer (but the pressure along the wall, in x-direction, may vary). This means we can the apply Bernoulli's equation for steady flow in order to further simplify the x-momentum (White [2006]):

$$\frac{\partial p}{\partial x} = -\rho U\frac{\partial U}{\partial x} \tag{5}$$

Together with the continuity equation, we have the incompressible boundary layer equations (Cengel [2014]):

$$\frac{\partial u}{\partial x} + \frac{\partial v}{\partial y} = 0$$

$$u\frac{\partial u}{\partial x} + v\frac{\partial u}{\partial y} = U\frac{dU}{dx} + \nu\frac{\partial^2 u}{\partial y^2} \tag{6}$$

Blasius (student of Prandtl) introduced a non-dimensional similarity variable in the BL-equations that eventually yielded a differential equation, known as Blasius equation for flat plate flow. Blasius derived numerical solutions for this differential equation, and thus found exact solutions for the boundary layer thickness White [2006]. The essential part here is to note that both analytical solutions and approximations for thickness of the laminar boundary layer exists, which we can effectively apply in our CFD computations in the evaluation of the required grid resolution within boundary layers.

The equations presented are computed for flat plate flow with a Cartesian coordinate system. For practical engineering purposes, walls of arbitrary shapes and curvatures are just as important and very relevant in the context of CFD analysis of circular cylinders. Cite provide some discussion regarding the validity of the boundary layer equations along a curved wall. The most prominent difference is that the pressure gradient normal to the surface is no longer negligibly small (as it was in Equation 4). However, White [2006] concludes that as long as the BL thickness δ is much smaller than the radius of curvature R, the normal pressure gradient will be small and the boundary layer equations 6 are still valid. The equations will not be true for sharp corners, which invite to immediate separation which violates with one of the basic assumptions of the boundary layer theory.

<u>Turbulent boundary layers:</u>

Turbulent boundary layer equations are also derived based on the same principles of order-of-magnitude analysis. However, since one cannot solve the boundary layer equations for turbulent flow (partly because turbulence by nature is unsteady, so the time-dependent term of the Navier-Stokes equations cannot be neglected), only empirical approximations are available. Among the most common turbulence boundary layer approximations is the log law expressed in terms of the non dimensional variable u*, called friction velocity:

$$\frac{u}{u^*} = \frac{1}{\kappa} ln \left(\frac{yu^*}{\nu} \right) + B \tag{7}$$

where $u^* = \sqrt{\frac{\tau_w}{\rho}}$ and κ and B are constants

The log law applies to a significant portion of the turbulent BL. The log law in fact turns out to be applicable in a great number of geometries of wall-bounded turbulent BL, not only for flat plates (Cengel [2014]). Very close to the wall however there is a region called the viscous sublayer where the law of the wall is unable to capture the behaviour of the BL. In this region, turbulent fluctuations are suppressed due the to close proximity of the wall, and the profile is nearly linear Cengel [2014]. It is common practice to express turbulent boundary layers in terms of "inner variables" or "law of the wall" variables, y^+ amd u^+, defined as

$$y^+ = \frac{yu^*}{\nu} \qquad \text{and} \qquad u^+ = \frac{u}{u^*} \tag{8}$$

Using these variables, the behaviour of the turbulent boundary layer in the different regions is much clearer. The law of the wall-variables are often specified in CFD softwares in order to model grid in turbulent boundary layers, so it is important to have some background understanding of these concepts. Another empirical equation called Spalding's equation captures both the viscous sublayer and the log-layer of the turbulent boundary layer into one equationTennekes and Lumley [1972]. Figure 3 illustrates the different regions of the turbulent BL represented by the above mentioned empirical approximations, in addition to a few other models which are not discussed in this thesis.
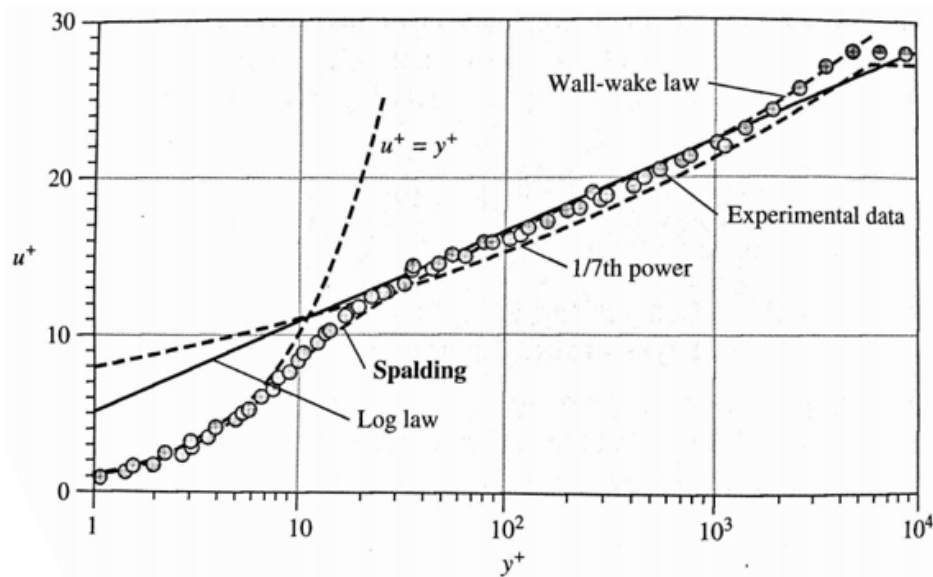
Figure 3: Turbulent boundary layer models (Cengel [2014])

In the simulations performed in this master thesis, the Reynolds numbers are of such a magnitude that the boundary layer on the cylinder surface will stay laminar. It is nevertheless natural to mention turbulent boundary layers in this chapter as a follow-up to the laminar boundary layer theory, which could be useful for the reader to be able to distinguish between the two. Some basic understanding of the evaluation of turbulent boundary layers could also be beneficial in case of need for further work.

2.5 Separation point

Separation is the birthing place of the vortex formations in the wake behind a cylinder in a fluid flow. The location of separation as well as the flow characteristics around the separation point can teach us a lot about the development of the wake behind the cylinder. One of the most important parameters used to describe the occurrence of separation is the pressure gradient in the boundary layer on the surface of a cylinder. The pressure gradient varies along the surface of the cylinder as the fluid is moving past the body. When the fluid moves past the front half of the cylinder, the flow accelerates and therefore the pressure gradient decreases here. A boundary layer develops close to the surface with a favourable pressure gradient. On the backside of the cylinder however, the outer flow decelerates and an adverse pressure gradient develops. The flow is likely to separate from the surface at some point, which results in wake formations behind the body. When the flow region outside the boundary layer (which can be approximated as inviscid and irrotational) is accelerating, U(x) is increasing and P(x) is decreasing (inside the boundary layer). The pressure gradient in this scenario is termed favorable. The boundary layer in such a flow is usually thin and "hugs" to the wall, and separation in this case is not likely Cengel [2014]. When the outer flow decelerates, U(x) decrease and P(x) increase, and we have an adverse pressure gradient with a thicker boundary layer. If the adverse pressure gradient is strong enough ($\frac{dp}{dx}$ is large), the flow will eventually separate. The behaviour of the velocity gradient $\frac{du}{dy}$ during separation is also of importance. Before separation, the gradient is positive, but when separation occurs the

gradient becomes zero, i.e $\frac{du}{dy}=0$. After separation, a backflow can be observed and the velocity gradient is negative. These concepts are illustrated in Figure 4
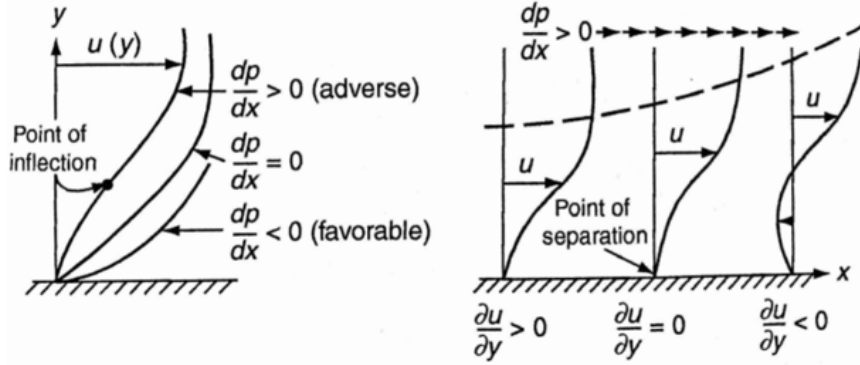

Figure 4: Behaviour of velocity and pressure gradient during separation (White [2006])

Another characterizing quantity of separation is the wall shear stress, τ_w. Generally shear stress in a two dimensional flow given by the following equation.

$$\tau = \mu \left(\frac{\partial u}{\partial y} + \frac{\partial v}{\partial x} \right) \tag{9}$$

By orders of magnitude, $\frac{\partial v}{\partial x}$ can be neglected. The remaining derivative is evaluated at y=0, so we arrive at the equation for the wall shear stress

$$\tau_w \approx \mu \left(\frac{\partial u}{\partial y} \right) \bigg|_{y=0} \tag{10}$$

With our knowledge of the behaviour of the velocity gradient around the separation point, we can conclude that at the wall stress will be zero at point of separation. This will be used in later to detect the separation point in the various simulations to be performed.

Whether the flow in the boundary layer is laminar or turbulent also has a big impact on separation. Generally speaking, laminar boundary layers have poor resistance to adverse pressure gradients and separate more easily than turbulent boundary layers. Turbulent boundary layers resist separation longer at the expense of increased thermal energy transfer and higher wall friction White [2006].

2.6   Vortex shedding and wake behaviour

For most Reynolds numbers, flow separation will occur successively on the top and bottom of the cylinder body, leading to the development of free shear layers leaving the cylinder surface. White [2006] defines a free shear layer as a flow layer in possession of strong velocity gradients created by some upstream mechanism, which is in the context caused by the mechanism of separation. The alternating vortex shedding lead to the evolution of the famous a Von

Karman vortex street. An important parameter of interest when it comes to vortex shedding is the Strouhal number. This non-dimensional number combines the vortex shedding frequency f_V, cylinder diameter D and flow velocity U. The relationship between the Strouhal number and the Reynolds number is important in the study of circular cylinders. The above described concepts are illustrated in Figure 5 and the Strouhal number formulated in Equation 11

Von Karman studied the vortex formations in the wake behind a circular cylinder, and described it mathematically through a stability analyses of idealized vortex streets compared with experimental studies Faltinsen [1990]. The discribed concepts are illustrated in Figure 5.
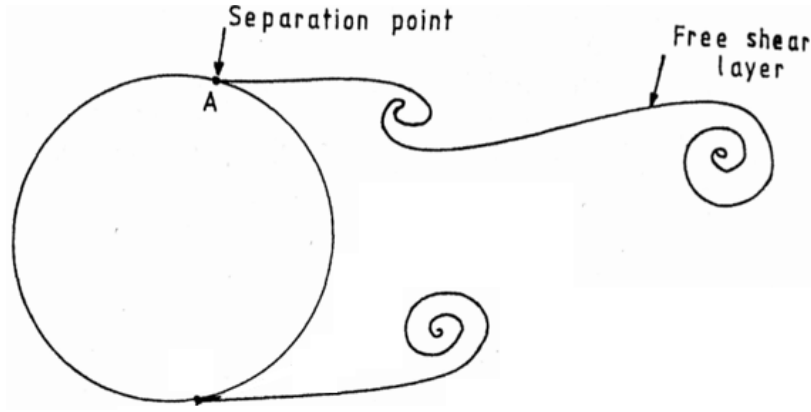
Figure 5: Vortex shedding (Faltinsen [1990])

$$St = \frac{f_v D}{U} \quad \text{where} \quad f_v = \frac{1}{T} \tag{11}$$

In general for three dimensional flow around straight cylinders, vortex shedding may occur either parallel or obliquely. The flow is called two-dimensional if all eddy filaments are parallel to the cylinder axis (Zdravkovich [1997]), while oblique shedding occurs when the free shear layers separate from the cylinder surface at some angle. Oblique shedding is in many cases a naturally occurring feature of the flow depending on the Reynolds number, but may also be triggered by external causes such as the boundary conditions, specifically by the physical set up of the cylinder ends in experiments. Williamson [1988a] provided convincing experimental evidence that in the flow past straight circular cylinders, end conditions can induce oblique vortex shedding a certain length along the span even in the laminar range. By application of angled end-plates in the experiments, parallel shedding was induced along the whole span of the cylinder, illustrating the importance of end-effects in the experimental set up. The study of Williamson [1988a] provides a mathematical formula linking the parallel shedding frequency S_0 to the oblique shedding frequency S_ϕ as:

$$S_0 = \frac{S_\phi}{cos\phi} \tag{12}$$

Determination of whether the phenomena of oblique vortex shedding is an intrinsic flow feature or induced by ex-

perimental or numerical conditions is the subject of many studies, and will be further reviewed in Section 3 and in the discussions of the simulations performed in the present master thesis.

Another important feature of the wake behind the cylinder worth mentioning is the presence of vorticity in the flow field. Faltinsen [1990] states that the vorticity is concentrated in thin sheets leaving the separation point. This is in line with definitions of the free shear layers, which we know exhibit strong velocity gradients. Vorticity is defined in compact notation as in Equation 13 and written out on component form in Equation 14 (Meiburg [2002]).

$$\omega = \nabla \times u \tag{13}$$

$$\omega_x = \frac{\partial u_z}{\partial y} - \frac{\partial u_y}{\partial z}, \quad \omega_y = \frac{\partial u_x}{\partial z} - \frac{\partial u_z}{\partial x}, \quad \omega_z = \frac{\partial u_y}{\partial x} - \frac{\partial u_x}{\partial y} \tag{14}$$

The vortex shedding is unsteady for the major share of Reynolds numbers, creating oscillations in the pressure distribution around the cylinder and thus an oscillating lift and drag force. We need to introduce some descriptive parameters in order to quantify features of the flow, so that we can compare our simulation results research. The parameters of interest when it comes to the forces exerted to the cylinder are the lift and drag coefficients:

$$C_D = \frac{F_x}{\frac{1}{2}\rho U^2 A_{ref}} \tag{15}$$

$$C_L = \frac{F_y}{\frac{1}{2}\rho U^2 A_{ref}} \tag{16}$$

Where F_x and F_y are the mean force in x- and y directions and A_{ref} is the reference area, in the straight cylinder simulations equal to the cylinder diameter multiplied by the spanwise length of the cylinder. In the present work, the mean drag force is used while for the lift the root mean square (RMS) is applied, since the lift is usually oscillating around zero. The RMS is a statistical parameter that is useful to apply when describing parameters having both positive and negative quantities, such as the lift coefficient. Another popular parameter in the study of flow around three dimensional cylinders is the base pressure, described non-dimensional by the base pressure coefficient C_{pB} as

$$C_{pb} = \frac{p_B - p_0}{\frac{1}{2}\rho U^2} \tag{17}$$

Where p_B is the so-called base pressure and p_0 is the ambient pressure. The base pressure p_B is defined as the time-averaged pressure component at the the base of the cylinder surface, which is 180° from the front. In the case of a three dimensional cylinder, p_B is taken at L/2 of the spanwise length of the cylinder. The base pressure serves as a useful parameter in the comparison of results as it turns out that from previous conducted experiments that the pressure is constant over a major lee part of a cylinder in a uniform flow (Faltinsen [1990]). In addition, it is non-dimensionalized without taking any length scale of the cylinder into account, making comparisons of different

geometries easier, such as straight cylinder vs curved cylinder.

2.7   Classification of flow regimes based on Reynolds number

Several definitions of the different flow states based Reynolds numbers for flow around straight cylinders exist in literature. In the present master thesis we will stick to definitions by Zdravkovich [1997] where the flow states are divided into the main regimes listed in Table 1.

State	Re Range
Laminar, L	$0 < \mathrm{Re} < 200$
Transition in wake, TrW	$180 < \mathrm{Re} < 400$
Transition in shear layers, TrSL	$350 < \mathrm{Re} < 2 \cdot 10^4$
Transition in boundary layers, TrBL	$1 \cdot 10^4 < \mathrm{Re} < (?)$
Fully turbulent, T	$(?) < \mathrm{Re} < \infty$

Table 1: Flow regimes defined by Reynolds numbers, according to Zdravkovich [1997]

In the laminar range, the flow has not yet transformed into turbulent in any parts of the regions surrounding the cylinder. The laminar range consists of three sub-ranges. For low Reynolds numbers, $\mathrm{Re} \leq 5$, the flow can be regarded as creeping, being dominated by viscous forces. The fluid lingers around the face cylinder in a symmetric fashion without the occurrence of separation. Increasing the Reynolds number slightly above this threshold will induce separation of the boundary layer and a free shear layer will separate from the surface of the cylinder. The region 4 - 5 < Re < 30 - 48 is characterized by steady separation, forming a pair of oval, recirculating flow bubbles behind the cylinder which Zdravkovich [1997] refers to as a closed near-wake region.

When increasing the Reynolds number further, an adverse pressure gradient in the end of the closed near-wake region induces a wave-like behaviour of the flow downstream of the cylinder. These waves represent the early phase of what Zdravkovich [1997] call the periodic laminar regime, 30 - 48 < Re < 180 - 200. In this region the flow starts to separate successively from the top and bottom of the cylinder (Rahman et al. [2008]), and the flow is now characterized as unsteady. The cylinder will experience a varying pressure distribution because of this alternating shedding, which in turn gives an oscillating lift and drag force. The flow is still laminar in all regions of disturbed flow in this phase and can be regarded as two-dimensional.

After the laminar state the flow starts to transition to turbulence in the far wake behind the cylinder. Zdravkovich [1997] talks of two main transition regimes: The lower transition regime TrW1 for 180 - 200 < Re < 220 - 250 and the upper transition regime TrW2 for 220 - 250 < Re < 350 - 400. Characteristic to both of these transition regimes is the presence of streamwise vortex formations. Eddies perpendicular to the two dimensional vortex filaments start to show up and the flow must now be regarded as three dimensional. In the near wake the flow is still laminar, however in the far wake the flow eventually transitions into turbulence. The most famous research within the TrW-range of Reynolds numbers was performed by Williamson [1988a], which famously labels the above mentioned sub-regions as Mode A and Mode B, and further describes the characteristics of the phases in the utmost detail. The TrW state is

also the region in which the CFD simulations of the present master thesis are conducted. A thorough review of the existing literature on this flow regime is presented in Section 3.

A second transition in the wake starts to occur as the Reynolds number is increased above 350 - 400, entering the region of transition in shear layers, TrSL. This state develops during a rather wide range of Reynolds numbers, as can be seen in Table 1. As indicated by the name of the state, a transition in the free shear layers develop before rolling up into turbulent eddies (Zdravkovich [1997]). The TrSL state can also be divided into subcategories, but this is not described in further detail in the present text. At some point beyond $1 \cdot 10^4 < \text{Re} < 2 \cdot 10^4$, the wake being fully turbulent at this stage, a transition of the boundary layer on the cylinder surface starts to occur. After further increase in Reynolds number, all regions of disturbed flow are turbulent. The alternating shedding can be detected all the way to $\text{Re} = 10^7$ (White [2006]). The three latter states of Reynolds numbers, TrSL, TrBL and T, are not subject to discussion in this master thesis, and are thus merely mentioned in this report.

3   Literature review

Flow around circular cylinders has been researched extensively throughout history due to the many practical engineering applications of the topic. Among the fundamental research performed within this field are the experimental studies undertaken by the Czech physician Strouhal who investigated the vibrations of strings of wire in air, showing that the vibration frequency was depended on the relative air velocity rather than the elastic properties of the wire (Roshko [1953]). Von Karman studied the vortex formations in the wake behind a circular cylinder, and described it mathematically through a stability analyses of idealized vortex streets compared with experimental studies (Faltinsen [1990]). The flow around a three-dimensional straight cylinder has been extensively studied, both by means of experiments and observations, and more recently through utilization of numerical tools. A general classification of flow regimes for straight cylinders based on Reynolds numbers as defined by Zdravkovich [1997] has already been presented in Section 2.7. The present master thesis undertakes low Reynolds number simulations, and so this literature review is focused on studies on the laminar (L) and the transition in wake (TrW) states of flow. Several of the concepts introduced in Section 2 are in the current review frequently applied, and the reader is assumed familiar with the terms and expressions at this point.

3.1   Straight cylinders

Roshko [1953] was among the earliest to conduct a systematic, experimental study of low Reynolds number flow past straight circular cylinders. The study involved straight cylinders of various geometries, in addition to flow past rings. Two distinct sub ranges were defined for this low velocity flow based on Reynolds number, the first being range $40 < \text{Re} < 150$ of stable, laminar and two dimensional flow wake, followed by a transition region between $150 < \text{Re} < 300$. In this transition region, three dimensional vortex formations were observed. The regime for Re > 300 exhibited irregular wake formation and turbulent features. Tritton [1959] performed further experiments on circular cylinder in the laminar range up to Re = 100, where a significant part of the study included investigations of shedding frequency compared to flow velocity, i.e Strouhal number as a function of Reynolds number. Observations of different shedding modes based on frequency were documented, which Tritton [1959] called low- and high speed modes. Vortex shedding could namely occur at different frequencies where a discontinuity or drop in frequency caused a transition between the modes, although this drop did not occur at the same Reynolds number in all of the experiments conducted by Tritton [1959]. The discussion turned into a long lasting controversy in research over the St-Re relationship in the laminar range. Gerich and Eckelmann [1982] showed the existence of cells along the spanwise length of the cylinder where different shedding modes would occur simultaneously. Their research found that whether the cylinder ends were free or fitted with end-plates would alter the vortex shedding mode locally. The debate on the present discontinuities in the St-Re relationship was finally put to rest when Williamson [1988a] studied the problem and illustrated that the two modes first described by Tritton [1959] were in fact governed by the phenomena oblique shedding, which was to a large extent was caused by cylinder end conditions. His experiments showed that parallel shedding along the whole span of the cylinder could be induced by slanting the end plates with a certain angle, which yielded a uniform St-Re relationship with no sudden discontinuity within the periodic-laminar range. Williamson [1988a] also found that any oblique shedding could be transformed into the universal mode by

3. Literature review

Mortensen, Olav Egaas

a trigonometric relation (described in Section 2.6), which further demonstrated that parallel shedding is in fact the true, intrinsic shedding mode in the periodic-laminar range up to Re < 180. The famous St-Re relationship from the study of Williamson [1988a] with the described features can be seen in Figure 6.

A considerable amount of research attention has been directed at finding the origins and the development of the transitions in the wake for Re < 180. Hama [1963] made some further progress on the field and showed that instabilities in the wake takes first takes form as a three dimensional waviness along the primary Von Karman vortex filaments, describing the phenomena by mathematical models as both a "Gaussian distortion" and a "sinusoidal distortion" along the span of the cylinder. The formation of secondary vortices in the streamwise direction were documented by Gerrard [1978], famously calling them "fingers of dye" as they mimic fingers pointing towards the face of the cylinder. According to Gerrard's observations, the fingers were visible in the region 140 < Re < 500, appeared at random positions along the span and endured for about

Figure 6: Strouhal numbers (S) versus Reynolds numbers Re, based on experiments with three different cylinders performed by Williamson [1988a]

2-3 cycles downstream in the wake. Williamson [1988b] was also on this topic first to describe the presence of two different modes within the TrW range of Reynolds number with distinct differences in the development of secondary, streamwise vortices. Williamson [1988b] found two discontinuities in the St-Re relationship above Re > 180, associated two distinct types of wake formations labelled mode A and B. These discontinuities are also marked in Figure 6. A full review of the different features and origins of shedding modes A and B were described by Williamson [1996]. According to this study, the most prominent difference between the two modes is the spanwise lenghtscales between each streamwise vortex. In Mode A, the spanwise wavelength (distance between each finger) is around 3-4 diameters, while that of Mode B is significantly smaller and measured to 1 diameter. The origins of the two modes are distinct from one another, where Mode A is described to appear due to an instability in the primary vortex core which causes this spanwise waviness described earlier, which results in streamwise vortices being "stretched" between the primary vortices. Mode B on the other hand scales on the smaller physical structures of the flow, namely the braid shear layer, and therefore appears with shorter wavelengths than that of mode A. Photographs from the experiments conducted by Williamson [1996] can be seen in Figure 7, clearly illustrating the differences between the modes.
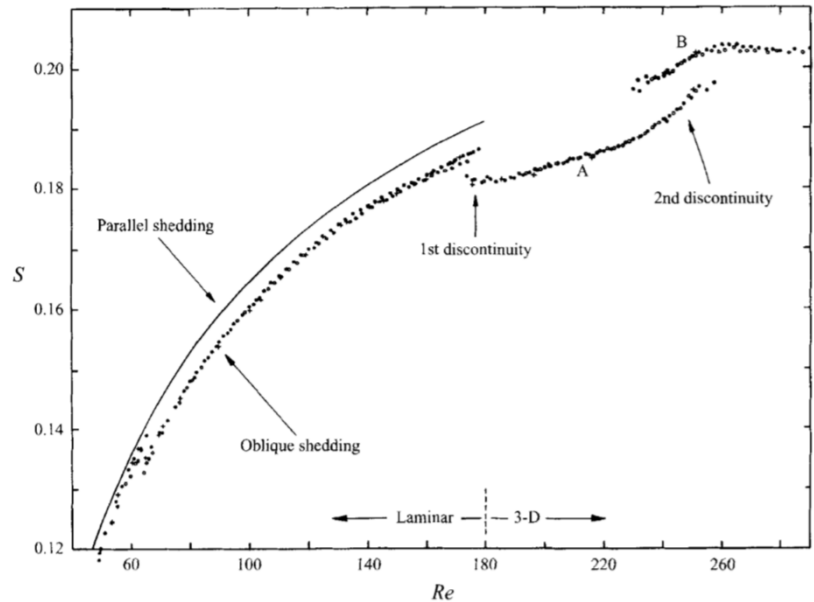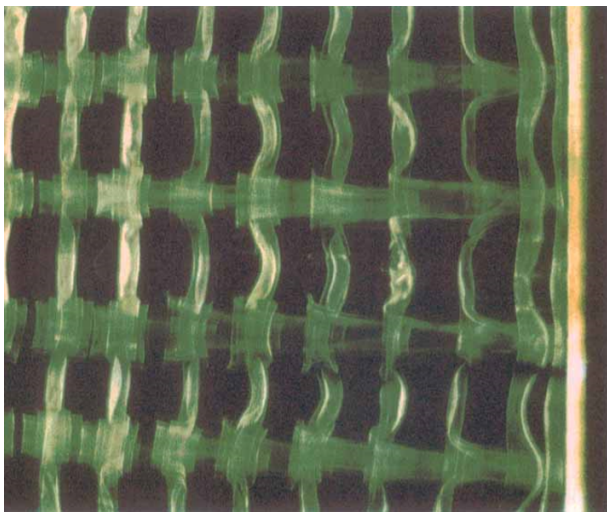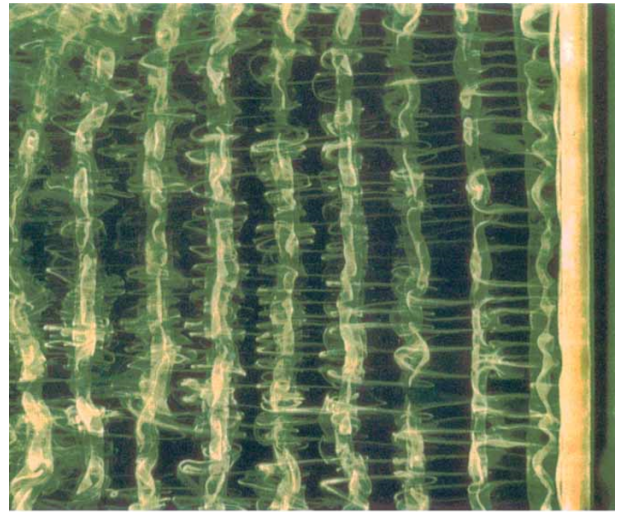
15

(a) Mode A, flow at Re=200, spanwise wavelength of 4D

(b) Mode B, flow at Re=270, spanwise wavelength of 1D

Figure 7: Mode A and B visualized, from Williamson [1996]

Another important feature of the transition regime, mainly discussed in Williamson [1996] and in an earlier paper Williamson [1992], is the occuring phenomena of "vortex dislocations". These are large scale vortical structures appearing in the primary vortex shedding near the body as a result of phase dislocations i.e varying frequency components along the span of the cylinder. The dislocations are easily spotted in the visualizations provided by Williamson [1992]:
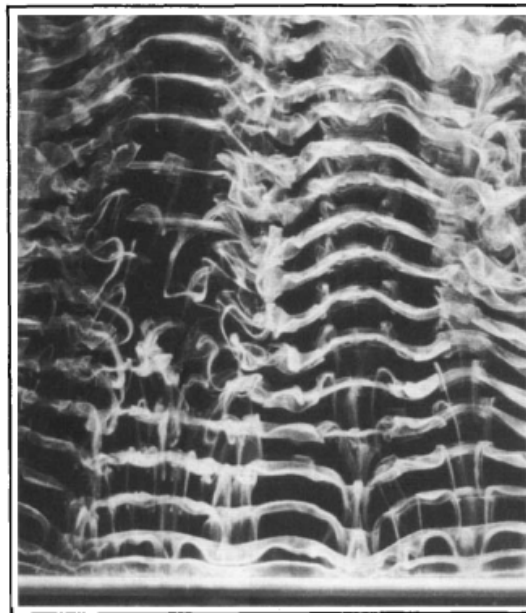
Figure 8: Appearance of vortex dislocations, from Williamson [1992]

After Williamson's thorough and accurate description of the origins and properties of the shedding modes in the TrW region, fewer experiments have been conducted for this range of Reynolds numbers. On the computational side on the other hand, there has been a growth in numbers of numerical simulations as a result of increasing computer capacity and more reliable numerical methods. Thompson et al. [1996] and Karniadakis and Triantafyllou [1992] performed some early numerical investigations in the TrW. In the simulations of Thompson et al. [1996] tests were conducted with a spanwise length of cylinder of $4\pi R$ which resolved mode A type of shedding with properties similar to that of Williamson [1996] experimental studies. Karniadakis and Triantafyllou [1992] used only half of this spanwise length, which turned out to not initiate mode A shedding, illustrating the importance of a spanwise length in the simulations of a 3D straight cylinder. Barkley and Henderson [1996] also conducted numerical simulations of the flow past a circular cylinder for Reynolds numbers in the range $140 < Re < 300$. Time-dependent simulations of the Navier-Stokes equations on a two dimensional domain were obtained and a Floquet stability analysis reveal that the configuration becomes completely unstable to three-dimensional perturbations at a Reynolds number 188.5 ± 1. The numerical analysis managed to reproduce the St-Re relationship derived experimentally by Williamson [1988b] with remarkable precision, as well as reporting wavelengths of 3.96 ± 0.02 diameter for mode A wake formations and wavelength 0.82 diameter for the second instability initiation (mode B). This is in good agreement with earlier experimental results, illustrating the increasing reliability of numerical results within the field.

3.2 Curved cylinders

The first studies of flow past curved cylinders came from experimental investigations of flow past rings of cylindrical cross sections. As pointed out by Leweke and Provansal [1995], one of the advantages of conducting experiments with this set-up is how the cylinder ends are effectively avoided, enabling the study of the intrinsic flow features without the concern of end effects. Roshko [1953] briefly studied the flow past rings with some variations in curvature. His early findings indicated that the vortex shedding behind rings with a large aspect ratio (radius of curvature divided by diameter) behaved very similar to that of a straight cylinder. Rings of small aspect ratios showed clear similarities to the vortex loops created by the flow past a disk. Bearman and Takamoto [1988] studied wakes behind rings compared to namely disks. The study revealed that there is a striking change in shedding development when the outer diameter of the ring is more than 50% larger than the inner diameter. Above this threshold (that means large aspect ratios of curvature), the vortex shedding exhibit periodic and approximately axisymmetric vortex rings in the wake. Leweke and Provansal [1995] were the first to perform a systematic experiment solely dedicated to investigate the flow around a ring with a circular cross section, with some variations in geometry and ring curvature. One of the main questions the study addresses is which three dimensional flow phenomena that are intrinsic to the vortex shedding regime behind such a three dimensional body. The term intrinsic refers to flow behaviour that are caused solely by three dimensional effects rather than end-effects, i.e results that are not polluted by end boundary condition effects. The experimental study show that depending on the initial conditions, the wake behind the ring takes the form of parallel vortex rings or helical vortices looking like streamwise loops, indicating oblique vortex shedding also in the periodic laminar range ($Re < 180$). The fact that oblique vortex shedding occur in this range of Reynolds numbers is to some extent in contradiction to what Williamson [1988b] illustrated for flow in the same Reynolds number range for straight cylinders, namely that the parallel shedding being the true shedding mode in this range. The study of Leweke and Provansal [1995] shows that the oblique vortex shedding in the laminar range

is in fact an intrinsic feature of the flow and can be induced by variation in initial conditions. Arguments were also presented pointing towards that the oblique shedding angle varies somewhat with the curvature. See figure 9 as an illustration of the difference between these modes.
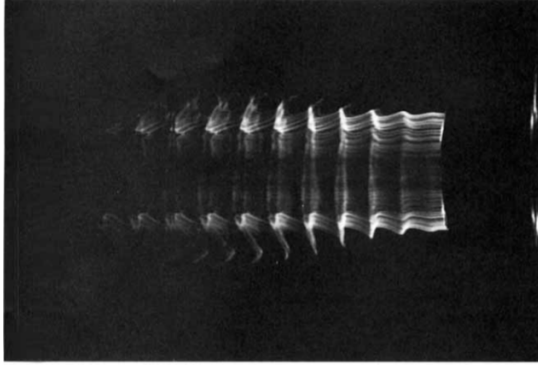
(a) Parallel vortex shedding causing symmetric vortex rings
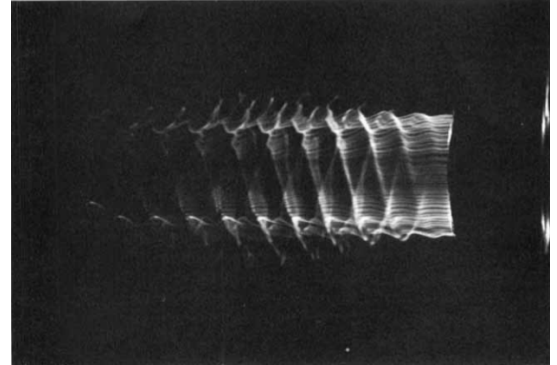
(b) Oblique vortex shedding causing helical wake

Figure 9: Different modes of vortex shedding caused by variations in initial conditions for flow past ring at Re=105 (Leweke and Provansal [1995])

When it comes to the direct effects of curvature on the flow development, the study of Leweke and Provansal [1995] highlights that essentially the flow behaviour of a curved cylinder is very similar to a straight cylinders when the aspect ratio is high, i.e when the curvature is small, although some differences were observed. The study puts forth an expression for the St-Re relationship in the periodic range which includes the parameters of curvature and oblique shedding angle, based on experimental results of rings with different curvatures. The effect of curvature may decrease the shedding frequency up to 5% for for Reynolds numbers in the upper region of the laminar-periodic range, whereas the frequency differences are almost negligible for low Reynolds numbers. The study also shows that the difference in shedding frequency is also present in the transition region TrW. Also in this region of Reynolds numbers, the frequency is generally lower than for a straight cylinder. One observation is that the effect of the curvature is generally smaller in mode A. Figure 10 is taken from Leweke and Provansal [1995] which illustrates some of the described differences in frequencies present at different Reynolds numbers.
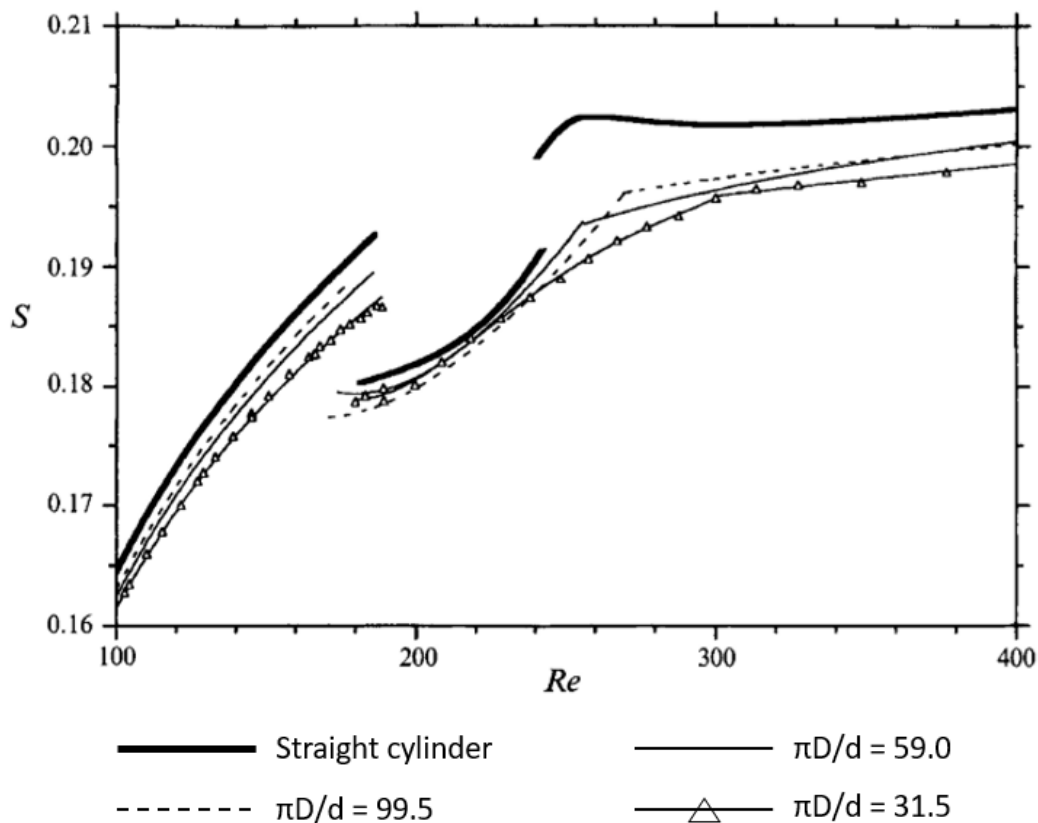
Figure 10: Strouhal numbers (S) versus Reynolds numbers (Re) for flow beyond rings of various aspects ratios, compared to that of a straight cylinder. Experimental results from the study by Leweke and Provansal [1995].

More recently there has been an increasing focus on flow in parallel to the plane of curvature, on both the experimental and especially the computational side. In these studies flow configuration may be termed either convex or concave depending on the orientation of the curvature with respect to the inflow. A convex flow in this context refers to flow towards a curved cylinder with stagnation along the outer radius. Concave flow is used on flow in the opposite direction with stagnation on the inside of the ring. Illustrations of these two configurations taken from the study of Miliou et al. [2007] can be seen in Figure 11. The present master thesis is mainly focused on cross-flow configurations, but some review of existing research on flow around curved cylinders in other directions are nevertheless included. The studies may reveal interesting details on computational set-ups and numerical considerations that could prove useful in the current thesis, in addition to casting some light over which other interesting flow phenomena may arise for other directional flows.

(a) Convex flow configuration

(b) Concave flow configuration
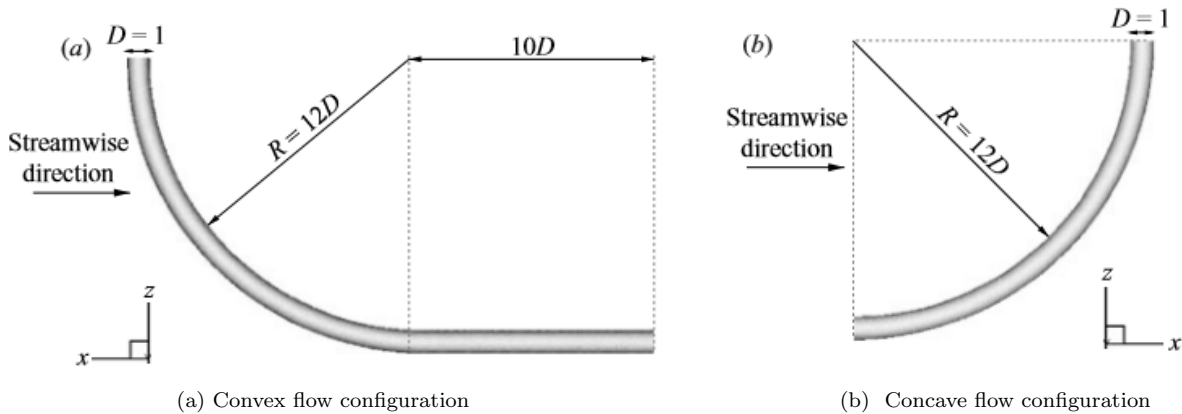
Figure 11: Flow configurations parallel to plane of curvature from study of Miliou et al. [2007]

Miliou et al. [2007] performed both numerical simulations and towing tank experiments on in-line flow towards quarter sections of rings in both concave and convex orientations. The convex flow case revealed a fully three-dimensional wake developing behind the cylinder, including vortex shedding in the upper part of the cross section which seemingly influences the shedding frequency in the lower region, creating one dominant shedding frequency. However for the concave case, vortex shedding did not occur. The paper suggests that the axial flow along the curvature plays a role in suppressing the shedding which is expected for cylinders without curvature (i.e straight cylinders). Jiang et al. [2018] published a numerical study of the in-line flow across a concave cylinder with a similar domain as that of Miliou et al. [2007] to effectively be able to compare the results between the studies. An significant alteration to the domain was however included; a horizontal and vertical straight extension to the curved cylinder seen in Figure 11b. In the domain of the concave flow in the study of Miliou et al. [2007] as seen in Figure 11b, the boundary condition at the free end of the cylinder interacts with the inlet surface of the domain, which could in theory affect the intrinsic flow features of the concave configuration. In the study of Jiang et al. [2018], a direct numerical simulation (DNS) conducted for Re = 100 illustrates that the inclusion of a horizontal extension to the lower end of the curved cylinder assists in suppressing the unwanted effects of boundary conditions. An extension to the curved cylinder allows for a developing boundary layers along the straight extension, before the flow reaches the curved cylinder and generates a more realist wake behind it. A horizontal extension of 10D is recommended for the present case. Several other research papers have highlighted the importance of domain choice and boundary conditions in the numerical simulations. Gallardo et al. [2013] discussed the effects of boundary conditions in simulations of convex flows. The study illustrates that the free-slip boundary condition applied on the domain edges in direct contact with the curved part of the cylinder effectively suppress intrinsic flow features of the curved cylinder, illustrating the need of straight extensions also in this flow configuration. Jung et al. [2019] recently investigated flow past curved cylinder configurations with similar geometrical properties to the studies of Miliou et al. [2007] and Jiang et al. [2018], performing simulations at angles of incident both parallel and perpendicular to the plane of curvature, explaining how the flow features differs between these configurations at Re = 100. Figure 12 illustrate qualitatively the differences between the flows.
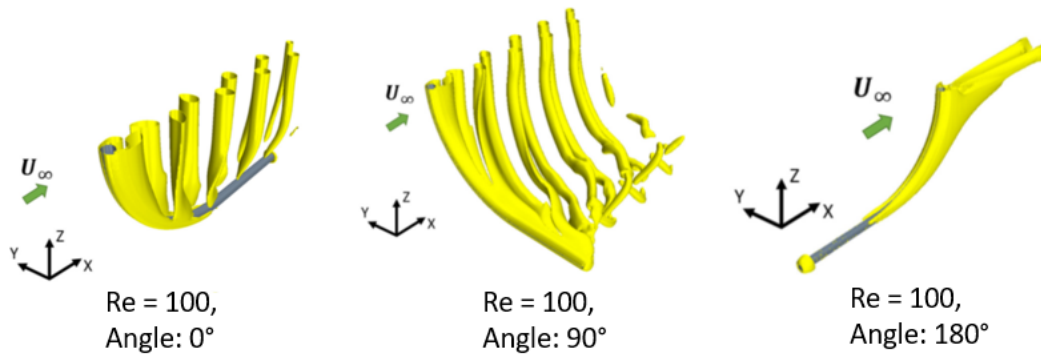
Figure 12: Flow visualization of curved cylinder flows at different angles of incidents at Re = 100, from simulations by Jung et al. [2019]

Some of the most recent research on the field of flow past curved cylinders comes in the form of DNS investigations of turbulent flow regimes behind concave and convex flow configurations have been. Gallardo et al. [2014] and Jiang et al. [2019] have both conducted a studies of a quarter ring in convex and concave configurations respectively, both at Re = 3900. Among the main findings of co-existing flow regimes, where the flow field is dominated by a periodic asymmetrical helical vortices. The study claims that this dominating flow field originates from an oblique shedding regime in the neighbouring cells of the curved surface. This high Reynolds number flow regime is classified within a higher Reynolds number regime (TrSL) than directly relevant for the flow simulations in the present analysis, but nevertheless illustrates some interesting flow phenomena worth taking note of. As the time of writing the study is not yet published, as it is awaiting review.

4   Governing Equations and Numerical Framework

The idea behind CFD is is to produce numerical solutions to a system of partial differential equations (PDE) that describes fluid flow. These differential equations are in essence the Navier-Stokes equations. These equations are discretized within a computational domain and solved for a given set of boundary- and initial conditions. For the applications relevant in this report, the output of the calculations performed is the flow velocity components u,v,w and the pressure p at each gridpoint in the domain. These outputs are afterwards used a to visualize the results in order to describe the characteristic features of the flow field.

There are different approaches on how to solve the governing equations in CFD, depending on the flow properties, geometrical parameters, etc. Direct Numerical Simulation (DNS) is a method where the Navier-Stokes equations are solved directly. That means no modelling or reformulations of any terms in NS is required. The usefulness of DNS is however often restricted to research, as the need for computational capacity increases rapidly with increasing Reynolds number. For highly turbulent flows, it is often too demanding to use DNS. Reynolds Averaged Navier-Stokes equations (RANS) is the most common method within turbulent CFD simulations. An averaging technique is applied to the classical Navier-Stokes equations in order to obtain an averaged version of the partial differential equations. In addition, a certain turbulence model must be applied where the different scales of turbulence is "smeared out". This mean that the effects of all the eddies of various sizes are approximated, instead of resolving all scales the way down to the Kolmogorov scales. Another up-and-coming CFD approach is called Large Eddy Simulation (LES). In this method, the idea is to resolve the largest eddy scales, while the smaller scales are still modelled by means of some turbulence model. The quality of an LES simulation is highly dependent on how large the fraction of the turbulent energy spectrum which is resolved. Several research papers within CFD apply LES in their simulations, and so it is of interest to have some knowledge on the topic.

4.1   Governing equations

Navier-Stokes Equations

The Navier-Stokes equations (NS) and the continuity equation are the fundamental governing equations for viscous fluid flow. The continuity equation represent conservation of mass within a fluid element, while the Navier-Stokes equations represent conservation of momentum. In marine applications, sea water is usually as the fluid of interest, which can be approximated as both incompressible and isothermal. These assumptions implies that the properties of density ρ, dynamic viscosity μ and kinematic viscosity ν remain constant in the whole domain. It is also worth mentioning that when the flow is assumed to be isothermal, implying that the local variations in temperature in the fluid can neglected, there is no need for a differential equation for conservation of energy. These assumptions reduce the complexity of a general flow problem and will be applicable for all the simulations performed in the present master thesis.

The continuity equation under these assumptions is given as

$$\frac{\partial u}{\partial x} + \frac{\partial v}{\partial y} + \frac{\partial w}{\partial z} = 0 \tag{18}$$

while the Navier-Stokes equations in three dimensions are given as

$$\text{x-direction:} \quad \frac{\partial u}{\partial t} + u\frac{\partial u}{\partial x} + v\frac{\partial u}{\partial y} + w\frac{\partial u}{\partial z} = -\frac{1}{\rho}\frac{\partial p}{\partial x} + g_x + \nu\left(\frac{\partial^2 u}{\partial x^2} + \frac{\partial^2 u}{\partial y^2} + \frac{\partial^2 u}{\partial z^2}\right) \tag{19}$$

$$\text{y-direction:} \quad \frac{\partial v}{\partial t} + u\frac{\partial v}{\partial x} + v\frac{\partial v}{\partial y} + w\frac{\partial v}{\partial z} = -\frac{1}{\rho}\frac{\partial p}{\partial y} + g_y + \nu\left(\frac{\partial^2 v}{\partial x^2} + \frac{\partial^2 v}{\partial y^2} + \frac{\partial^2 v}{\partial z^2}\right) \tag{20}$$

$$\text{z-direction:} \quad \frac{\partial w}{\partial t} + u\frac{\partial w}{\partial x} + v\frac{\partial w}{\partial y} + w\frac{\partial w}{\partial z} = -\frac{1}{\rho}\frac{\partial p}{\partial z} + g_z + \nu\left(\frac{\partial^2 w}{\partial x^2} + \frac{\partial^2 w}{\partial y^2} + \frac{\partial^2 w}{\partial z^2}\right) \tag{21}$$

The Navier-Stokes equations are derived based on Newton's second law of motion, which in other words tells the relationship between mass, acceleration and force. The leftmost term on the left hand side is named the unsteady term, while the following three terms on the left hand side are called acceleration terms. The terms on the right side represent pressure force, body force (e.g gravity) and viscous force respectively. The body force term is in most contexts neglected from calculations. The NS-equations are non-linear partial differential equations that are not at all trivial to finding solutions. For high velocities i.e turbulent flows, the flow exhibits too many random, fluctuating features for us to be able to solve it purely by numerical means - we must introduce certain modelling techniques in order to simplify the mathematical problem.

Reynolds Averaged Navier-Stokes (RANS) equations:
The RANS-equations can be derived by introducing the Reynolds Decomposition into the Navier-Stokes equation. The derivation is shown briefly in the following.Tennekes and Lumley [1972] applies Einstein's notation which is more efficient to simply derive the expression. Using this notation, the Navier-Stokes equation can be written on compact form as

$$\frac{\partial \widetilde{u}_i}{\partial t} + \widetilde{u}_j\frac{\partial \widetilde{u}_i}{\partial x_j} = -\frac{1}{\rho}\frac{\partial \widetilde{p}}{\partial x_i} + \nu\frac{\partial^2 \widetilde{u}_i}{\partial x_j \partial x_j} \tag{22}$$

The Navier-Stokes equation describes the instantaneous momentum of a fluid element. The Reynolds decomposition states that the instantaneous value of a parameter can be written as a sum of it's mean value and it's fluctuations. Here, exemplified with velocity, the instantaneous $\widetilde{u}_i$ can be decomposed by means into an average velocity U_i and a fluctuating velocity u_i:

$$\widetilde{u}_i = U_i + u_i \tag{23}$$

The RANS-equation is derived by inserting the Reynolds decomposition into the regular NS-equation, and further simplifying it by taking the average of all the terms in the equation. Several terms can be canceled out by utilization of the following: First, we have the definitions $\bar{U}_i = U_i$ and $\bar{u}_i = 0$. Secondly, if the Reynolds decomposition is inserted into the continuity equation, it can be shown that both the mean velocity U_i and the fluctuations u_i both conserve mass, i.e $\frac{\partial U_i}{\partial x_i} = 0$ and $\frac{\partial u_i}{\partial x_i} = 0$. This will eventually yield the RANS-equation:

$$\frac{\partial U_i}{\partial t} + U_j \frac{\partial U_i}{\partial x_j} = \frac{1}{\rho} \frac{\partial}{\partial x_j} \left(-P\delta_{ij} + \mu \left(\frac{\partial U_i}{\partial x_j} + \frac{\partial U_j}{\partial x_i} \right) - \overline{\rho u_i u_j} \right). \tag{24}$$

Some reorganizing of the equation has here been done. The three terms on the right hand side of the equation are called pressure stress, viscous stress and turbulent stress respectively. The term $\overline{\rho u_i u_j}$ is of high significance since it is the term that generates turbulence. It originates from the non-linear term on the left hand side of the NS-equation, but it is moved to the right hand side in the RANS-equation. We call the term Reynolds stress or turbulent stress. Due to its highly non-linear nature, it has no analytic solution. In order to solve the RANS-equation we need to find approximate solutions to this term, which is the basic problem in turbulence modelling.

Some of the most common turbulence models are based on so called two-equation models. The most famous of these is called the k-ϵ model. In this model, we have two partial differential equations (PDE) for the turbulent kinetic energy k and the viscous dissipation rate ϵ, in addition to a third unknown quantity that is called the eddy viscosity ν_T. The eddy viscosity is used to describe the Reynolds stress term $\overline{\rho u_i u_j}$ by means Boussinesq's generalized eddy viscousity hypothesisTennekes and Lumley [1972]. There are other common turbulence models as well, for example the k-ω-model and the Spalart-Allmaras model. The details and mathematics of the models are too complex to be presented in a short manner in this report. In most CFD softwares, the user is presented with a choice of which turbulence model to be applied if he is doing a RANS-simulation. Knowledge of the existence and areas of applications of these models is crucial to be able to compute turbulent CFD simulations.

4.2 Spatial discretization and time marching methods

The first step in performing CFD simulations is to create a domain on which a computational grid (or mesh) is generated. In the grid generation, the domain is divided into many smaller cells or elements. It is common to distinguish between structured and unstructured grids. A structured grid consists of plane cells of four edges in 2D mesh generation or 6 faces in 3D cases. The element may have an arbitrary shape, meaning it does not need to be completely rectangular. What is special about structured grids however is the ability to easily enumerate cells in the domain. Each cell is numbered according to indices, often described as (i,j,k) which uniquely correspond to each element in the domain (Cengel [2014]). In unstructured grids, the cells may take the form of various shapes, such as tetrahedrons and hexadrons, or basically any polyhedral shape. Unstructured grids cannot in general be numbered by indices in the same manner as structured grids. CFD softwares usually have some internal way of managing unstructured grids. In comparison, structured grids often converges more quickly to an accurate solution, while unstructured grids are usually easier to generate around complex geometries. Many CFD-codes offer both types of grid generation depending on domain and flow parameters, and even hybrid combinations of the two(Cengel [2014]).

When the domain is descritized into the desired mesh configuration, the governing equations are numerically solved in each of these cells. There are different ways to descritize the equations as well, where finite-difference methods (FDM), finite element method (FEM) and finite volume method (FVM) are among the most commonly used. The methods of FDM and FEM are are only mentioned here to provide some familiarity with the different spatial discretization methods used in CFD codes. The latter method, namely finite volume method, is applied in most modern CFD softwares. The advantage of FVM is intrinsic ability of conserving flow properties. In addition, FVM does not require any transformation of coordinate system in order to be applied on an irregular grid, and can thus be used directly to unstructured mesh. The method is based on a control-volume (CV) way of thinking, where each cell in the computational grid represents a small CV where the following integral law of conservation laws applies (Lomax et al. [2001]):

$$\frac{d}{dt} \int_{V(t)} Q dV + \oint_{S(t)} \mathbf{n} \cdot \mathbf{F} dS = \int_{V(t)} P dV \tag{25}$$

The different terms are not described in detail in the current report, and the above equation is only mentioned to illustrate how the governing equations are discretezed on the computational domain. After the spatial deviates are discretized, a coupled set of non-linear PDE equations need to be solved. A time descretization method needs to be applied, such as the Runge-Kutta scheme, before time integration is performed. The size of the time step is important in these considerations. Choosing a small enough time step is necessary to ensure convergence. One way to check this is to apply Courant-Friedrichs-Lewy (CFL) condition. This is described further in Section 5.

4.3 Boundary conditions

To solve numerical problems, one must always specify boundary conditions (BC). Boundary conditions are constraints in the form of parameters values specified on the edges of the domain. This means that we only have information about the inside of the domain, while the outside is unknown to us. Boundary conditions can be divided mathematically into two main categories: Dirichlet and Neumann. For a Dirichlet boundary, the value of a scalar is fixed on the boundary, while for a Neumann boundary condition the value of a gradient of a scalar is fixed on the boundary. A mixture of Dirichlet/Neumann boundary conditions are also commonly used (Lomax et al. [2001]). The choice of boundary conditions is dependent on the properties that the surface or domain face is meant to represent. A general overview of the most common conventions are mentioned below, as presented by Cengel [2014].[1]

- Wall boundary conditions: This is in essence modelling of the no-slip condition, which is applied on solid surfaces within the domain. All velocity components are usually set to zero (Dirichlet condition) on the wall surface. In some cases a free-slip boundary conditions may also be applied, where the normal velocity component to the wall is still zero, but the fluid is free to move in directions tangential to the wall.

---

[1]CFD softwares may employ different names of boundary conditions than what is defined in this section.

- Inlet/Outlet boundary conditions: These are boundary conditions specified on the boundaries of the domain where the fluid enters and exits. Fixed velocity components at the inlet (Dirichlet) are extensively used in many applications, but it also possible with pressure-specified inlets. The outflow can often specified by a zero pressure or velocity gradient (Neumann condition).

- Miscellaneous boundary conditions: These are boundary conditions applied on faces of the domain which represent neither inlets, outlets or physical walls. Two approaches commonly used are symmetric and periodic boundary conditions. Symmetric boundary conditions mirrors the flow field across the plane on which the boundary condition is specified. Mathematically this usually involves that gradients of the flow field variables normal to the symmetry plane are set to zero (Cengel [2014]). A periodic boundary condition on the other hand can be used when the pattern of the flow field is expected to repeat itself across the the boundary. This involves that flow variables on the boundary are linked to an equal set of variables on an neighbouring face. Both symmetric and periodic boundary conditions are particularly useful for flow fields that repeats itself in some fashion, and can help to reduce required computational resources by a significant amount.

4.4 FINE/Marine

FINE/Marine is developed by NUMECA, one of the major companies within the field of CFD. FINE/Marine is designed for marine applications specifically, with features such as free-surface models, multi-fluid simulations of flow around ship hulls with various kinds of appendages. When using FINE/Marine, you work in three different softwares that are all integrated within the FINE/Marine-package. The first software out of these three is called HEXPRESS, being the domain- and grid generation application. After a model has been created and meshed in HEXPRESS, a simulation is set up with the desired flow parameters, boundary conditions, etc, and simulations are performed in the flow solver ISIS-CFD. The third software is named CFView, where post-prosessing and visualization of the flow computations can be performed. This section gives only a brief description of the software components. For a deeper and more comprehensive description of the software, the Online Documentation Platform can be used as reference (NUMECA).

5 Computational grid, domain and time step

A preliminary case study of the flow past a two-dimensional circular cylinder at Re=100 has been performed with focus on learning how to use FINE/Marine and the various software features. The creation of the 2D model in HEXPRESS and the set up of the simulation in FINE/Marine is in this section presented. This is included in order for the reader easily be able to repeat the work done in the thesis. Moreover, the work in this case study also involved settling the two-dimensional domain size, grid resolution in the various parts of the domain and as deciding a required size of time step. The end goal of the present master thesis is obviously to perform more complex, three dimensional simulations, however the findings of the initial, two-dimensional simulations proved very useful with regard to settling several computational parameters. In the current chapter, the modelling approach is described along with the convergence studies related to settling mesh configuration, domain size and time step. The general geometry for the flow configuration can be seen in Figure 13, where the parameter a is to be decided.
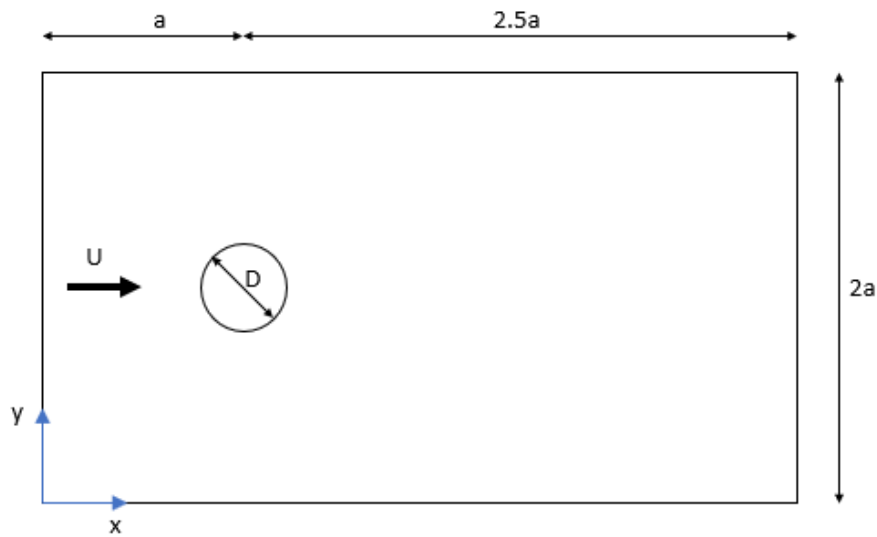
Figure 13: General domain design for computations past a two-dimensional circular cylinder

5.1 Modelling approach

The modelling of the domain geometry and generation of mesh is performed in HEXPRESS. The interface of HEX-PRESS can be seen in Figure 14.
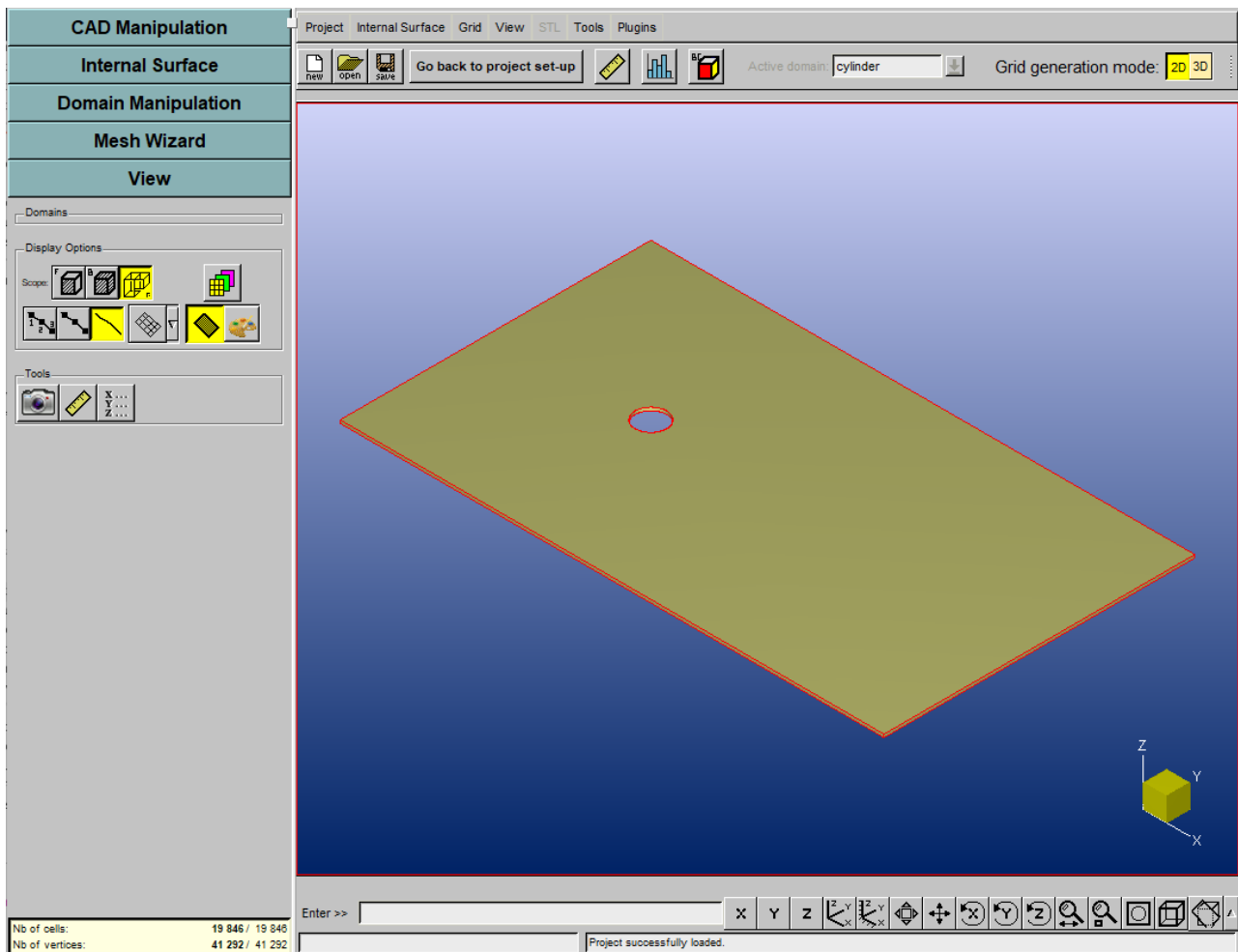
Figure 14: User interface in HEXPRESS visualized

For the current two-dimensional flow configuration as seen in Figure 13, the domain is created by generating a rectangular box and a cylinder at specified coordinate points. The cylinder before subtracting the geometry of the cylinder from the box-domain, all defined as a 2D domain. In addition, boundary conditions need to be defined. As for velocity boundary conditions, no-slip (zero velocity in both x- and y- directions) is specified on the cylinder surface. The inlet, lower- and upper wall of domain are specified with the constant velocity U=1. For pressure boundary conditions, the outlet is defined by a prescribed pressure. Specifically FINE/Marine allows you to choose a "frozen pressure", meaning that the pressure is constant and equal to 0 during the computation (Dirichlet condition). In addition, initial conditions need to be set for the simulation to be able to run. Velocity is specified by user for all cells to 1.0 m/s, while a reference pressure is defined as 0 Pa in all cells by default in FINE/Marine. The set up of

boundary conditions and initial condition is done in the solver of FINE/Marine, not in Hexpress.

In Hexpress, the mesh is generated in the following five steps: Initial mesh - adapt to geometry - Snap to geometry - optimize - viscous layers. This gives the users several options as to how to refine the mesh. The *initial mesh* generates a primary mesh over the whole domain, see figure below. The initial mesh is set to $\Delta_{X1} = \Delta_{Y1} = 0.5$m in all the simulations. In *Adapt to geometry*, you can choose the regions of the domain where you expect you will need a high level of refinements. In the present study, we are interested in the vortex shedding region behind the cylinder, so we insert a so called "box refinement". This is a rectangular box in the region in which you expect vortex shedding, and the program will refine a specified number number of times, which we in this report call N_{box}. In addition to the region behind the cylinder, we also want a fine mesh close to the cylinder surface in order to successfully to resolve the boundary layer. The user can specify the number of surface refinement levels, here called $N_{surface}$. The total number of refinement levels $N_{global} = N_{box} + N_{surface}$. For each refinement level, the element size is halved. You will know the element size closest to the cylinder at this point as

Figure 15: 5 steps of meshing process in FINE/Marine

$$\Delta_{finest} = \frac{\Delta_{initial}}{2^{N_{global}}} \tag{26}$$

Snap to geometry and *Optimize* adjusts the cell-geometries relative to the geometries and optimizes cell sizes in order to reduce potential numerical errors. *Viscous layers* is an important feature in Hexpress mesh generation - the user can here specify the required cell size closest to the cylinder surface inside the boundary layer, choose a stretching ratio and a number of refinement levels within the viscous layer, $N_{viscous}$. Here, the number of viscous refinement levels will be independent of the global number of refinement levels set earlier. Screenshots of the different mesh refinement stages in FINE/Marine can be seen in the figures below.

(a) Initial mesh   (b) Adapt to geometry   (c) Viscous layer

Figure 16: Different steps of mesh refinement in FINE/Marine

	Mesh properties	Computation 1	Computation 2	Computation 3	Computation 4	Computation 5	Computation 6
	Total nb of cells	1758	5504	7590	15708	16740	19846
Total properties	Initial level 1: x1, y1	0.5	0.5	0.5	0.5	0.5	0.5
	Inner level: x, y	6.25E-2	3.125E-2	1.5625E-2	1.5625E-2	1.5625E-2	7.8125E-3
Initial mesh	Nb of cells	35*20=700	35*20=700	35*20=700	35*20=700	35*20=700	35*20=700
	Global nb of ref.	3	4	5	5	5	6
Adapt to geometry	Box nb of ref.	2	2	2	3	3	3
	Surface nb of ref.	1	2	3	2	2	3
	Surface: first layer thickness	no	no	no	no	0.01	0.01
Viscous layers	Stretching ratio	no	no	no	no	1.2	1.2
	Number of layers	no	no	no	no	8	8

Table 2: Mesh refinement study, parameters variation

5.2   Mesh refinement study

A mesh refinement study must be conducted to ensure that you have a fine enough grid to resolve the flow properly. It is particularly important with small elements close to the cylinder in order to properly resolve the boundary layer. Both the shear force τ and vorticity $\bar{\omega}$ is proportional to the gradient of the velocity $\frac{du}{dy}$ - if the mesh is too coarse in the boundary layer, $\frac{du}{dy}$ will not be resolved properly, so τ and $\bar{\omega}$ will be inaccurate. For laminar flow around a circular cylinder the boundary layer thickness can be approximated as $\delta = \frac{1}{\sqrt{Re}}$. In this report Re = 100 and δ = 0.1. There should be 5-10 cells within the boundary layer, and the size order of adjacent elements should not be larger than 10%-20%. These are are rules of thumb presented in relevant lectures. If these rules are applied, we need to have elements closest to the cylinder in the size order Δ_x, Δ_y ~0.01 and element area ~0.0001. In the present study, we start by computing results using coarse grids, and then refining the mesh until we see a converging pattern in the outputs. Specifically we look for convergence in the drag coefficient. However, since the drag force is calculated based on an integration of the surface pressure, the results might represent some source of error. The validity of using the drag coefficient in the mesh convergence study is further discussed in the following. FOr the present refinement study, the domain size is set to a=5 (that is a domain size 17,5m x 10m) and time step Δt =0.01

It can be challenging to know which parameters to adjust in the mesh refinement study in order to get the optimal mesh. It is part of the exercise to get to know the different options by trial and error. We know that we want a mesh that resolves the boundary layer (a mesh with element size of ~0.01 close to the cylinder surface. We have however performed simulations with elements of larger order of magnitude close to the cylinder to see how it plays out in terms of results. A total of 6 runs with increasing number of refinements were performed, and the details from each run can be seen in the table in Figure 2.

If the the table in Figure 2 is studied in detail, it can be seen that in the first three computations keep the box refinement level constant at 2, while the number of surface refinements is increasing. From computation 4, the number of box refinements is set to 3, and surface refinement is increasing. For the last two computations, viscous layers are inserted. Note that we do not expect very accurate results for the first ~ 4 computations, since we know the inner level within the cylinder surface is larger than 0.01 and the boundary layer is therefore not fully resolved. But we still perform the computations to show that the results will converge when a fine enough resolution is achieved.

For each run, FINE/Marine writes an output file with the forces in x- and y- direction which corresponds to the drag-

and lift forces respectively. The drag coefficient (and similarly the lift coefficient) can be found by multiplying the mean force in steady state condition by a factor of 2, which can be seen easily from Equations 15 and 16 if you insert the known values of the parameters U, D and ρ (the density is also equal to unity, as discussed). For all the runs in Figure 2, the forces were oscillating like we would expect, which occurs because of vortex shedding. Oscillation starts to occur in steady state after $\sim$110 sec for all computations, see example in Figure 17b. Some computational effort could be saved if the velocity was not set precisely equal to 1.0 for all boundaries, but instead introducing some fluctuations in order to trigger unsteady behaviour at an earlier stage - this method can prove to be important when runner more computationally demanding simulations. The mean drag coefficient in each case is calculated and plotted as a function of number of elements in Figure 17a. The plot reveals that the drag coefficient is very sensitive to changes in mesh size before $\sim$17000 elements. We would actually expect the results to start to converge at this point, since a viscous layer is inserted to the in the mesh to ensure that the boundary layer is resolved. It would be wise in this case to perform one computation with even finer grid to ensure that results continue to converge. On the basis of this convergence study, we end up with the mesh properties of computation 5 - we will keep these mesh properties close to the cylinder surface (i.e number of box, surface and viscous refinements) when we now proceed to vary the domain size.
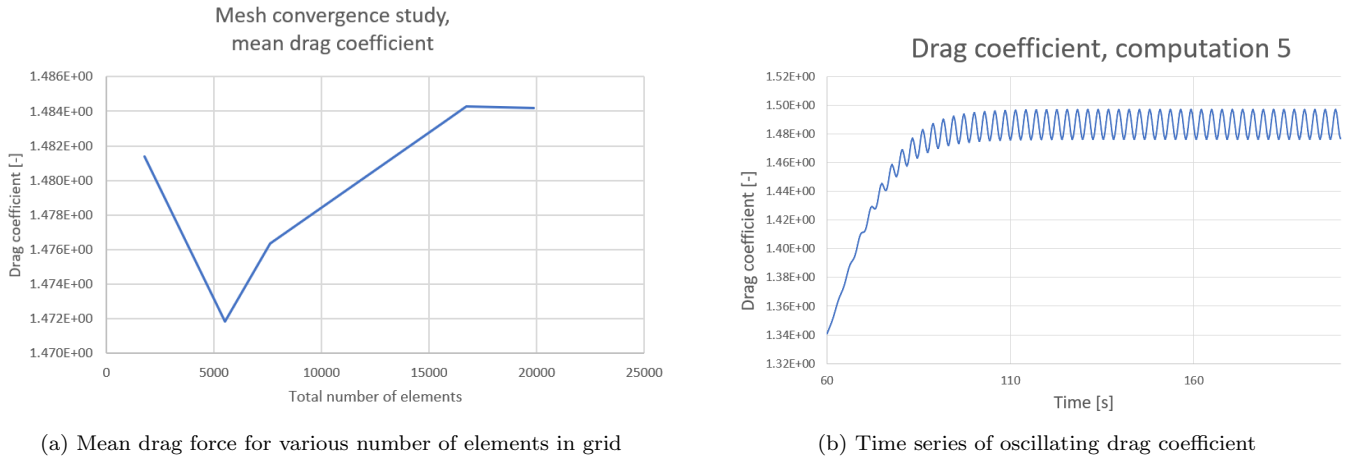
(a) Mean drag force for various number of elements in grid

(b) Time series of oscillating drag coefficient

Figure 17: Mesh convergence study based on mean drag coefficient

The results of the mesh convergence study anb the decided parameters are presented below:

<div style="display: flex;">
(a) 2D mesh, perspective view   (b) 2D mesh, close-up on cylinder surface
</div>
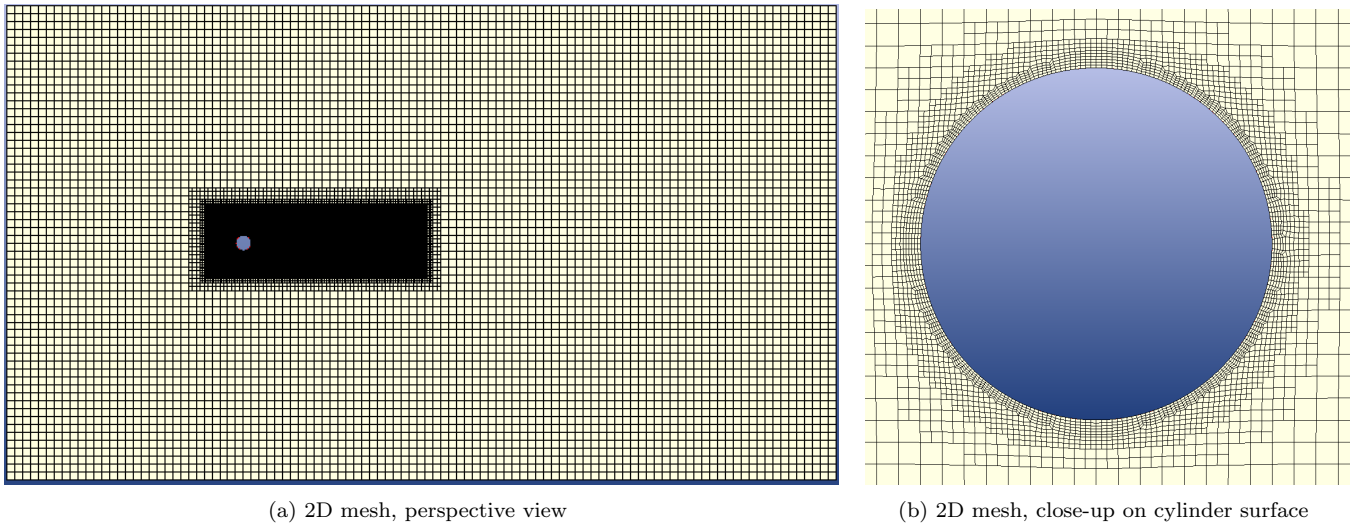
Figure 18: Mesh structure in the final domain design

	Parameter	Quantity
Initial mesh	Δx_1	0.5
	Δy_1	0.5
	Δz_1	Variable
Adapt to geometry	Global refinement	5
	Box nb. of ref.	3
	Surface nb. of ref.	2
Viscous layers	Inner layer thickness	0.01
	Stretching ratio	1.2
	Number of layers	8
Total properties	Total nb. of cells	16740
	Inner level	0.01
	nb elements on cylinder surface	256

Table 3: Mesh configuration parameters

5.3   Choice of domain size

Next step is to check how sensitive our results are when we vary the domain size. The domain should be as small as possible to have as few cells as possible and to save computational time, but not so small that the results are polluted. The results can be polluted if boundary condition in the walls (set to U=1) affect the nearby cells and then "propagate" all the way to the velocity close to the cylinder surface. The different domains tested here are a = 5, 10 and 15. In important point here is to apply the same grid refinement close to the cylinder surface even though the outer domain is being increased. The mean drag coefficient, RMS of lift coefficient and Strouhal number are compared for the 3 different domains. The velocity profile from the top of the cylinder radially outwards to the end of the domain was plotted to check if the velocity was converging towards 1 on the outer boundary of the domain.

The easiest way to modify the geometry of the domain by using the option "Domain Manipulation" in Hexpress. This ensures that the box refinement, surface and viscous refinement levels stay precisely the same even though the outer domain boundary is being increased. FINE/Marine cooperates very well when it comes to changing the domain size and still keeping fine mesh in the required boundary layer regions. The results from the runs of different domains in FINE/Marine can be viewed in Table 4.

Domain	a = 5	a = 10	a = 15
Number of elements	16740	22395	26513
C_D mean [-]	1.484	1.410	1.351
C_L RMS [-]	0.2273	0.2267	0.2256
St [-]	0.167	0.167	0.167

Table 4: Results for the tested domains; a = 5, 10 and 15.

Here, the drag coefficient and lift coefficient were calculated in the same manner as earlier, using only the stationary part of the time series (from 120-200 seconds). The Strouhal number is here calculated by placing a pressure probe on the top of the cylinder surface. The output is an oscillating pressure (much like the drag and lift forces). We can count these peaks within a certain time interval and compute the vortex shedding frequency and thus the Strouhal number. Counting may seem like an inaccurate way to gather results, however if the numerical values for the pressure variation is exported into Matlab, one can generate a plot and relate the peaks counted precisely to the corresponding time and thus get an accurate result. An imporant point to state here is that the time window for counting should in principle be long, otherwise one risk to loose a peak or not get a precise average. It is interesting to observe that the drag coefficient is very dependent on the changing domain size, indicating that checking the domain size is important to gather accurate results. The the lift is less sensitive to changing domain than the drag coefficient. The Strouhal number seems in our computations to be independent of the changing domain. There were precisely 6 seconds between each peak in the pressure probe plots. Based on these results, it seems that the magnitude of pressure and velocity is sensitive to changing domain size (because of changing C_D), however the separation frequency is very robust when it comes to domain changes (because of stable St).
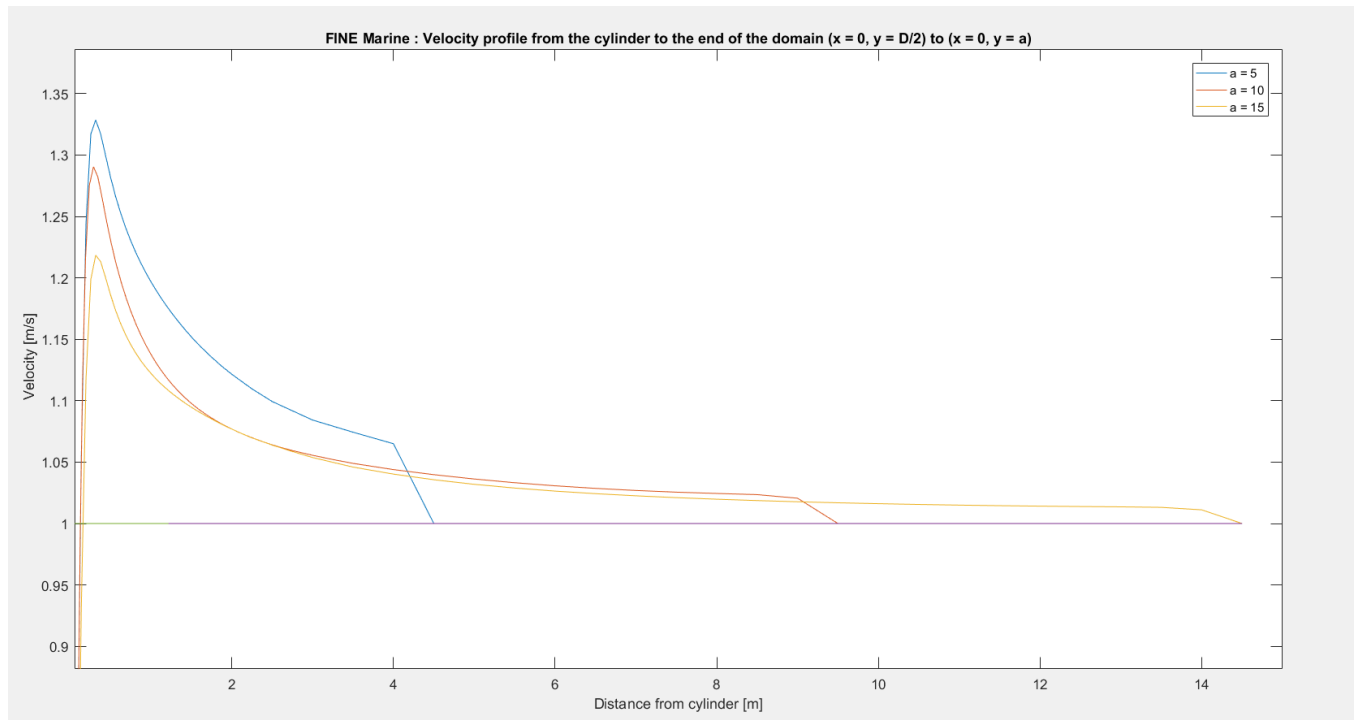
Figure 19: Comparison of velocity profiles for different domains

The velocity profiles radially outwards from the top of the cylinder from the three domain computations can be seen in Figure 19. This was done to capture how the horizontal velocity is effected by changing size of the domain. The boundary conditions on the outer wall of the domain was defined as $U_{inf} = 1$ m/s. For the velocity profile for the smallest domains (a = 5 and a = 10), the velocity close to the domain boundary does not reach velocity 1 m/s as it should, and a sharp "jump" in the graphs when approaching the boundary at y = 2a. This is a clear indicator that the domain is not large enough. For the domain with a = 15 the velocity converges towards ≈ 1.02, and transitions to 1 m/s at the boundary in a smoother way. This means there is a deviation of 2% on the boundary velocity for this case. For optimal results, the domain size should be even larger than a = 15. For further work a larger domain is recommended, but for the purpose of this assignment it is acceptable with the precision that a=15 provides. In addition, it can be seen in both figures that the maximum velocity is highly dependent on changing domain size. This observation fits well with the fact that the drag coefficient is highly dependent on the choice of domain.

5.4   Choice of time step

Another important parameter in CFD simulations is the size of the time step. We are solving the dependent Navier Stokes equation numerically, which means that time integration is performed. It is important to choose a time step which is small enough to ensure convergence. One way to check this is to apply Courant-Friedrichs-Lewy (CFL)

condition. This condition is given on mathematical form in one dimension and two dimensions respectively as

$$CFL = \frac{u_x \Delta t}{\Delta x} \leq C_{max} \tag{27}$$

$$CFL = \frac{u_x \Delta t}{\Delta x} + \frac{u_y \Delta t}{\Delta y} \leq C_{max} \tag{28}$$

where Δt is different time step applied, u is the velocity and Δx is the cell size. As mention earlier $u_x = 1$ m/s far away from the cylinder, but will vary around the cylinder, especially close to the surface of the cylinder. $u_y = 0$ in front of the cylinder but will vary around and behind the cylinder. The length Δx and height Δy of each cell depends on what part of the domain we are considering. In the current context, since the solver is explicit (time-marching), one must ensure that the Courant number in each cell in the entire domain is less than unity, that means less than 1. We have run all the previous analyses with time step $\Delta t = 0.01$. In this section we will check the sensitivity of the drag coefficient, lift coefficient and Strouhal number with respect to different time steps. We have performed simulations for $\Delta t = 0.02$, 0.05 and 0.001 and compute the mentioned parameters and the Courant number in each case.

In FINE/Marine, there is an option of computing the Courant number for every timestep in a simulation. In the current version of FINE/Marine, the option is only available for multifluid simulations, and not monofluid like in the current problem. It is likely that the problem is fixed for the next version of FINE/Marine and the function can hopefully be utlized in future computations. But for now, another method was applied for the purpose of this problem. By looking at the equation for the Courant number (Equation 27) you can see that the highest possible Courant number will occur when you choose a large velocity and a small element size - this immediately tells us that the region close to the cylinder surface is critical with respect to getting a Courant number smaller than unity. For each computation with varying Δt, we plot the x-velocity profile from the cylinder surface and radially outwards from the surface (Figure 19). By collecting the maximum velocity and the grid cell size at this point, the Courant number is approximated for each time step. Table 5 display the resulting drag- and lift coefficients, Strouhal number and Courant number from each of the simulations. The current simulations are performed with the chosen grid resolution from the mesh convergence study along with the appropriate domain with parameter a=15. The total number of elements was 26513 for every run with varying time step.

Time step Δt	0.001	0.005	0.01	0.02
C_D, mean [-]	1.350	1.351	1.349	1.378
C_L, RMS [-]	0.2248	0.2249	0.2256	0.2254
St [-]	0.167	0.167	0.167	0.167
CFL [-]	0.062	0.302	0.602	1.206

Table 5: Results from testing different time step Δt.

As we can see from the Table simulations with Δt=0.01 and lower yield results with Courant number lower than 1.

Based solely on this, one could say that it would be sufficient with this time step. However, the requirement is that the CFL number should be "significantly smaller than 1", and we should check the other parameters' sensitivity to varying time step in addition. By looking at the drag coefficient, we can see that it is slightly different in the runs. It can be seen that the drag coefficient is quite sensitive to changing the time step from 0.02 to 0.005. For time step lower than 0.005 however the sensitivity is much smaller, with only 0.2 % deviation going from $\Delta t = 0.005$ to $\Delta t = 0.001$. It seems that the lift coefficient is less sensitive to changing the time step. The deviation of RMS of C_L from $\Delta t = 0.005$ to $\Delta t = 0.001$ is only 0.04%. The Strouhal number is very robust to changing time step as well according to our simulations. However, as discussed earlier, the method of calculating Strouhal number may involve some error, as discussed in the previous section (i.e counting peaks in the time series of pressure). Based on this discussion, it seems wise to choose Δt=0.005 as we see that the parameters are not very sensitive to changing time step below this threshold, in addition to having CFL≈0.3 which is significantly lower than 1.

6 Straight cylinder, 3D simulation

6.1 Problem description

The flow around a three dimensional straight cylinder has been simulated, serving as a case study in the preparation of performing flow with more complex geometry. Simulations are performed using the laminar model in FINE/Marine at Re = 200 and Re = 300, including testing of simulation parameters such as length of cylinder and boundary conditions, and some different mesh configurations. This is done to investigate the numerical sensitivity to these parameter variations. The flow regime occurring for these Reynolds numbers are characterized by the transition in the wake behind the cylinder and the formation of streamwise vortices of modes A and mode B (see Section 3 for further details). Figure 20 illustrates the domain set-up for these straight cylinder computations. Domain dimensions and other flow parameters are displayed in Table 6. The domain parameters of the two-dimensional horizontal xy-plane have been settled based on the mesh convergence study presented in Section 5.3. The spanwise length of the cylinder however, L_Z, is a new domain parameter that needs to be investigated in the following simulations.
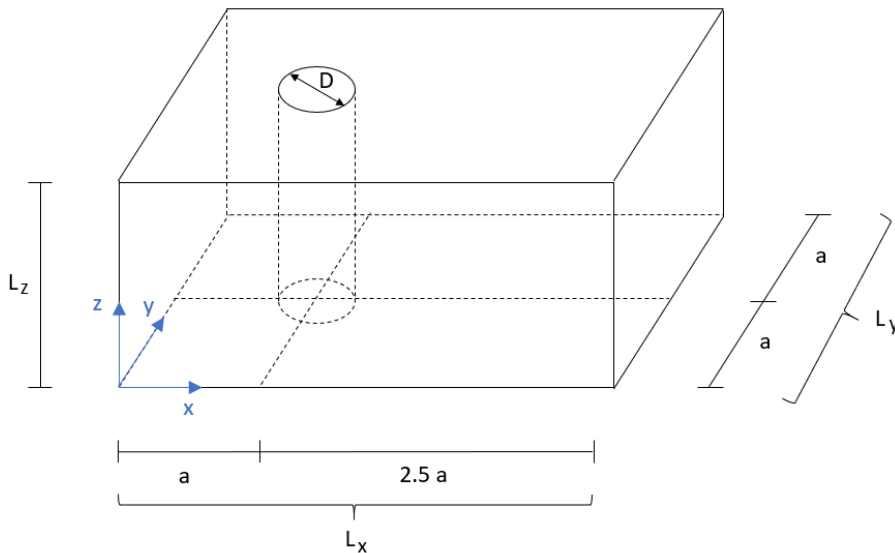
Domain parameters

a	15 m
Domain length, L_X	52.5 m
Domain width, L_Y	30 m
Diameter, D	1 m
Domain height, L_Z	Variable

Flow parameters

Flow velocity, U	1 m/s
Density, ρ	1 kg/m^3
Dynamic viscosity ν	Variable

Table 6: Domain and flow parameters for straight cylinder simulations

Figure 20: General domain design, straight cylinder simulations

6.2   Grid generation considerations

Just as the horizontal domain dimensions, the 2D mesh properties have also been based on the findings in the earlier convergence studies (see Section 5.2). The previous mesh topology consisted of a combination of box refinements, surface refinements and viscous layers to resolve the boundary layer and two dimensional wake details. In the current simulations, it is also a concern to resolve the three dimensional flow phenomena such as streamwise vortices, which require a fine enough mesh resolution also in z-direction as well. The most obvious mesh parameter that needs to be settled for three dimensional flows is therefore the element size in this spanwise direction. If you multiply the number of elements in the horizontal plane by the number of elements in z-direction, you quickly realize that this parameter will largely impact the computational cost of the simulation. Another parameter that will be investigated in the following section is the size of the box that refines the flow around the cylinder and in the wake. In the previous 2D case study, this parameter was settled based on guidance from more experienced users of FINE/Marine. In the current simulations there is a more pressing demand of reducing elements in order to spare computational time and resources, and so the required size of the box refinement needs further investigation. There is a consistent compromise of choosing a computational domain and mesh that gives results of sufficient precision, while at the same time running simulations at an acceptable computational cost. With these concerns in mind, some further testing with three dimensional meshing aspects is in demand. In all the present mesh sensitivity checks, a spanwise domain length $L_Z = 12D$ was applied for Re = 200. These parameters will be further investigated in upcoming sections, but are kept constant throughout these primary grid testing simulations. Figure 21 shows a general grid configuration of the present straight cylinder simulations and Table 7 summarizes the applied mesh parameters along with the remaining parameters (termed "variable" in the table) to be investigated in the following.

(a) 3D mesh straight cylinder, perspective view   (b) 3D mesh, cutting plane at cylinder centre (x = 15 m)
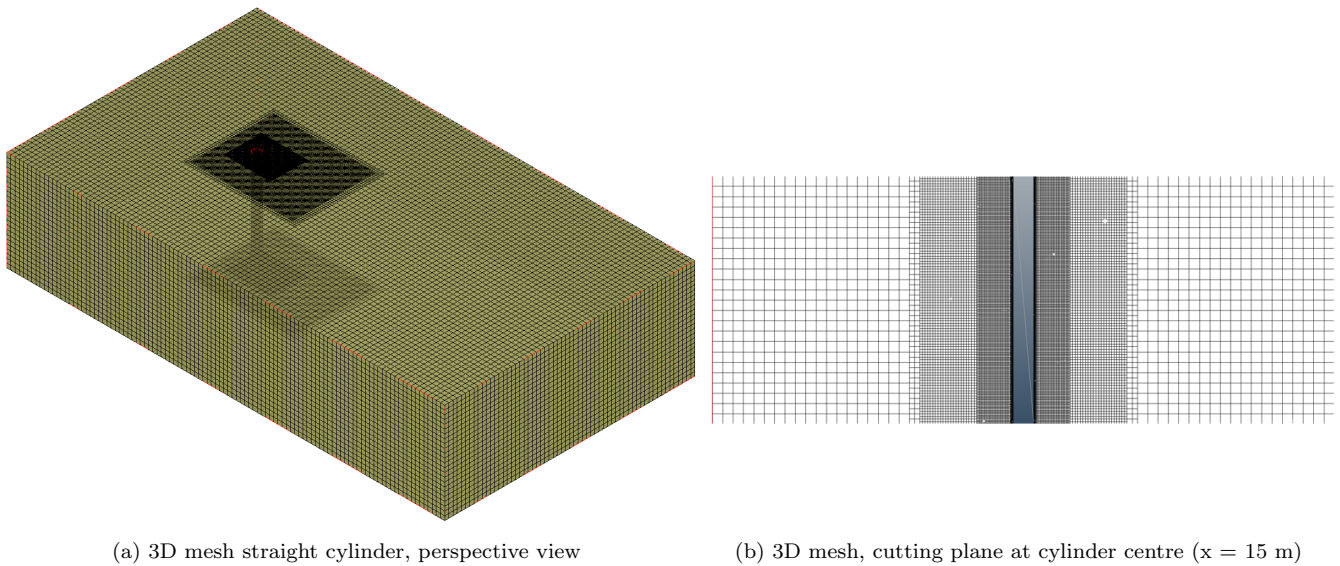
Figure 21: Mesh overview in 3D straight cylinder simulations

	Parameter	Quantity
Initial mesh	Δx_1	0.5 m
	Δy_1	0.5 m
	Δz_1	Variable
Adapt to geometry	Global nb. of ref. lvl.	5
	Box nb. of ref. lvl.	3
	Box dimensions	Variable
	Surface nb. of ref. lvl.	2
Viscous layers	Inner layer thickness	0.01
	Stretching ratio	1.2
	Nb. of viscous layers	8

Table 7: Mesh parameters straight cylinder simulations. Parameters to be decided in the upcoming discussions are labeled "variable".

6.2.1 Refinement in the spanwise direction

The number of cells required in the spanwise direction in the simulation of a the flow around a circular cylinder is linked to several factors, depending on the required level of flow detail and which parts of the domain is the main focus. If we consider the boundary layer and separation, the refinement level in the horizontal plane is can arguably be more important than in the spanwise direction, seeing that separation mainly occurs in the same direction as the flow. There is however a possibility of oblique vortex shedding. Factors that can affect the initiation of oblique vortex shedding are Reynolds numbers, boundary conditions and the spanwise length of cylinder/domain (Williamson [1988a], Leweke and Provansal [1995]). It is likely that the refinement level along the spanwise length of the cylinder could be an decisive factor with respect to the nature of separation.

Not only the boundary layer and separation regions need a fine mesh resolution. The wake also requires an adequate level of refinement in the spanwise direction in order to capture the three dimensional flow phenomena such as streamwise vortex formations. As a general rule of thumb in generating mesh along the spanwise length of a cylinder, it is said that minimum 30-40 elements per diameter is required to capture the above mentioned flow features. A sensitivity check to spanwise refinement level in simulations in FINE/Marine is nevertheless in demand, and can provide useful knowledge for future simulations.

When discussing the required number of cells in z-direction, it is convenient to compare the cell size in the vertical direction to the respective sizes of the cells in the horizontal plane (x- and y-directions). The ratio of the cell sizes in various directions is in the present report named cell aspect ratio α, defined based on the relationship between the initial cell size in z- and x-direction, such that

$$\alpha = \frac{\Delta Z_1}{\Delta X_1} \tag{29}$$

Even though the above formula refers to the ratio between the cell sizes of the initial mesh, the aspect ratio will remain constant in the entire domain. Mesh refinement in HEXPRESS occurs in the same manner in all directions, meaning that the aspect ratio will be constant all the way to the inner layers (viscous layers) of the mesh.

When discussing the goodness of a mesh in general, the aspect ratio is often an important factor to keep in mind trying to avoid cells with large aspect ratios, pointy edges or any other unwanted shapes giving potential numerical error. The preferred choice is most often to have an aspect ratio close to 1 in the entire domain. Generating a mesh with α=1 for the present simulations will have a high computational demand. A higher aspect ratio could potentially give acceptable results as well, and needs to be tested. Another rule of thumb often used is that 30-40 elements in spanwise direction per diameter is needed to resolve three dimensional flow phenomena. Using this as a guideline, α = 2 should be sufficient.[2]. Based on these considerations we proceed to evaluate aspect ratios $\alpha = 4, 2$ and 1. The grid generated in these three cases are illustrated in Figure 22 along with the number of cells per mesh. Each time the aspect ratio is halved, the total number of elements is doubled. This highlights the importance of investigating the simulation sensitivity to changing element size in z-direction.

| (a) $\alpha = 4$, 16 elt per D | (b) $\alpha = 2$, 32 elt per D | (c) $\alpha = 1$, 64 elt per D |
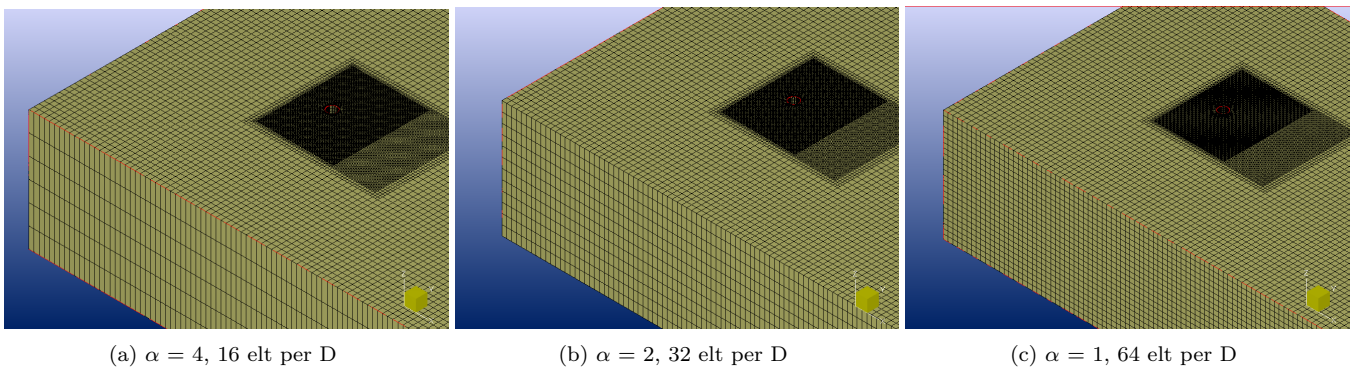
Figure 22: Mesh generation with various aspect ratios, $\frac{\Delta Z_1}{\Delta X_1}$. Simulation were run using $L_Z = 12$D and Re = 200.

The goodness of the mesh with various aspect ratios can be evaluated based on different criteria. One way is to visually observe if the wake generated in the different cases resemble the expected three-dimensional mode A with similar properties as described in the paper of Williamson [1996]. The figures below give visual comparisons of the resulting flow regimes based on the vortex detecting-parameter $\lambda 2$.

---

[2]This can be calculated by taking $\Delta Z_1 = 1$, so that inner refinement level has a size $\Delta Z_1/2^5 = 0.03125$, such that 1 / 0.03125 = 32 elements per diameter

(a) $\alpha = 4$

(b) $\alpha = 2$

(c) $\alpha = 1$
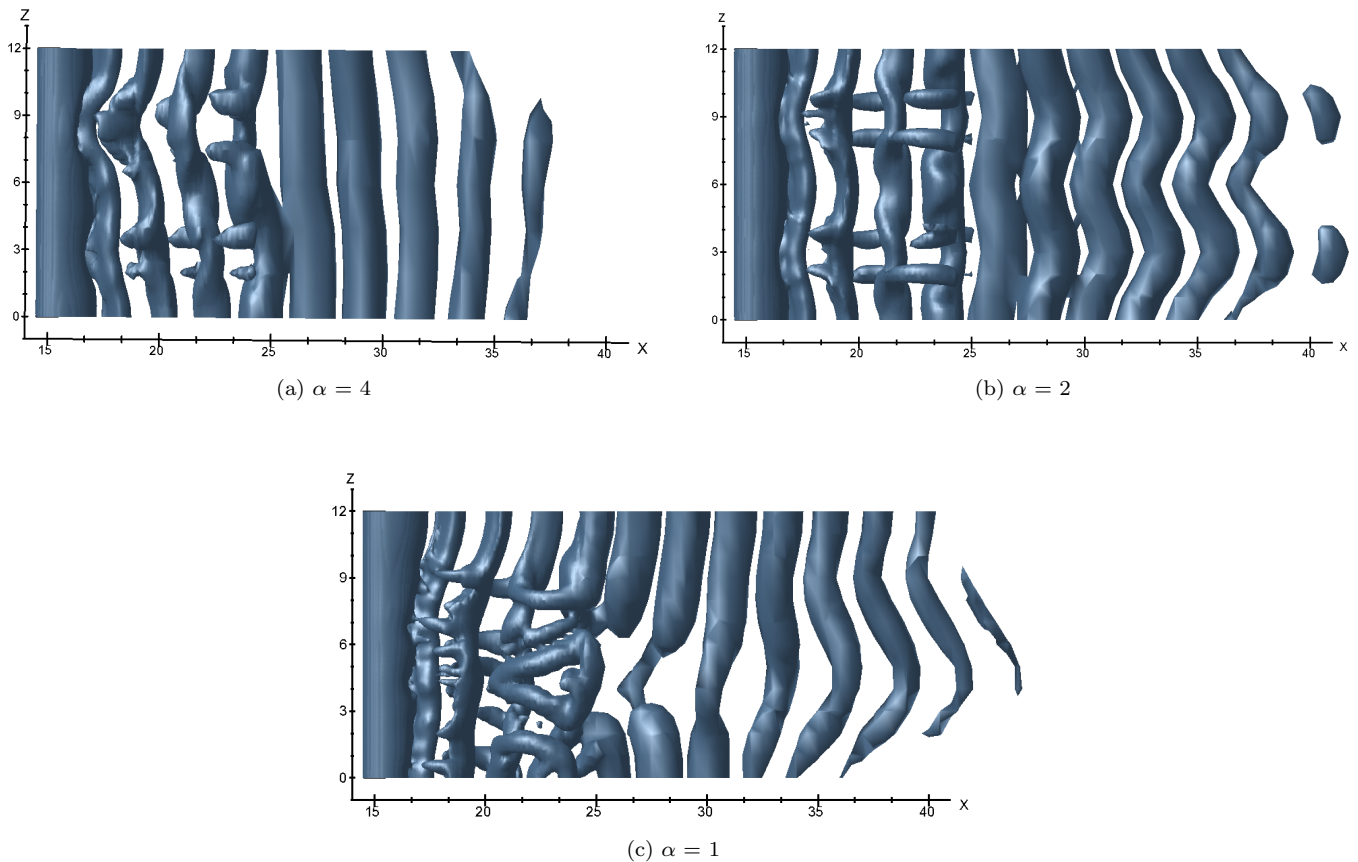
Figure 23: Vortex detection with $\lambda 2 = -0.01$, Re = 200 simulation at timestep t=200, for different aspect ratios

These visualizations indicate that in fact all three values of α captures three dimensional streamwise vortices characteristic for the TrW regime. For $\alpha = 2$ and 4, the streamwise vortices appear to be quite regular and have wavelengths of 3-4 diameters between each finger, which is in good agreement with the mode A descriptions by Williamson [1996]. They do however exhibit some differences as well, where $\alpha = 4$ show signs of connected fingers, as if they appear to "melt together" into one larger three dimensional structure approximately at position (x,z) = (18,9) in Figure 23a. $\alpha = 2$ provides more clearly separated, parallell streamwise vortices. The flow visualization of the $\alpha = 1$ yields a more complicated, unstructured wake regime. At this point, it is clear that the smaller aspect ratio makes the flow more susceptible to perturbations, causing a more irregular wake. These result are only snapshots of the flow regime at a certain point during the simulation, and the wake may exhibit different features if the simulation is run for a longer. Some further parameter testing could be performed on these various aspect ratios for further work, but it is in the present concluded that $\alpha = 1$ probably will reveal more wake details and give more reliable results than larger aspect ratios.

6.2.2   Box refinement trials

The mesh resolution around the cylinder and in the wake is another parameter that may affect the flow greatly. In the present simulations, a box refinement is applied that is placed such that it surrounds the cylinder. The immediate question that arises is the required box size in order to capture the desired amount of flow detail. Reducing the size of the box refinement will reduce computational time, but reducing it too much could pollute the results in the sense of not properly resolving the flow detail and thus introducing numerical error. In order to investigate the influence of the size of the box refinement, a few trials with varying box dimensions are compared to each other. In all the simulations, there are two levels of box refinement, one "outer" and one "inner". Only the size of the "inner" box has been varied, that is where the mesh is finest. Figure 24 and 25 display the three tested mesh configurations and the respective box dimensions. Note that the figures below are zoomed in screenshots of the mesh. All other parameters are kept constant, including the cell aspect ratio $\frac{\Delta Z_1}{\Delta X_1}$ which is taken as $\alpha = 2$ in all present simulations.

| (a) Box 1 mesh | (b) Box 2 mesh | (c) Box 3 mesh |
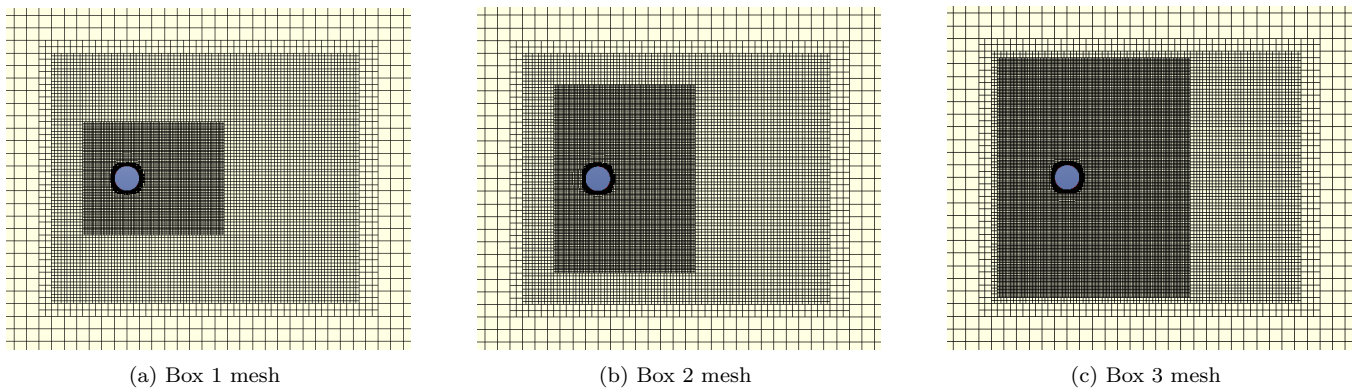
Figure 24: Mesh generation with variations in box refinement

| (a) Box 1 dimensions | (b) Box 2 dimensions | (c) Box 3 dimensions |
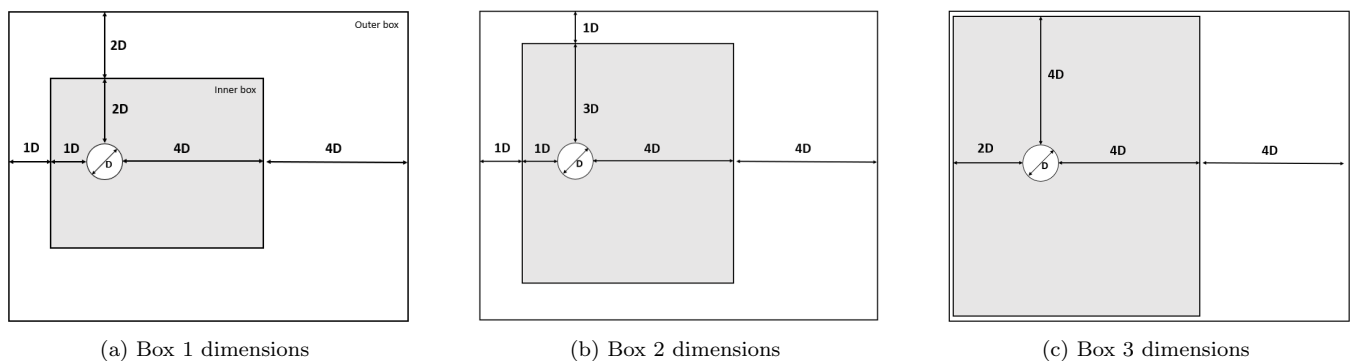
Figure 25: Box refinement dimensions

Figure 26 illustrates how the streamwise vortices are resolved compared to grid resolution. There is a clear difference in vortex formation between the different levels of mesh refinement. The initial mesh (outside the box refinement)

is clearly too coarse to resolve any three dimensional phenomena, and only two dimensional vortex filaments are generated. There is also a difference within the box refinement levels, where the inner box resolves the streamwise vortices to a finer level than the outer box. This might not be easily seen from Figure 26 itself, but studied by dynamic view in CFView illustrated clearly that there were more wake details behind the finer mesh.

The differences between the three box refinement simulations are however not reflected when comparing the average resulting force components on the cylinder. Resulting mean values of drag coefficients are presented in Table 8. These results indicate that the different box configurations have very little effect on the resulting force components. There is some small percentage deviation between the values of C_D, but this is most likely only a consequence of the long period oscillations present during the simulations (see Section 6.5 for details). The question of which box refinement to choose boils down to the desired level of flow detail in the wake. If a well-resolved far wake is in demand, a wide box refinement should be applied. However if the resulting forces on the cylinder is most important aspect of the cylinder, box 1 refinement seems to be sufficient. Some further parameter comparison could have been included in order to examine the differences in more detail.

	Box 1	Box 2	Box 3
C_D	1.253	1.274	1.265

Table 8: Drag coefficients for different box refinement configurations
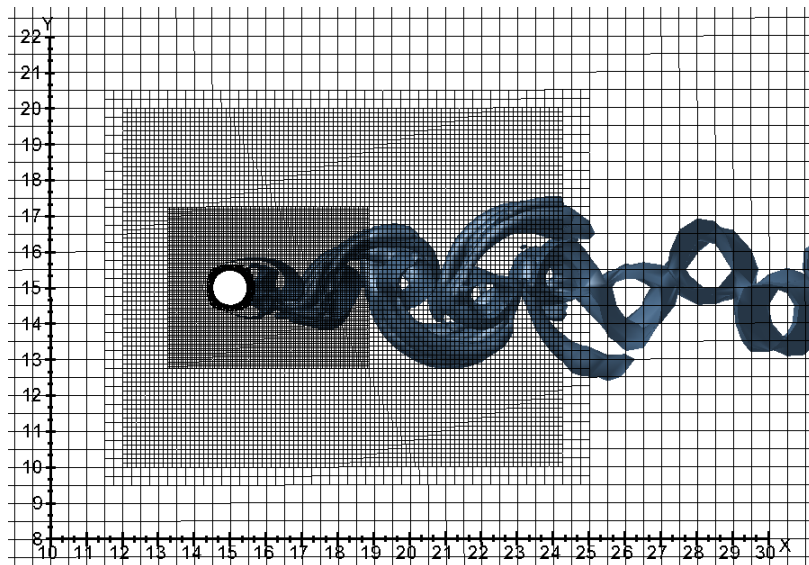
Figure 26: Box refinement visualization compared to vortex formation in wave

6.2.3   Adaptive grid refinement

Adaptive Grid Refinement (AGR) is a special mesh refinement algorithm available in the set-up of a simulation in FINE/Marine. This feature enables the grid to automatically resolve during a simulation within the regions of high

flow activity in the domain. Areas that demands a fine mesh at a certain time instant is then refined to the required resolution. When there is little activity, which in essence means no pressure or velocity gradients, the refinement level is reduced to save computational time. Different refinement criteria can be applied based on the flow case at hand, where the "Flux component Hessian" is most normally used for wake flows similar to the study of circular cylinders. Further information on AGR can be reviewed in the documentation of FINE/Marine.

(a) Mesh resolution using AGR

(b) Streamwise force component history (F_X)
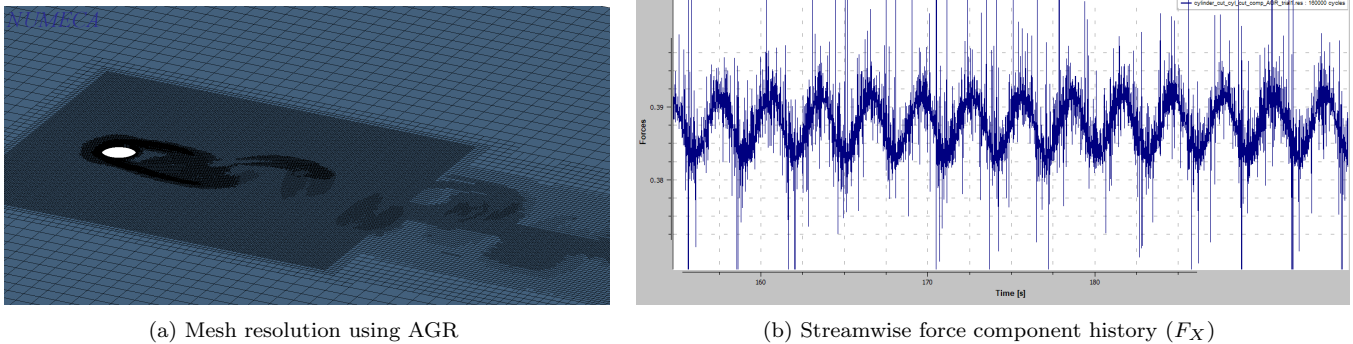
Figure 27: Adaptive grid refinement: Instantaneous mesh refinement illustration and resulting body force in x-direction

An effort was made to get AGR to work on the straight cylinder flow case. The motivation behind this was to further reduce the amount of cells in the computations by only resolving the regions which actually require a fine mesh. An issue of frequently appearing spikes in the force history of the AGR-simulations presented itself, which clearly introduces error sources to the results. Several alternations to simulation parameters were tested to investigate the origin of these spikes, with some improvement and a smoother force history. However, some spikes were still present in the simulations, and the results with AGR were not satisfactory enough to pursue this option further due to time limitations. There is a potential benefit with respect to reducing the required number of cells in the mesh and reducing the computational time, but further investigation of the sources if the described spikes in the simulations is in demand.

6.3   Length of straight cylinder

Previous studies of the flow around straight cylinders, both experimental and numerical, have revealed that the cylinder length will influence flow behaviour greatly. Sufficient cylinder length is required in order to trigger three-dimensional flow development. Mode A shedding is known to appear at spanwise spacing of 3 - 4D, indicating that the minimum length of cylinder should exceed one such wavelength. Earlier numerical studies (Thompson et al. [1996], Karniadakis and Triantafyllou [1992]) discuss the matter to some extent, where spanwise lengths of 2πD proved a sufficient length to initiate Mode A, while πD was insufficient at that. Simulations in this project have been performed with spanwise lengths 4D, 8D and 12D at Reynolds number Re=200. Other simulation parameters, such as two-dimensional domain and boundary conditions, have been kept constant according to Table 6. The initial mesh has elements of equal size, that is $\Delta X_1 = \Delta Y_1 = \Delta Z_1 = 0.5$, with aspect ratio $\alpha = 1$. Simulations have been

run with timestep $\Delta t = 0.01$ for 200 s (20000 timesteps). The figures below illustrate how the vortex development appear in the wake behind the cylinders with the various spanwise lengths at the last timestep in the simulations.

(a) 4D

(b) 8D

(c) 12D
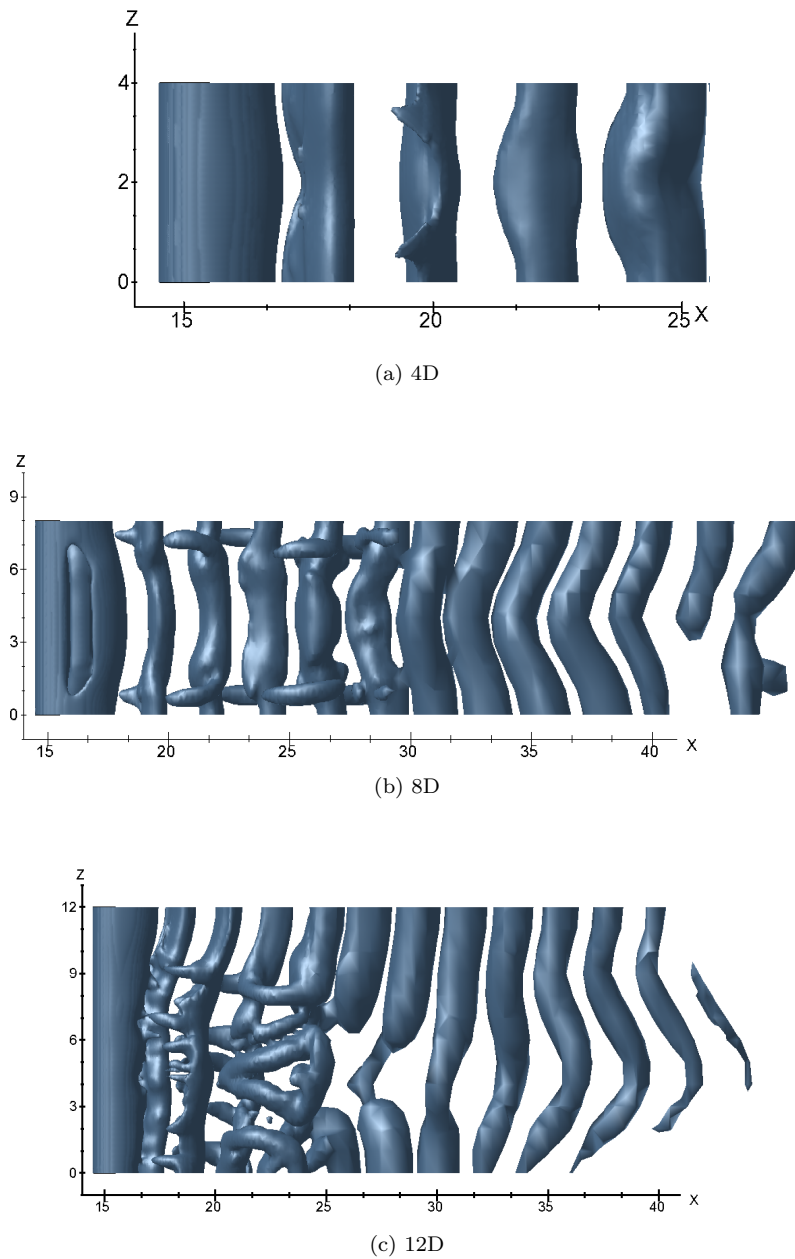
Figure 28: Vortex detection with $\lambda 2$ = -0.01, Re = 200 simulation at timestep t=200, for different cylinder lengths

The figures illustrate that the spanwise length of the cylinder has a large impact on the simulation results. It is quite clear that neither the lengths of 4D or 8D fully resolves the three dimensional vortices expected in mode A. The length of 4D completely is clearly not sufficient as to develop these expected fingers, although there is some instability in the simulation causing visible signs of three dimensional vortex shedding, but they are not fully developed. In the

8D-case, the streamwise vortices develop more properly, but they seem to only occur close to the domain boundaries and clearly have a larger spanwise length scale between them than what is expected for mode A. The 12D case exhibit more developed three dimensional effects. It was somewhat surprising that the shorter spanwise lengths were insufficient as to produce better results based on the knowledge of shorter lengths have been successfully performed in earlier research. Further investigation of the reason behind this was not prioritized - thus a 12D spanwise length was deemed the preferable choice among the tested cylinder lengths.

6.4   Boundary condition effects

Previous research on the topic of flow past straight cylinders have discussed the importance of boundary conditions in numerical simulations. The faces of the domain where the cylinder ends are situated are of special importance. Studies by Miliou et al. [2007] and Jiang et al. [2018] illustrated how the boundary conditions affected the flow in the convex and concave curved cylinder. The unique feature of this configuration is the appearance of a free-end in either the inlet or the outlet of the domain. In the straight cylinder simulation this is naturally avoided. This is also the case for the upcoming curved cylinder computations in cross-flow.

There are essentially two types that are frequently used to model the cylinder ends: Periodic and symmetric boundary conditions. Only the latter option is used in the simulations. The reason why periodic boundary conditions were not tested is because this type of BC was not available in the version FINE/Marine (7.2) that was used for the present work. One type of boundary conditions that however is available in FINE/Marine is the free-slip. A simulation was in fact run with this kind boundary condition, but the resulting flow field was very similar to the simulations using the mirror boundary. The difference between these two boundary conditions is according to the documentation of FINE/Marine that the mirror type is not incompatible with "rigid mesh displacement", while the slip-condition is. It is recommended to study this documentation for further knowledge on this topic []. For the practical purposes of this flow configurations, the two types can be considered equivalent. The mirror boundary condition is applied for the cylinder ends in the furhter work.

6.5   Simulation stability considerations

Up to this point we have made adjustments to several simulation parameters in order to see the influence on flow behaviour. One flow feature which seems to be independent of any of the above tested parameters, is that the drag force seems to experience fluctuations of transitions between flow phases throughout the time series. Figure 29 illustrates how the drag coefficient changes throughout the simulation. One can study the flow at different stages and observe the corresponding flow regimes. In the present example, the flow first takes the form consisting of only primary two-dimensional vortex filaments, before it transitions to three dimensionality at 130s. During this transition, the drag coefficient drops significantly and the wake exhibit some unstable features that is probably a numerical feature and not a real flow regime. After the transition, three dimensional streamwise vortex shedding is present, although these unsteady transitions keep occuring for as long as the simulation is run. In the study of Williamson [1996], the wake never becomes completely periodic during the TrW regime, with occasional cases of

vortex dislocations being present. However the fluctuations observed in Figure 29 looks to be caused by some other phenomena than merely occurrences of dislocations. It is believed that these long period oscillations originate by some numerical truncation error or something similar, but the actual source of the phenomena was not discovered.
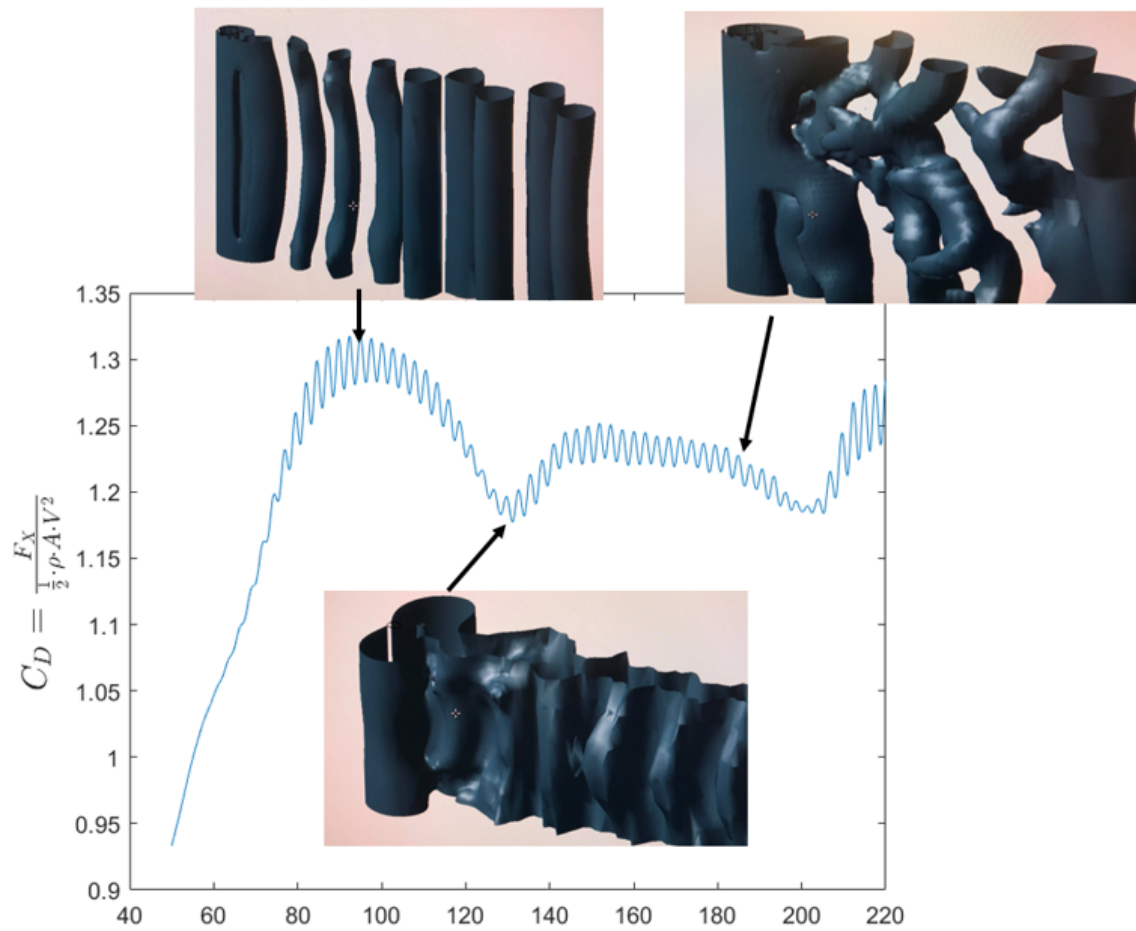
Figure 29: Drag coefficient time history for a simulation with 12D spanwise length at Re=200, illustrating different flow phases occuring throughout the simulation

6.6   Overview of results from straight cylinder simulations

In the present section, a summary of the general findings of the straight cylinder simulations are presented. All simulations performed up to this section has lead to the preferred simulation set-up. A spanwise length of 12D is applied, an aspect ratio of α=1 is adopted with a box refinement practice equivalent to "box 1" described earlier is applied. It is assumed that these tuned domain- and mesh parameters are applicable also for simulations at Re = 300, although all testing was performed for Re = 200. The current simulation set up and main results for the two cases of Re = 200 and 300 are summarized in Table 9.

Final mesh parameters

Initial mesh	0.5 m
Inner viscous layer thickness	0.01 m
Nb. of elements around cylinder	259
Nb. of elements per spanwise diameter	64
Total nb. of elements	

Simulation results

Reynolds number	200	300
Strouhal number, St	0.185	0.200
Drag Coefficient, C_D	1.266	1.273
RMS of Lift Coefficient, C_L	0.323	0.293
Base pressure coefficient, -Cpb	0.801	0.921

Table 9: Comparison of numerical parameters for different cell aspect ratios

The Strouhal number is calculated based on velocity probes placed in at a distance of 1D behind the trailing edge in near-wake of the cylinder. A Fast Fourier Transform (FFT) of the velocity component u reveals the Power Spectral Density (PSD) of present frequencies. Although there is some low frequent noise in the time series, there is a clear dominating frequency that is equivalent to the vortex shedding frequency. The PSD of the relevant case for Re = 200 is included in the Appendix. The present vortex shedding frequencies for the two simulations are in reasonably good agreement with previous research. The Strouhal number during mode A is lower than mode B, which corresponds well with the Strouhal numbers at Re = 200 and Re = 300 in the St-Re relationship in the TrW region as defined by Williamson [1996] (see Figure 6 in Section 3).

The drag coefficient is not discussed extensively for the TrW range in Zdravkovich [1997], but a plot is included where the value of C_D is predicted to be within the range of 1.25-1.30 for both Re = 200 and 300 based on various experimental results. The calculated values of C_D in the present simulations are both within this range. The base pressure is another frequently used parameter to characterize the flow regime. A detailed plot of values of -C_{pb} for the TrW range is included in Williamson [1996]. The experimental values are here given as -C_{pb} = 0.78 for Re = 200 and -C_{pb} = 0.95 for Re = 300 (values read directly of a plot). The numerical values in the present simulations provide result with deviations of 2.7 % and 3.1 % deviations in -C_{pb}, which is relatively close. There is however a significant

source of error in the averaging of the simulations parameters, as a result of the long period oscillations/instabilities presented in Section 6.5.

Figure 30 compares the wake development from the simulations of the different Reynolds numbers at a snapshot at t = 200s after start. Mode B vortex shedding is very well captured, with streamwise vortex formations with quite evenly spaced at 1D wavelengths, which is in good agreement with visualizations from the study of Williamson [1996]. This mode is easily initiated and quite stable. The simulations at Re = 200 resemble Mode A as described by Williamson [1996], although the streamwise vortices are not as evenly spaced at 3-4D as the study would indicate. For some reason this mode exhibit more unsteadiness than mode B in the present simulations. This can again be traced back to the discussions of the stability of the simulations as described in Section 6.5, which also introduces also a significant source of error in the averaging of the simulations parameters such C_D, C_L and $-C_{pb}$.

(a) Mode A at Re = 200

(b) Mode B at Re = 300
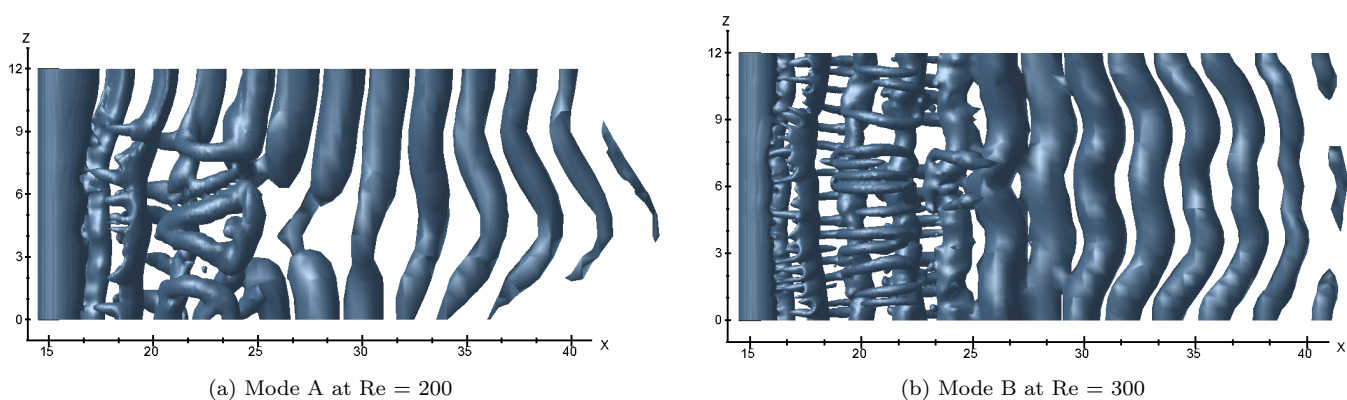
Figure 30: Vortex detection $\lambda 2$ = -0.01 at for straight cylinder simulation at Re = 200 and Re 300

7   Curved cylinder, 3D simulation

7.1   Computational setup

The main objective of this master thesis has been to perform a numerical simulation in FINE/Marine of a curved cylinder placed in a uniform crossflow. The present work represent one of the first studies performed on this flow configuration. The study involves only low Reynolds numbers, namely Re = 200 and Re = 300, which are the same Reynolds numbers as were the topic of the straight cylinder simulations. This gives the opportunity to investigate how the curvature affects the wake development at these low flow rates compared to the respective straight cylinder simulations. A horizontal, straight extension to the curved cylinder has been included in several simulations. Based on earlier obtained knowledge both from literature review and previous simulations, it is know that end-effects and choice of boundary conditions can greatly affect the flow development. Including a straight extension to the curved cylinder can potentially minimize the end-induced effects in order to capture only the intrinsic induced flow features due to the cylinder curvature. Various lengths of the straight extensions are tested. An illustration of the flow configuration and domain layout can be viewed in Figures 31 and 32 along with numerical values of various parameters in Table 10.
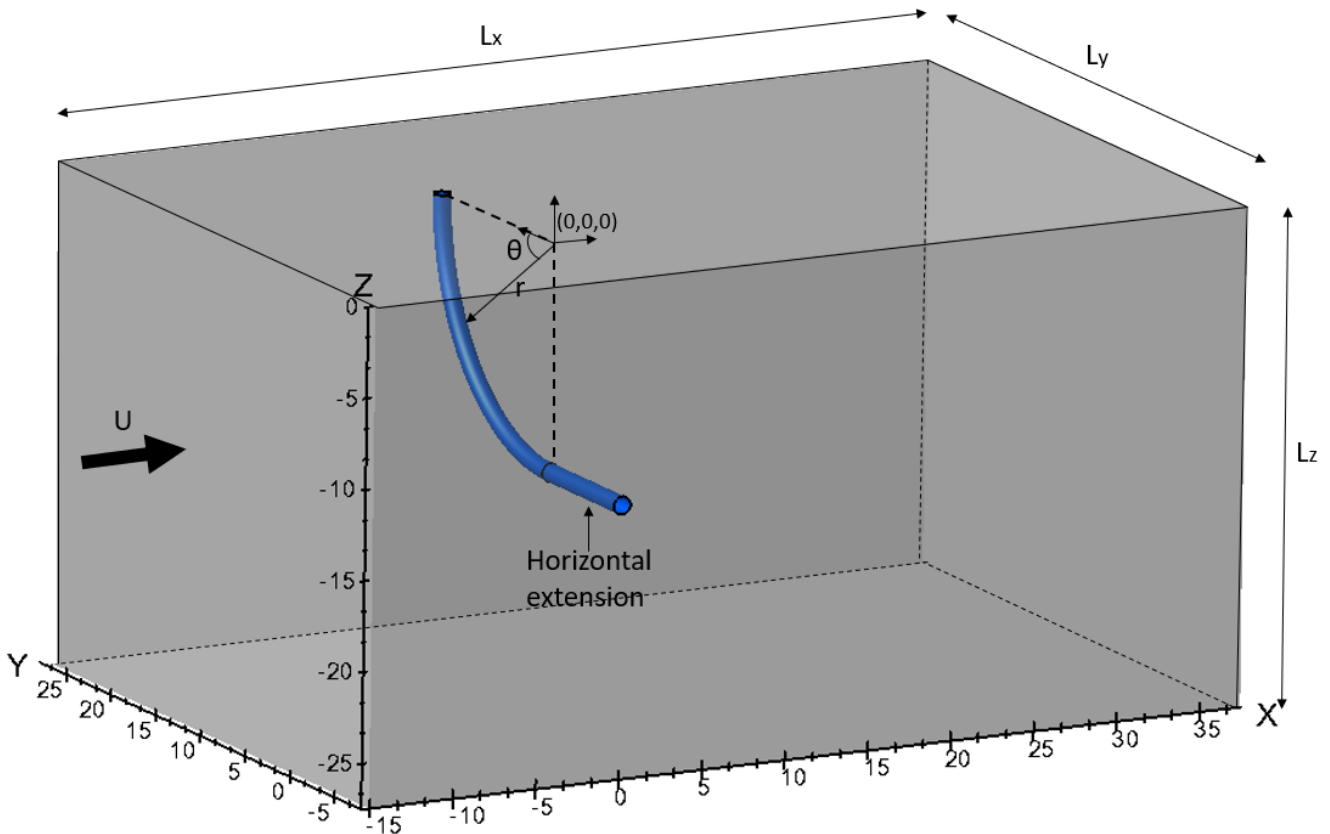
Figure 31: Three dimensional view of domain for curved cylinder simulations. Notice that axes and coordinates are shown along the edges of the domain, although the origin is situated in the center of the curvature of the curved cylinder. The direction of flow is perpendicular to the plane of curvature.
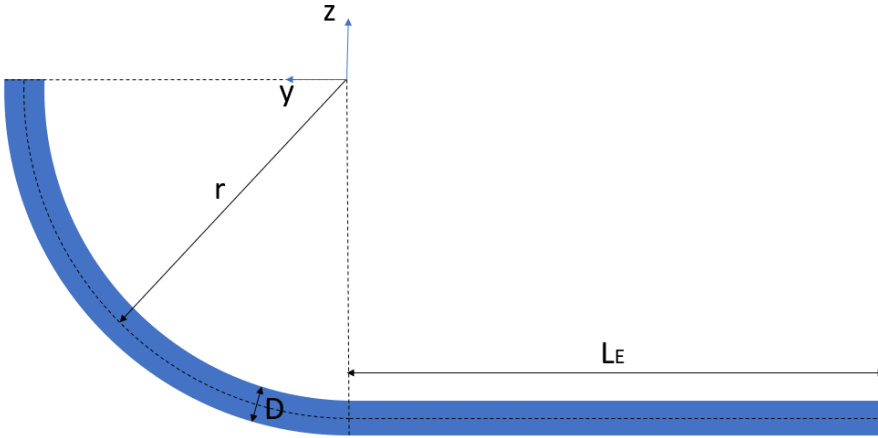
Figure 32: Two dimensional view of curved cylinder

Domain parameters

Domain parameters	
Domain length, L_X	52.5 m
Domain width, L_Y	27.5 m+L_E
Domain height, L_Z	27.5 m
Straight extension, L_E	Variable
Diameter, D	1 m
Radius, r	12.5 m

Flow parameters

Flow parameters	
Flow velocity, U	1 m/s
Density, ρ	1 kg/m^3
Dynamic viscosity ν	Variable

Table 10: Domain and flow parameters for curved cylinder simulations

The domain in curved cylinder simulations was constructed by importing a parasolid model into HEXPRESS, serving as the body of the cylinder (both curved part and straight extension). A box domain was then created around the cylinder surface. The dimensions of the domain were settled based on the knowledge from the previous simulations. It was earlier settled that a domain size of 15 m above and below the cylinder surface was required. Since the radius of curvature is constantly 12.5 m, the dimensions of both L_Y and L_z becomes 12.5 m + 15 m = 27.5 m. The exception is for the simulations where a horizontal extension L_E is attached to the curved cylinder, such that L_Y increases by this amount. Mainly three extensions lengths were simulated: $L_E = 16D$, $L_E = 8D$ and $L_E = 0D$ (no extensions). Boundary conditions are settled based on findings in Section 6. Mirror BC were used for the cylinder end plates.The inlet, bottom face and left wall were set as external BC with Dirichlet conditions of a constant flow velocity u=1, while the outlet was given Neumann BC for velocity components and along with a frozen pressure p = 0. The simulation time step were also for the current simulations chosen as Δt = 0.01.

The mesh in the curved cylinder simulations are generated in the similar manner as for the straight cylinder simulations in HEXPRESS. It is assumed that the final mesh configuration from the grid sensitivity study for the 2D straight cylinder simulations can be applied in the curved cylinder simulations as well. This assumption should hold based on the discussions of White [2006], stating that as long as $\delta \ll$ r the boundary layers equations are still valid for curved surfaces (see Section 2 for further insight). The aspect ratio $\alpha = \frac{\Delta Z_1}{\Delta X_1} = 1$ in order to resolve the flow in the different directions equally. Other than this, the mesh is equivalent to what can be seen in Table 3. An overview of the mesh configuration can be seen in Figure 33, while illustrations of cutting plane views at the cylinder centre along with labeled mesh refinement levels is seen in Figure 34.
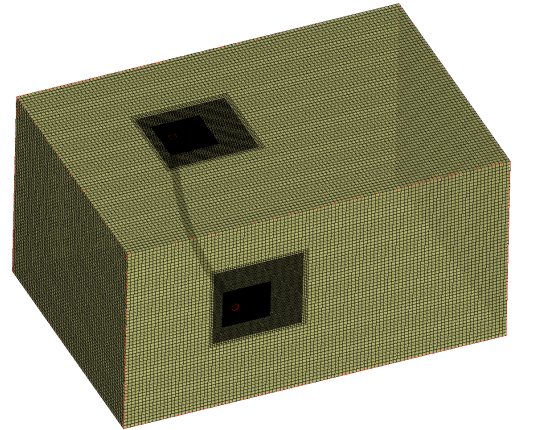
Figure 33: Overview of mesh for curved cylinder simulations

(a) Curved cylinder mesh at x = 0   (b) Close-up view of fine mesh close to curved surface
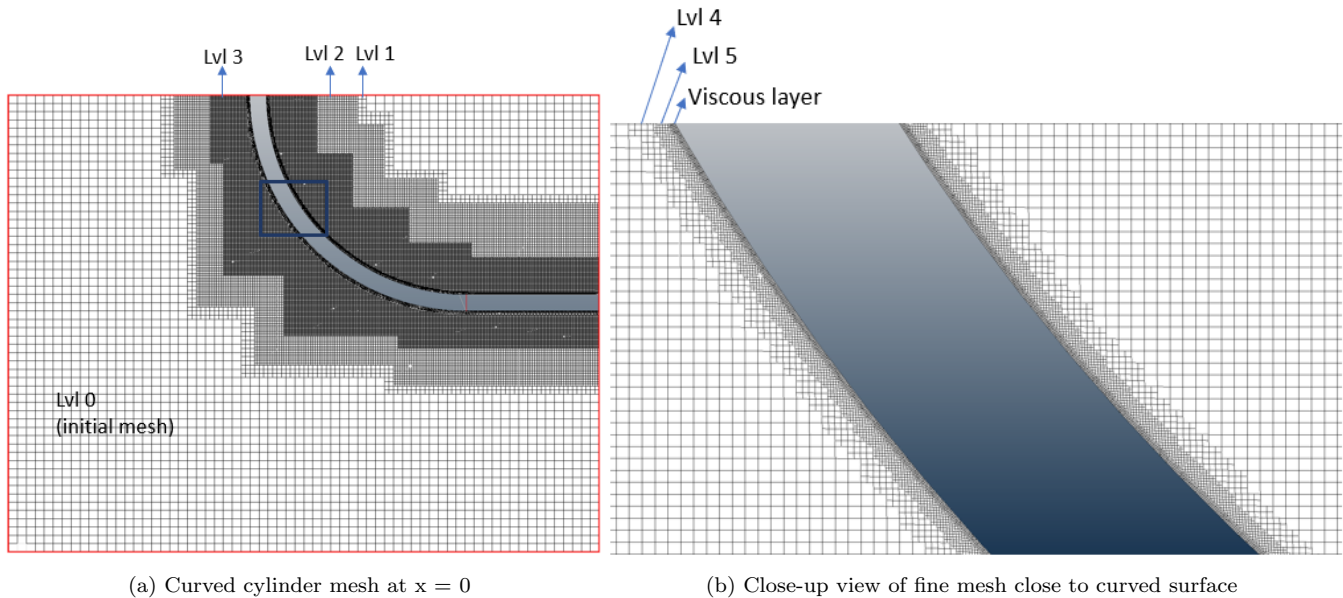
Figure 34: Grid visualization at a cutting plane along the centerline of the curved cylinder. Mesh refinement levels are labeled. Square box marks the position at which the leftmost figure is taken at.

Simulation series:

Two parameters were varied throughout the curved cylinder simulations, namely the Reynolds number and length of extension of the horizontal cylinder. The following cases were run and post processed:

- $L_E = 0D$ extension, Re = 300 (200 s simulation)

- $L_E = 8D$ extension, Re = 300 (100 s simulation)

- $L_E = 16D$ extension, Re = 300 (100 s simulation)

- $L_E = 0D$ extension, Re = 200 (300 s simulation)

- $L_E = 8D$ extension, Re = 200 (300 s simulation)

- $L_E = 16D$ extension, Re = 200 (300 s simulation)

Simulations at Re = 200 were initially run from based on initial conditions U = 1 m/s in the entire domain, however these simulations did not trigger three dimensional vortex structures even after quite long running times. For simulations at Re = 300 however, starting from the equivalent initial conditions, a three dimensional wake develops very rapidly. In order to induce these three dimensional effects for Re = 200, which we know exist for this flow velocity based on previous research, the simulations are modified to have initial conditions equal to the last timestep of the Re = 300 simulations. Discussion on why the three dimensional effects are harder to induce for lower Reynolds numbers for this flow geometry is provided.

In the present discussions, the focus will first be concentrated on the features of the flow development behind the curved cylinder and the potential unique flow features as a result of the cylinder curvature. Following this an analysis of the effect of the straight extension to the curved surface will be provided.

7.2   General flow development and wake formations

In all the curved cylinder simulations, three dimensional vortex shedding of different modes presented themselves with similar properties as was observed for the straight cylinder simulations. The flow development during the simulation the curved cylinder with no extension (L_E=0D) at Re = 200 is presented in the following figures.

(a)

(b)

(c)

(d)
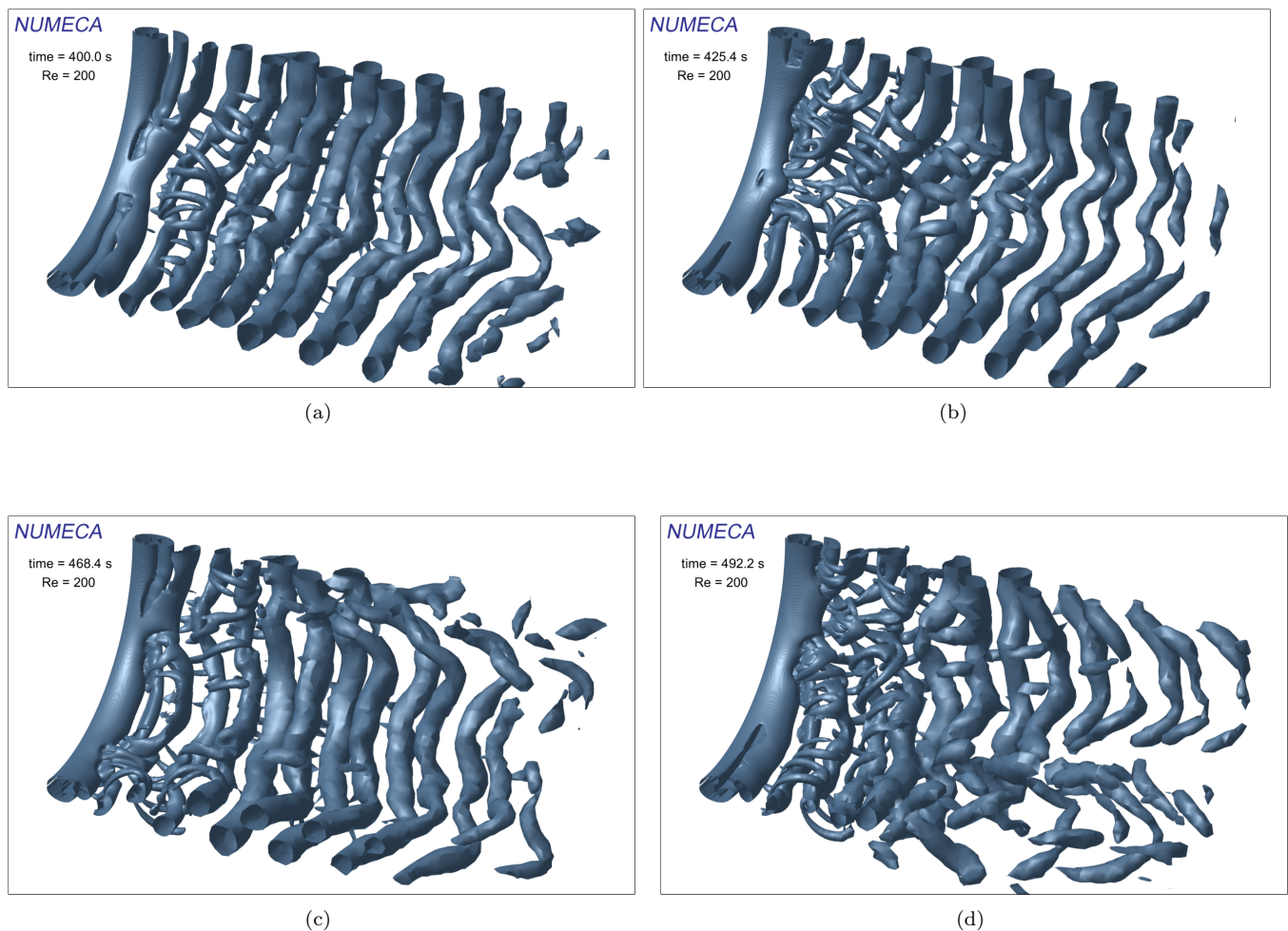
Figure 35: The transitional wake at Re = 200 behind a curved cylinder with no extension at selected time instants during the simulation, displayed by application of surface probes defined by the vortex detecting quantity Q-invariant = 0.01. Specific time instant is seen within each subfigure

From an observational point of view, the wake appears to be quite unstable with changing properties throughout the

simulation. At the first timestep, t = 400.0 s (Figure 35a), mode A has clearly started to develop in the middle part of the curvature, while on the boundaries of the domain the three-dimensional vortices remain absent at this point. There is a passing of a vortex dislocation seen in approximately in the middle of the of the domain at t = 425.4 s (Figure 35b), observed as a discontinuity along the primary vortex filament. Three dimensional vortex shedding seems to be developing close to the upper boundary of the domain at this point, while the lower boundary still shows no sign of mode A secondary vortices. As the flow develops further, at time instant t = 468.4 s (Figure 35c), there seems to be somewhat fewer appearances of secondary vortices along the span. This could be seen in relation to a transition through (bottom value of the long period oscillations in the force history as seen in Figure 38). There is another dislocation close to the upper boundary of the domain at t = 492.2 s (Figure 35d), as well as a knot where several streamwise vortices appear as they "tie" into each other. Oblique vortex shedding is present in all of the time instants displayed in Figure 35 at different locations along the span and occurring at different oblique shedding angles. The figures are still-images taken from the animation which is included on the hard-drive that has been delivered along with the report. The animation gives a better impression of the behaviour and development of the flow in this simulation.

The flow regime developed in the simulation 16D extension seems to be somewhat more stable than what the 0D case. The word stable is used in this context, meaning that the appearance of mode A streamwise vortices appear more regularly across the whole span of the cylinder, both on the curved body and the horizontal extension. There are also no vortex dislocations present in the latter simulation. One possible reason behind these differences observed in the wake of the two cases (no extension compared to 16D extension) is because of the boundary conditions applied. An illustration of the symmetry conditions for the relevant configurations is shown in Figure 36.
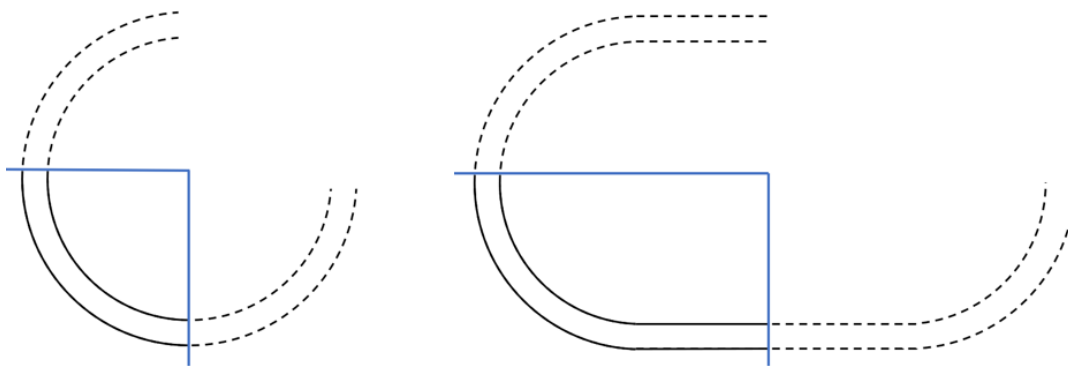
Figure 36: Mirror boundary conditions visualized for domains with no extensions (left) and with a horizontal extension (right)

For the case with no extension, the boundary condition implies that the domain resembles a ring. As a direct result of the curvature, it will not be possible to have an axissymmetric wake with constant wavelengths between the streamwise vortices along both the outer and the inner radius of the body. The instabilities in the flow at Re = 200 "wants" to trigger mode A streamwise vortices at constant wavelengths of 3-4 diameters, but the geometric geometric nature of the ring prohibits this from happening. The streamwise vortices must be suppressed at some

locations along the body, which manifests itself as frequent dislocations along the span. This effect is magnified by the boundary conditions indicating that the curvature extends also outside of the domain. In the simulations with the horizontal extension, these dislocations are likely to happen less frequently due to the "shorter" curvature that the flow is exposed to. This is only an hypothesis that seems plausible from a physical point of view, although there may be other factors involved as well. It should also be mentioned that the simulation using 8D extension actually suppresses mode A along the extension, illustrating that there most probably are other numerical phenomena at play as well.

An animation of the 16D extension case is delivered with the report for comparison with the animation of 0D extension. The length of the animation with the 16D extension is considerably shorter (20s, $\sim$ 4 cycles) than the animation with no extension (100s, $\sim$ 20 cycles). Vortex dislocations and other irregularities might show up if the animation with the 16D extension was longer.

The simulation at Re = 300, for both the 0D, 8D and 16D case, exhibit a more regular shedding regime with clear mode B streamwise vortices regularly spaced at about 1D wavelengths between them. The combined effect of the curvature and symmetry conditions referred are not as dominating for this higher Reynolds number. This is well in agreement with the findings of Leweke and Provansal [1995], who investigated flow past rings as well. The experimental results in this study showed that wake fluctuations become more periodic as the Reynolds numbers is increased throughout the TrW, with a better defined dominating frequency and fewer dislocations. Approaching this from a physical point of view, one reason could be because of the wavelength between the secondary vortices is shorter in mode B than mode A. This leads to fewer dislocations necessary for the flow to remain the axissymetric in the wake as it wants to achieve. If long enough simulations are run at this Reynolds number, it is likely that the occasional appearance of vortex dislocations will occur. Figure 37 shows the wake behind the 0D and te 16D cases at Re = 300, both illustrating clear mode B shedding along the whole span of the cylinder.

(a) 0D extension, Re = 300

(b) 16D extension, Re = 300
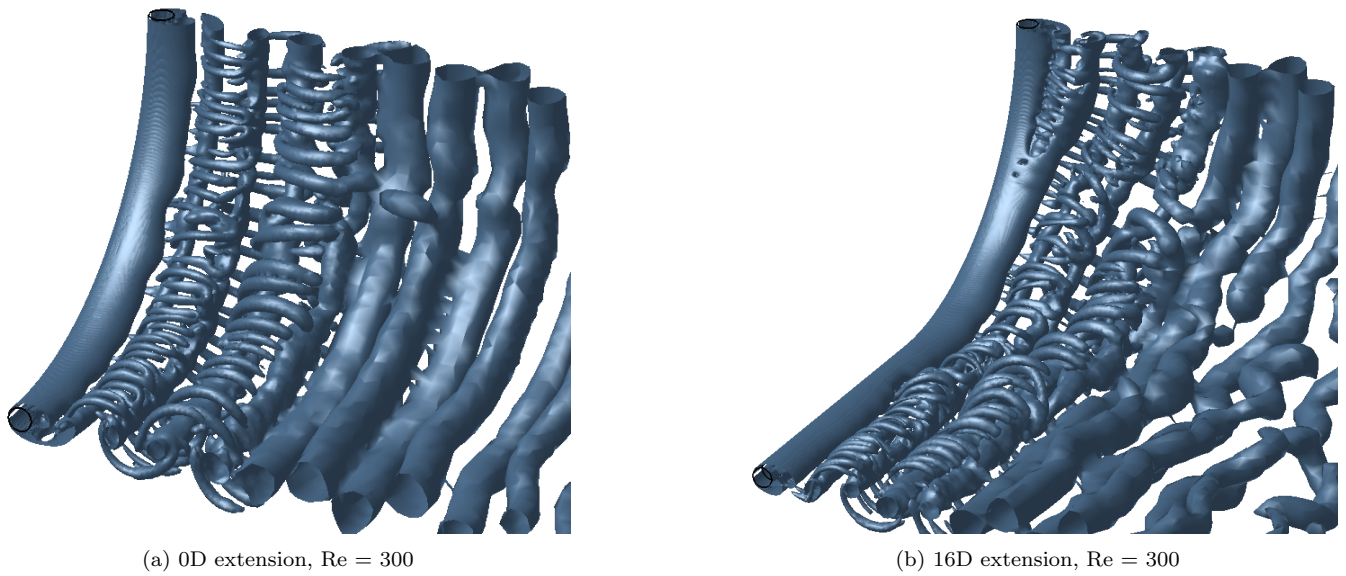
Figure 37: Vortex detection $\lambda 2$ = -0.01 for simulations with no horizontal extension (0D) and 16D extension at Re = 300

7.3 Stability of the simulations

The long period oscillations observed in the force history the straight cylinders discussed in Section 6.5 are present in the simulations of curved cylinder as well. Figure 38 illustrates how the raw force data from the simulations exhibit significant fluctuations in all force directions, F_X, F_Y and F_Z. There seems to be stronger fluctuations for Re = 200 than Re = 300. This could seen in relation to the previous discussions of vortex dislocations and generally more unstable flow regime present in mode A shedding. However, in comparison to the studies of Williamson [1992] and Leweke and Provansal [1995], the dislocations manifest themselves more as instantaneous drops or peaks in a parameter's time history (see example of this in Figure 47). The long-period oscillations clearly seen during the in-line force history after 300 s of simulation are quite different in nature and are most likely influenced by some other numerical factors. The same discussions as for the straight cylinder applies also for the curved cylinder simulations in this regard.

(a) In-line force component

(b) Transverse force components
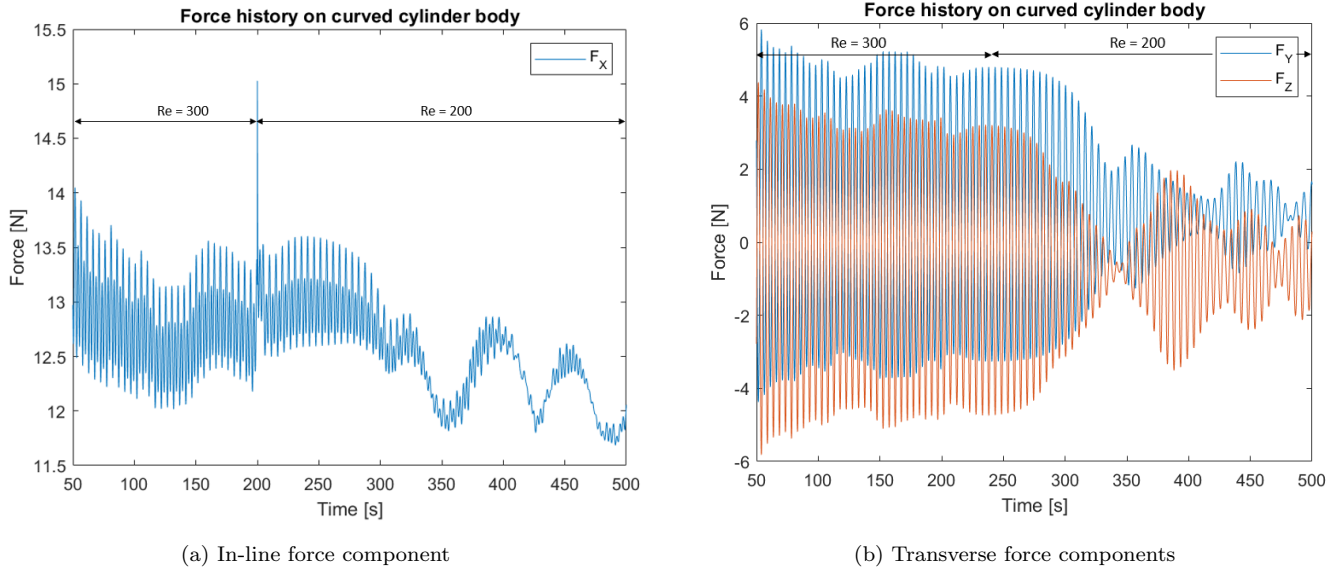
Figure 38: Force histories of Fx, Fy and Fz from 0D simulation at different Reynolds numbers

Since these irregularities are present within all the simulations performed, it is important to be critical to the value of an averaged parameter. For example, the averaged value of the in-line force during some short time interval at 350 s of simulation compared to some short interval at 400 s of simulation (see this in reference to Figure 43a), the mean value will be quite different. As a result, it is crucial to apply long time intervals in order to get more accurate averages. The present simulations performed are in fact not long enough to get completely reliable averages due to the required computational time such extensive simulations would demand. The mean values used in the current analysis should therefore be investigated from a critical point of view, aware of the possible sources of error they may represent.

7.4   Frequency considerations

An important parameter of flow beyond circular cylinders is the Strouhal number. Figure 39 shows the power spectral density (PSD) based on a fast fourier transform (FFT) of the time series based on the streamwise velocity component u measured behind the cylinder, along the span of both the curved and the straight part of the cylinder. All the frequencies in the current set of data are divided by two since the in-line velocity component is oscillating with twice the vortex shedding frequency. The spectrum clearly show the presence of a the dominating frequency along the both the curved and straight cylinder span. A closer inspection of the plot reveals that there is a small step in dominating frequency between the curved cylinder and the horizontal extension. The dominating frequency gradually increases from ∼0.185 to ∼0.193 as you move along the span from the curved part to the horizontal, as indicated by the dotted lines in the plot. This is in qualitative agreement with the study of Leweke and Provansal [1995], stating that the vortex shedding frequency is somewhat higher for straight cylinders than for cylindrical rings, see Figure 10 in Section 3. The explanation for this shift in frequency could be related to the appearances of

57

oblique vortex shedding angles. The findings of Leweke and Provansal [1995] state that oblique shedding is indeed a feature of cross-sectional flow past curved cylinders. Furthermore, the hypothesis can be supported to extent by the mathematical relation between oblique and parallel shedding modes presented in Equation 12 in Section 2.6. The equation yields an oblique-shedding angle ϕ=18.4, which is in the range of typical oblique angles for this Reynolds number presented by Williamson [1988a]. It should be taken into account that Williamson [1988a] studied oblique vortex shedding within the laminar range. There is nevertheless clear cases of oblique vortex observed in the present simulations.
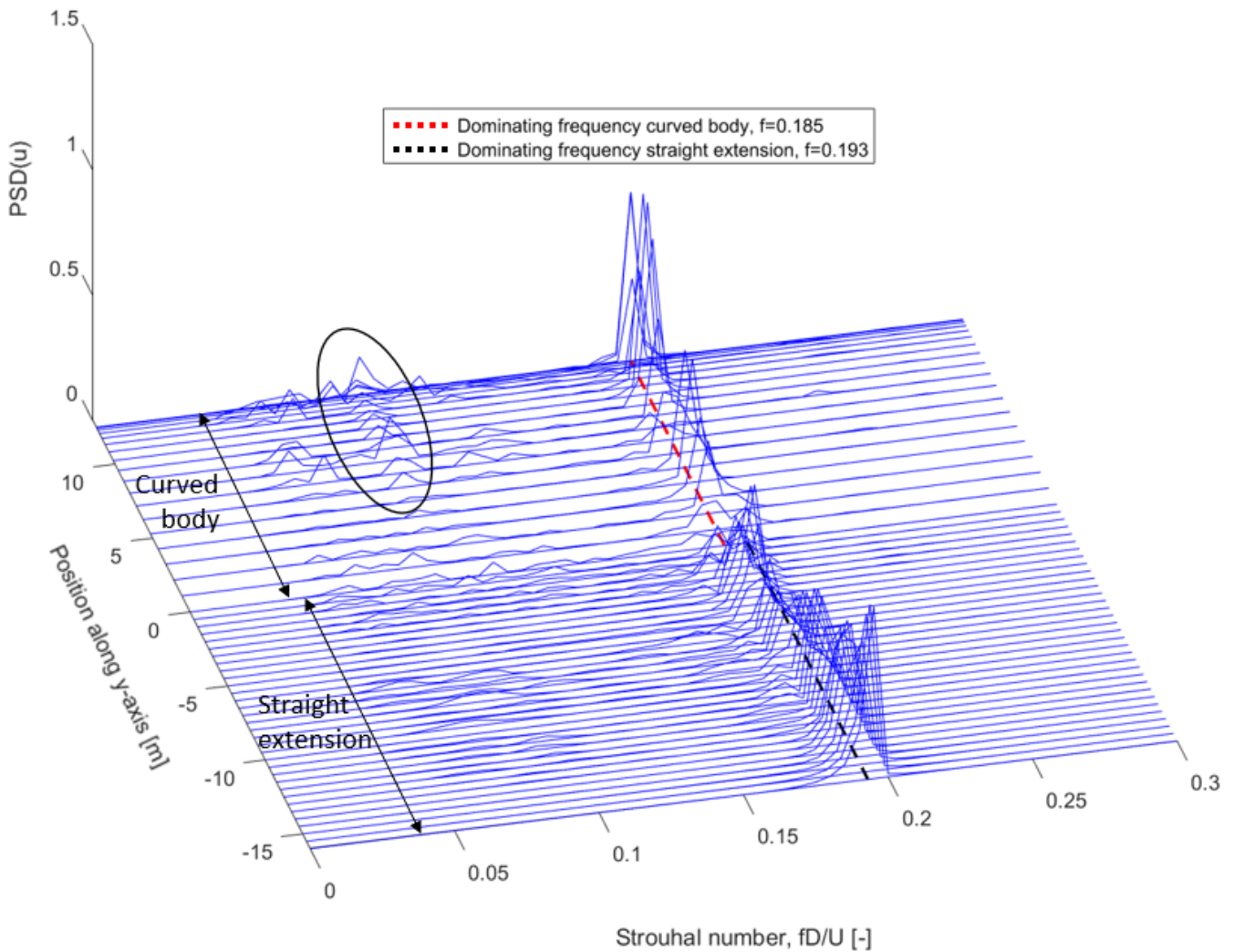
Figure 39: Frequency spectrum of the dominating frequencies in the time series of velocity component u (i.e in the same direction as the flow) from simulation with Re = 200, 16D extension. The velocity is measured at point probes along the span of the curved- and horizontal cylinders at a distance 1D behind the trailing edge. Spectral energy $[\frac{m^2}{s^2 Hz}]$ is measured on the z-axis, dimensionless frequency (Strouhal number) on the x-axis and position along the y-axis of the simulation domain on the y-axis. Position of curved cylinder body and horizontal extension is labeled for clarity.

There is also a significant secondary frequency component along the curved span at St~ 0.1, marked with a circle in Figure 39. These frequencies are most prominent close to the upper domain boundary where there is no extension. The magnitude of the secondary frequency becomes weaker closer to the horizontal extension, and manifests itself more like noise at this point. Along the horizontal extension there is also trace of other frequencies, but not in a significant manner. Some long periods of oscillations are expected based on the known passage of vortex dislocations and other irregularities seen in the force histories, which will appear as low frequent peaks in the PSD. However, the fact that this secondary frequency is much higher close to upper boundary could potentially lead us to believe that the secondary oscillations are related to the curvature present or the mirror boundary conditions applied. The frequency spectra from the straight cylinder simulations in the previous section did not show any clear such secondary frequencies, and it is not described in any earlier experimental studies either. This is clearly not a feature of a flow behind a straight cylinder. A frequency spectrum of similar properties of the curved simulation with no extension is included in the Appendix. There is also a clear secondary frequency in this spectrum. Longer simulations should be performed in order to see whether these secondary frequencies in reality come from low frequent noise or if they actually represent some intrinsic flow feature.

7.5   Pressure and velocity distributions

Pressure and velocity distributions from the various simulations have been studied. These flow parameters exist within every element in the entire 3D domain, so clever solutions as to show the flow development should be applied. One way to visualize these parameters is to use cutting planes perpendicular to the cylinder to see how the parameters changes at different positions across the curved span, and how different length extensions affect these distributions. Cutting planes have been made at angles θ = 0 °, θ = 45 ° and θ = 90 °, where θ is the angle from the upper horizontal boundary as seen in Figure 31. For simplicity, these planes have been numbered in the following discussions as plane 1, plane 2 and plane 3 respectively, as can be seen in Figure 40.
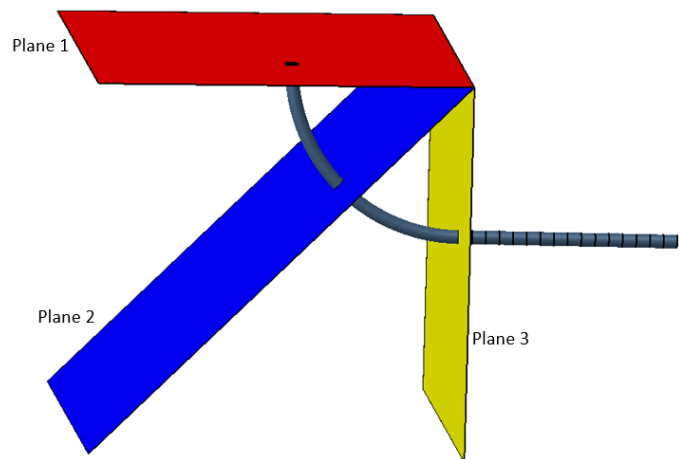
Figure 40: Cutting planes with labels for visualization of pressure and velocity distributions

Only averaged parameters are useful when it comes to comparisons of the flow properties different planes. Therefore, all simulations were run with averaged pressure and velocity fields as output. Figures 41a and 41b show how the mean pressure distribution compare in Plane 1 and Plane 3. At first sight of the two pressure distributions, one might say they appear to be quite similar. The low pressure distribution on plane 3, which is just next to the horizontal extension, seems to be somewhat wider than that of plane 1. Other than that, not much more can be said about the differences between the pressure distributions. The parameters might be more easily studied by numerical

comparison. More plane views of pressure and u-velocity fields from the different simulations can be studied in the Appendix.
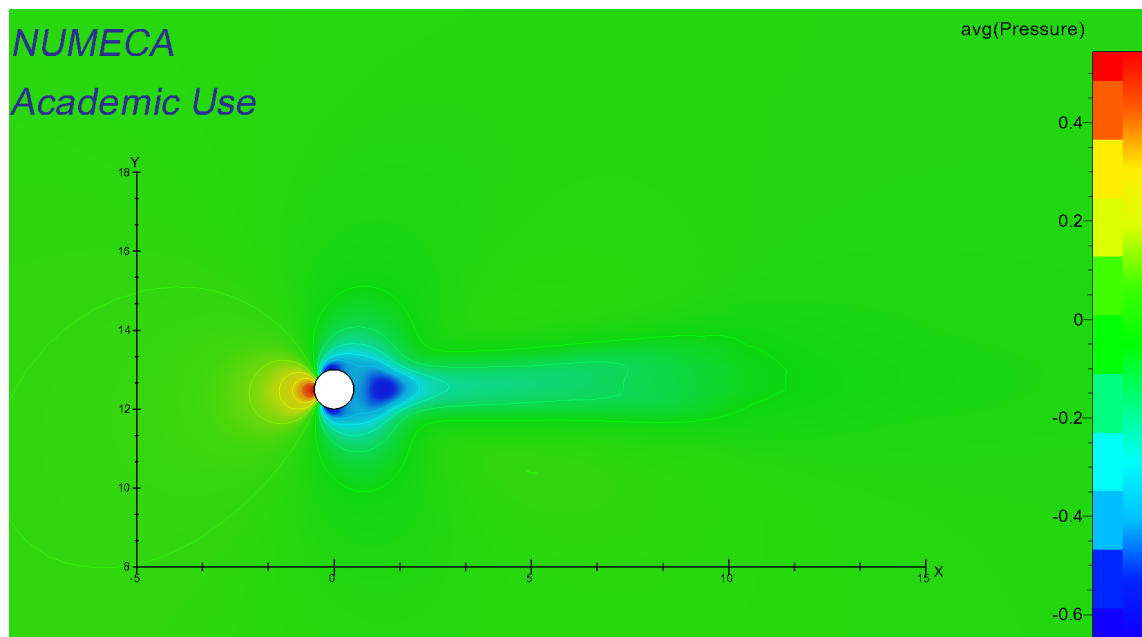
(a) Plane 1, horizontal plane
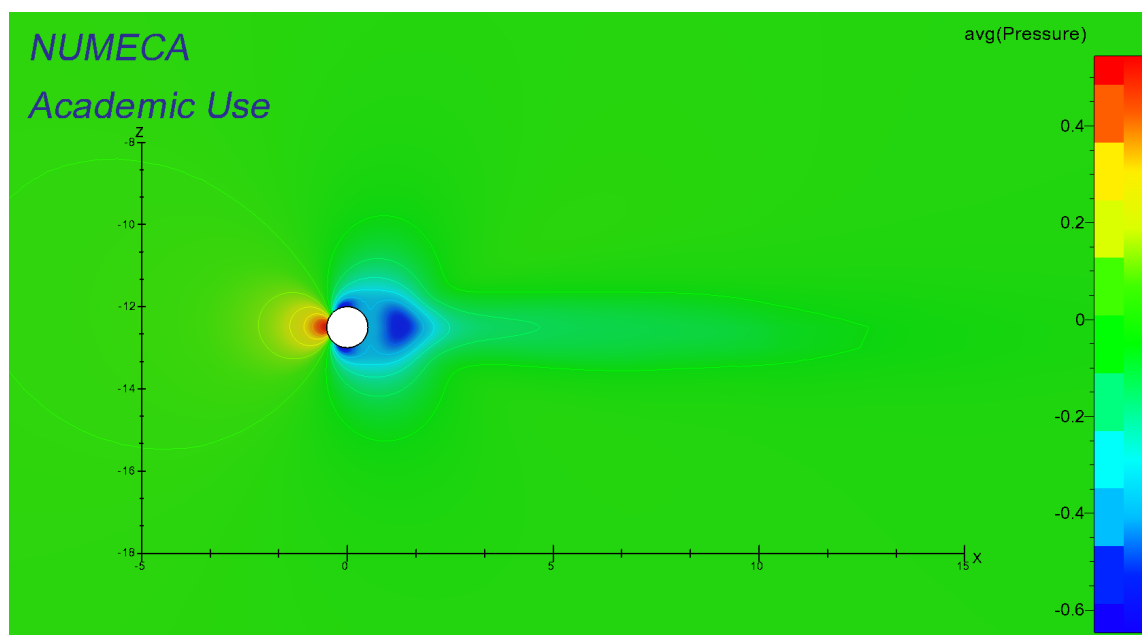
(b) Plane 3, vertical plane

Figure 41: Average pressure distribution at different cutting planes in the domain

In order to provide some further numerical comparison, the pressure and
u-velocity components were collected along a line pointing from the sur-
face of the cylinder and radially outwards in the wake (see Figure 42 for
explanation). This is possible through the use of "Cartesian plots" along
a specified section in CFView. Figure 43 shows how the three simulations
of 0D, 8D and 16D extensions at Re = 200 yields different pressure and ve-
locity distributions along the described section on the boundary between
curved cylinder and extension ("plane 3" according to the illustrations in
Figure 40).
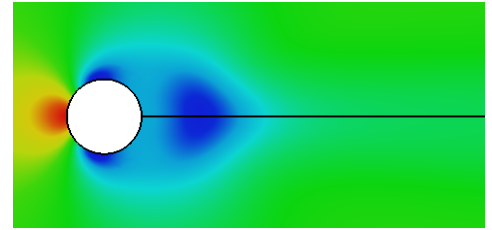
Figure 42: Pressure and velocity param-
eters are collected along a line from the
surface of the cylinder and radially out
into the wake

(a) In-line force component

(b) Transverse force components
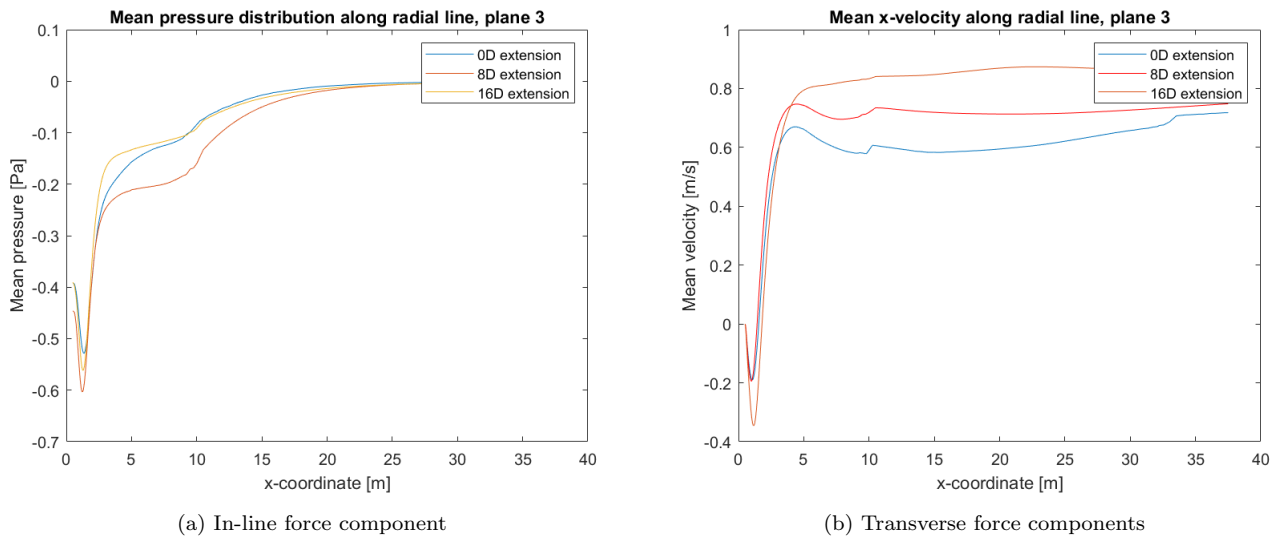
Figure 43: Pressure and u-velocity along a linear line from the surface of the cylinder and radially outwards in the
wake. Comparison between the different simulations of 0D, 8D and 16D extensions in plane 3. See Appendix for
enlarged plots for a closer study

As we can observe from the plots, there are some clear differences both in the near- and far wake regions of the flow.
In the pressure distribution plot, the extensions seem to induce a lower pressure (more negative) in the near wake
just behind trailing edge of the cylinder. The 8D-extension actually has a lower pressure than the 16D extension
according to the plot. About 5 - 10 diameters in the wake behind the cylinder, there are also some clear deviations
between the plots, before they converge together towards the frozen boundary. From the velocity components in
the leftmost plot, the 16D extension simulation seemed to have a larger magnitude of reversed velocity in the near
wake. The far wake also differs in between the three cases, where the simulations including extensions seem to induce
somewhat higher velocity components all the way towards the outlet of the domain.

The results are calculated by taking the mean of the instantaneous results to get comparable results. The earlier discussions regarding the required sampling time in order to get "good enough" averages are also applicable in this context. The simulation time from which the mean pressure and velocity are calculated could arguably be longer in order to get more reliable results. This represents a source of error that should be kept in mind in the analysis of the results. The described observations of the plots in Figure 43 represent some vague trends, but it is somewhat difficult to make any conclusions as to what is actually going on, other than stating the fact that the extension clearly affects the flow features in the wake to some extent.

7.6   Effect of straight extensions on force components

The computed force histories during simulations in FINE/Marine are normally only calculated for specified bodies which are defined in the simulation set up. The initial set up of the present simulations consisted of one horizontal component and one straight extension, meaning you could only monitor the resulting force histories on each of these two sections. It became clear after a few simulations however that a better way of monitoring the computed force on the horizontal extensions was in demand. To approach this problem, the horizontal extensions were divided into individual sub-bodies of lengths of 1 m in HEXPRESS prior to running the simulations. This was done with the intention of studying the generated force components on each individual part of the extension separately, instead of resulting forces on the whole straight extension. The illustration in Figure 44 shows how the extension was split into smaller sections. Extension E1 is the section closest to the curved cylinder, while E16 is the free end on the boundary of the domain. The sections will referenced in this manner in the following discussions.
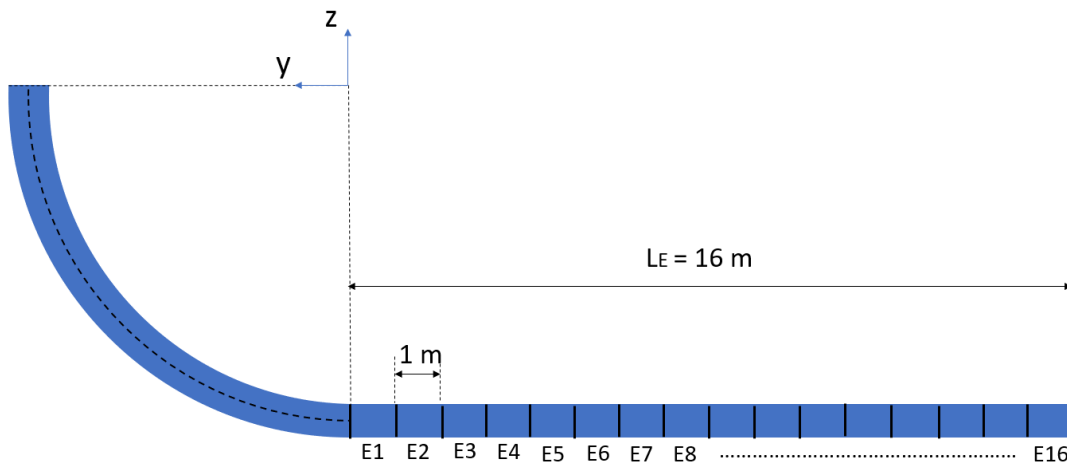
Figure 44: Enumeration of straight extensions split in parts. All extensions have length $E_i =1$ m. Figure uses 16D extension as example, but a similar case with 8D was also run

The most relevant parameters to study when it comes to the extension are the induced drag and lift forces. The drag forces are calculated based on the time history of the force component in x-direction, while the RMS of the lift component is based on the force in the z-direction. Plot 45 show how the forces compare to each other along the two simulations with horizontal extensions 8D and 16D. Tables 11 and 12 provide the numerical values corresponding to

the plot.

(a) Mean drag coefficient

(b) RMS of lift coefficient
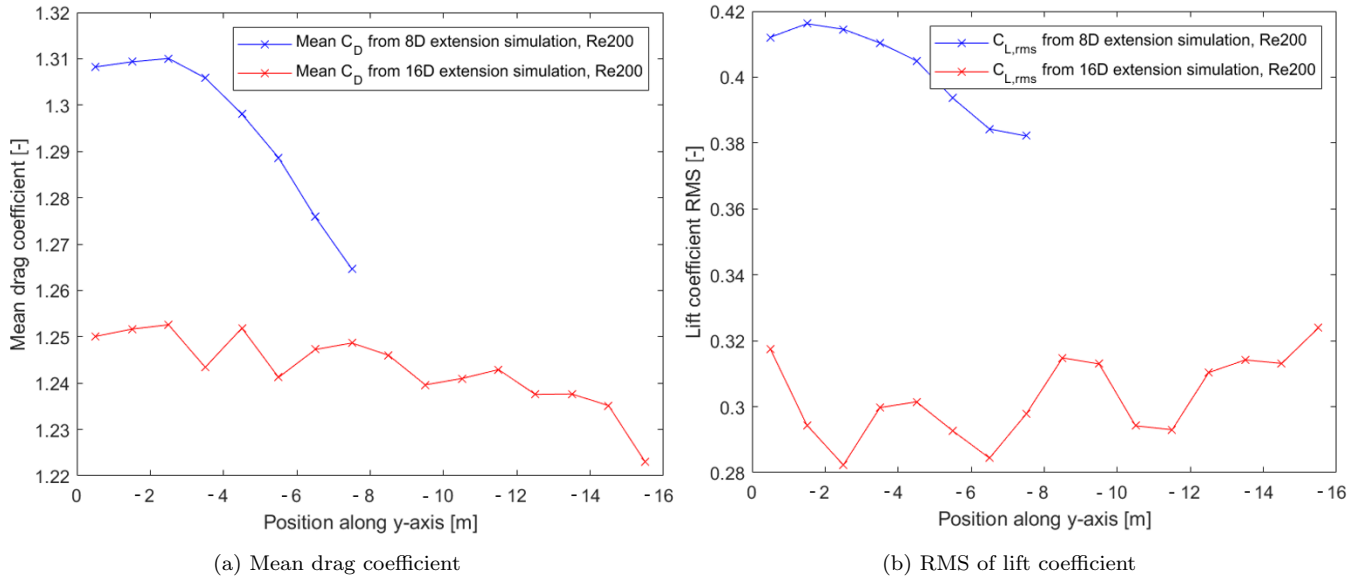
Figure 45: Plot of mean drag coefficients and RMS of lift coefficients along the straight extensions in simulations of respectively 8D and 16D extensions

Extension number	E1	E2	E3	E4	E5	E6	E7	E8	E9	E10	E11	E12	E13	E14	E15	E16
$C_{L,rms}$	0.318	0.294	0.282	0.300	0.302	0.293	0.284	0.298	0.315	0.313	0.294	0.293	0.310	0.314	0.313	0.324
$\overline{C_D}$	1.250	1.252	1.253	1.243	1.252	1.241	1.247	1.249	1.246	1.240	1.241	1.243	1.238	1.238	1.235	1.223

Table 11: Comparison of force components for the straight extensions in simulation 16D

Extension number	E1	E2	E3	E4	E5	E6	E7	E8
$C_{L,rms}$	0.412	0.416	0.415	0.410	0.405	0.394	0.384	0.382
$\overline{C_D}$	1.308	1.309	1.310	1.306	1.298	1.289	1.276	1.265

Table 12: Comparison of force components for the straight extensions in simulation 8D

The first impression you get from studying the plot above is that the two cases generate quite large differences in drag and lift forces across the whole extension. The drag coefficient on E1 is significantly larger for the 8D-extension than it is for the 16D-extension, with about 5 % deviation. The drag coefficient in both simulations is gradually decreasing moving away from the curved cylinder. The slope of curve representing the drag coefficient along the 8D simulation is much steeper, decreasing at a higher rate than that of the 16D simulation. This rapidly decreasing C_D along the 8D extension is probably related to the streamwise vortices being suppressed along the extension during

63

this simulation due to the oblique vortex shedding occuring here. The lift RMS plots show a similar trend, except that the lift actually seems to slightly increase moving away from the curvature in the 16D simulation. The plots illustrate that there are significant differences between the forces along the extensions. Also for these results, the simulations have some level of uncertainty due to short time series from which the results are based upon. As a consequence, the 16D extension would be the preferred choice based on these results (or maybe an even longer extension would be the better alternative) seeing that the force has still not converged towards a constant value towards the free end.

Drag coefficients on curved cylinder body:

The drag forces exerted to the curved cylinder were also monitored. The drag coefficients are however not directly comparable to the drag coefficients of the straight extensions as they have different geometric shapes and are non-dimensionalized by another projected area. The C_D of curved cylinder body between each simulation of 0D, 8D and 16D extension is nevertheless comparable. The general trend that can be seen between the simulations is that the use of vertical extensions seem to reduce the drag force exerted to the curved cylinder. This trend is apparent in for both Re = 200 and Re = 300, where the most significant reduction in drag force happens during the lower Reynolds number with 16D extension. This could again be seen as an effect of the mirror boundary condition applied. If an increased drag coefficient is an intrinsic feature of the curved cylinder cross flow, this effect will be further enhanced if a ring configuration is applied (no extension) rather than a quarter ring (8D and 16D extension). This trend however needs longer simulation time to get a more reliable average in order to be confirmed.

Re = 200			
	L_E=0D	L_E=8D	L_E=16D
C_D	1.295	1.281	1.2560

Re = 300			
	L_E=0D	L_E=8D	L_E=16D
C_D	1.305	1.235	1.2433

Table 13: Drag coefficients on the curved cylinder body from different simulations

7.7 Base pressure variations along cylinder span

One of the parameters regularly used in the comparison of different flow regimes around cylinders is the base pressure coefficient defined in Equation 17 in Section 2. This was also a topic of discussion in straight cylinders, where the computational results came as close as about 3% deviation from the reference values presented by Williamson [1996]. The comparison of base pressure is particularly useful due to the fact that it is made non-dimensional without having to divide it by a cross-sectional area or a transverse length scale, as opposed to drag- and lift coefficients. This makes it easier to compare the flow around the curved cylinder to the straight extensions.

In order to compare the base pressure coefficients, pressure point probes were placed at various positions along the cylinder base on both the curved cylinder surface and the straight extension. Figure 46 relates the probe positions

to the calculated base pressure coefficients for the simulation with a 16D extension at Re = 200. The y-position of the probes as indicated by the x-axis of the plot refers to the position of the probes with respect to the coordinate system of the computational domain (defined in Figure 31 and 32). All values are time-averaged from 300 seconds of simulation (30000 timesteps). A direct comparison to the base pressure coefficient for straight cylinders taken from Williamson [1996] is indicated by the red line. The immediate impression of the plot is that $-C_{pb}$ on the curved cylinder is generally larger than at the straight extension. The apparent trend is that the value of $-C_{pb}$ is decreasing towards the reference value from Williamson [1996] as the distance from the curved part increases. Based on the results from this specific simulation it can appear as though the curved cylinder in cross flow exhibit a larger $-C_{pb}$ (equivalent to a lower base pressure, if the negative sign is not accounted for) than that of the straight cylinder. The curvature seems to affect the straight extension by an increased $-C_{pb}$ for the probes on the straight extension that are positioned close to the curved surface. The probe on the the very end of the straight extension (E16) calculates a value of $-C_{pb}$ which is very close to the reference value for straight cylinders.
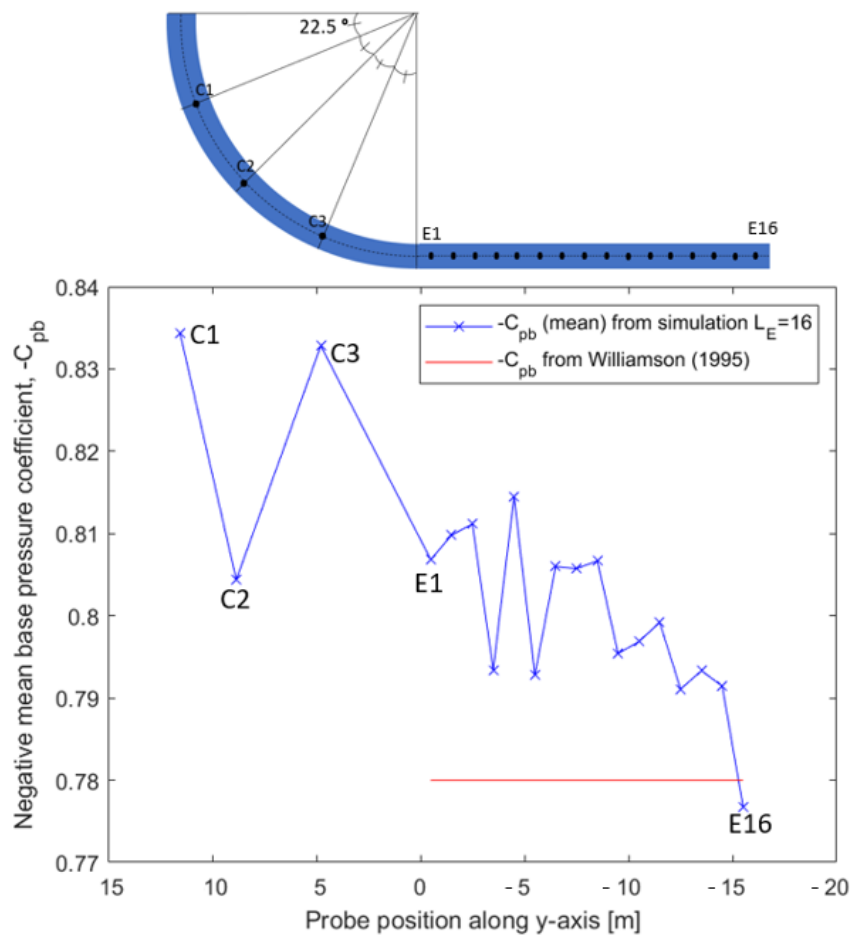
Figure 46: Plot of base pressure coefficients along the span of the curved cylinder and the straight extension at Re = 200. A geometrical figure is included in order to illustrate the positions of the pressure probes in the simulation in relation to the corresponding values in the plot. All base pressure coefficients are taken at the base of the cylinder surface, 180deg from the front

The present trend described for the plot of -C_{pb} i Figure 46 is however based on relatively few probe values. There are only three probes placed on the curved surface, which between them has considerably deviating values of -C_{pb}. This is arguably too few probes to to draw any clear conclusions with respect to base pressure on the curved cylinder. Repeated tests with more probes on the base of the curved surface should be carried out. There is an additional factor of uncertainty due to presence of both long-period oscillations and dislocations of vortex shedding in the time series of the base pressure. Both of these phenomena were discussed previously in the context of resulting forces on the cylinder surface. Knowing that force is merely the integrated value of pressure over a surface, one should expect the same patterns (dislocations, irregularities, etc) in the time series of the base pressure as well. This does indeed occur, as can be seen from Figure 47. The simulation is started from the last timestep of the simulation with Re = 300, in order to induce mode A shedding, according to the procedure described earlier in this section. Approximately at 240 s, there is a very prominent dislocation (also indicated with an error in the figure). This could explain why the mean of -C_{pb} is lower than that of the other two probes on the curved surface (C1 and C2). Figure 47 also illustrates that the simulation has not stabilized, further underlining the fact that there is uncertainty related to the data.
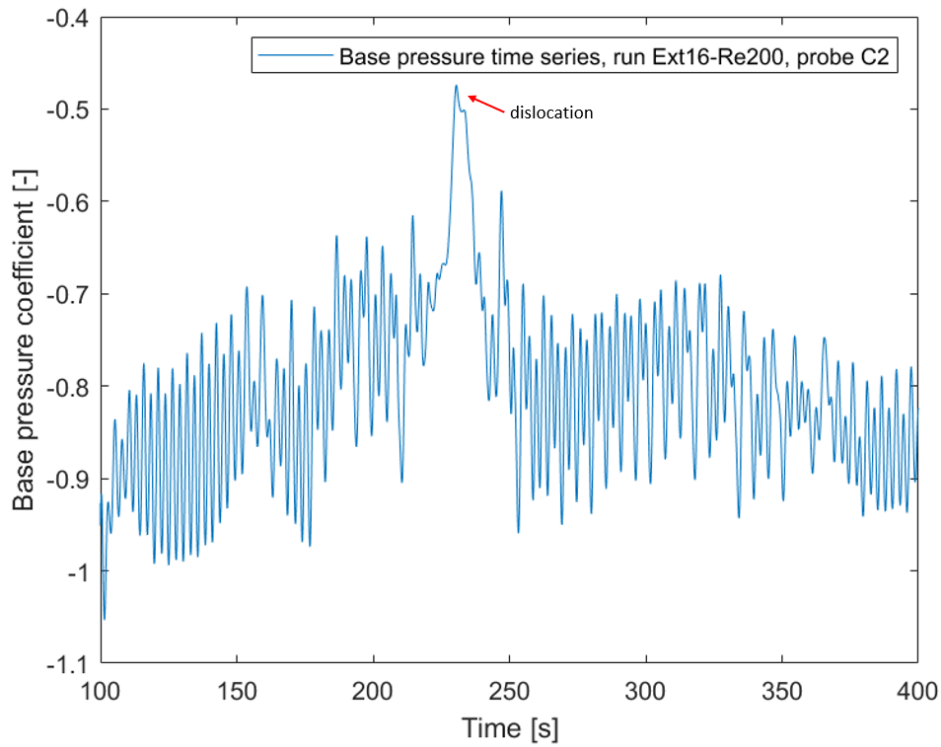
Figure 47: Time series of base pressure coefficient at C2

7.8   Summary and suggestions to further work

In these curved cylinder cross-flow simulations, the main focus has been to explore how the curvature affect the flow compared to straight cylinder simulations, as well as investigations of the importance of length extensions. Several flow parameters have been discussed and compared to other simulations in order to shed some light on influencing factors to the flow development. The results from the computations gives an overall impression that the wake formation and general flow development is quite similar to that of the straight cylinder simulations. Both mode A and mode B shedding was detected at the relevant Reynolds numbers. Mode A seemed to exhibit more unsteadiness, likely triggered by both the curvature and the mirror boundary conditions applied. The horizontal extensions seemed to have a damping effect on these fluctuations during mode A, reducing the frequency of occurrence of dislocations. Vortex shedding frequency and drag coefficients also appear to be somewhat influenced by the curvature and by the inclusion of straight extensions.

The direct result of the chosen symmetry boundary condition in the present simulation is that the domain is mirrored. The discussion of whether to include extensions or not, and how long the extensions should be, boils down to a question of what type of flow configuration is in demand. The choice of boundary conditions in this configuration must be done with respect to the practical applications it should be used for. In the context of flexible marine risers, either quarter-rings or half-rings are the models that closest represent reality. For this purpose it would preferred to include straight extensions to the curved body.

Some concluding recommendations of possible improvements of curved cylinder simulations:

- Longer simulations should be run to get more reliable averages. The described unsteadiness in the simulations, especially during mode A shedding, introduces sources of error to almost all flow parameters, making the comparison to other simulations somewhat unreliable. Some further attempt could also be made to investigate the origin of the fluctuations in the force time histories.

- The applied mesh during the current curved cylinder simulations is equivalent to the mesh composition of the earlier straight cylinder simulations. Due to the little existing research on curved cylinder cross-flow, the wake could potentially exhibit certain flow phenomena we are not aware of at this stage, which could be influenced by the mesh configuration. A more thorough convergence study should be performed to ensure reliable mesh that resolves all flow phenomena.

- Different radius of curvatures could be investigated. This would for example illustrate more clearly the effect of curvature on mode A wake development.

- At this point, it is not certain that a 16D extension is sufficient. Even longer extensions, 24D for example, could be utilized to see if there is a more clear convergence in for example the resulting forces on the straight cylinder edges.

8 Conclusion

This thesis presents the development and results of a numerical investigation on the three-dimensional viscous flow of around a straight circular cylinder and a curved circular cylinder in cross-flow performed in the CFD-software FINE/Marine. Domain and mesh configurations were created in HEXPRESS, the applied flow solver was ISIS-CFD, while post-processing and flow visualization was done in CFView. All these three software systems together form the GUI of FINE/Marine. The present work on a curved cylinder in cross-flow represents one of the first numerical studies that has been performed on this configuration. The main objective is therefore to explore the current flow development and provide some preliminary characterizations of the transitional wake regime for this set-up. The analysis includes some recommendations for computational domain with respect to possible utilization of length extensions to suppress potential free-end effects.

Simulations of the widely researched flow case of a straight cylinder was initially performed in order to obtain experience in FINE/Marine before performing simulations of more complex geometry. Uniform inflow at Re = 200 and 300 was considered, revealing the distinctive transitional wake regimes of mode A and mode B within the respective simulations. Cylinder lengths of 4D, 8D and 12D were tested. The three-dimensional flow features were successfully initiated in the two shortest configurations, but only in the 12D-case the streamwise vortices were generated in a complete manner making it the preferred choice of cylinder length. The mesh resolution in the spanwise direction was found to successfully initiate three-dimensional flow features for even in the coarsest resolution that was adapted. Furthermore the refinement level of the near wake region was found to be important in order to successfully capture three-dimensional streamwise vortex formations downstream of the cylinder. A special case of numerical instabilities were present in all simulations performed, manifesting itself as long period oscillation noise in the force time series. This introduces some error to the calculations of mean flow parameters. The source of these instabilities was not found, and long simulation times are recommended in order to get more reliable averages. The present straight cylinder computations nevertheless provided numerical values of St, C_D and C_{pb} in close agreement with the experimental values obtained by Williamson [1996].

The curved cylinder domain was modelled as a quarter ring with a radius of curvature of 12.5 m and a diameter of 1 m. Straight extensions to the curved body of lengths 8D and 16D were included in some simulations. The incoming flow was directed perpendicular to the axis of curvature, investigated at Re = 200 and Re = 300. The same characteristic transitional wake regime and the two modes A and B present in the straight cylinder simulations were observed for the respective Reynolds numbers in the curved cylinder computations as well. The simulations at Re = 200 proved to quite robust to instabilities in the flow, making the initiation of three dimensional streamwise vortex structures of mode A more difficult to achieve. It is recommended that simulations are started from a perturbed initial condition in order to trigger three dimensional streamwise vortex structures. The present simulations at Re = 200 were started from the last timestep of the equivalent Re = 300 simulation in order to let the Mode A develop more easily. Moreover, vortex dislocations seemed to occur more frequently during mode A shedding (Re = 200) than it did in mode B (Re = 300). Horizontal extensions seem to reduce the amount of dislocations to some extent. The curvature of the cylinder is most likely an amplifying factor to the occurrence of dislocations. Some arguments are presented that the symmetry boundary conditions applied are enhancing this effect.

The effect of length extension were evaluated by comparison of drag coefficients along the span of the cylinder. There was a clear tendency of decreasing drag force along the extension moving away from the curved cylinder body. The decreasing drag force did not seem to converge towards a final value towards the end of the extension, and so it is recommended to investigate even longer extensions. The drag coefficient on the curved body was also measured and compared between the simulations with no extension, 8D extension and 16D extension. The inclusion of the extension seemed to reduce the drag force on the curved cylinder significantly. Another difference observed between the curved cylinder and the corresponding extension was a reduced dominating vortex shedding frequency along the curved span compared to the the straight extension. It is believed that this could be an intrinsic feature of the curved geometry, as indicated by the experimental studies by Leweke and Provansal [1995].

Several aspects of this curved cylinder cross-flow configuration require further investigations to confirm the tendencies observed in the present simulations. Different radius of curvatures is one feature that could potentially reveal further the direct effect of the curvature in this cross-flow configuration. In addition other Reynolds numbers within the transitional wake regime could be tested. It is nevertheless believed that the present simulations and results can contribute to a wider resolution of problem, forming a foundation for future work and knowledge within the field.

List of Figures

List of Tables

References

D Barkley and RD Henderson. Three-dimensional floquet stability analysis of the wake of a circular cylinder. *Journal Of Fluid Mechanics*, 322:215–241, 1996. ISSN 0022-1120.

P W Bearman and M Takamoto. Vortex shedding behind rings and discs. *Fluid Dynamics Research*, 3(1-4):214–218, 1988. ISSN 0169-5983.

John M. Cimbala Cengel, Yunus A. Fluid mechanics - fundamentals and applications. *McGraw-Hill*, 2014.

Odd M Faltinsen. Sea loads on ships and offshore structures. *Cambridge University Press*, 1990.

J. P. Gallardo, B. Pettersen, and H.I. Andersson. Effects of free-slip boundary conditions on the flow around a curved circular cylinder. *Computers and Fluids*, 86:389–394, 2013. ISSN 0045-7930.

J.P. Gallardo, H.I. Andersson, and B. Pettersen. Turbulent wake behind a curved circular cylinder. 742:192–229, 2014. ISSN 0022-1120.

Detlev Gerich and Helmut Eckelmann. Influence of end plates and free ends on the shedding frequency of circular cylinders. *Journal of Fluid Mechanics*, 122:109–121, 1982. ISSN 0022-1120.

J. H. Gerrard. The wakes of cylindrical bluff bodies at low reynolds number. *Philosophical Transactions of the Royal Society of London. Series A, Mathematical and Physical Sciences (1934-1990)*, 288(1354):351–382, 1978. ISSN 0080-4614.

Francis R. Hama. Progressive deformation of a perturbed line vortex filament. *Physics of Fluids*, 6(4):526–534, 1963. ISSN 0031-9171.

F. Jiang, B. Pettersen, and H. I. Andersson. Influences of upstream extensions on flow around a curved cylinder. *European Journal of Mechanics / B Fluids*, 67:79–86, 2018. ISSN 0997-7546.

F. Jiang, B. Pettersen, and H.I. Andersson. Turbulent wake behind a concave curved cylinder. *Journal of Fluid Mechanics*, 2019.

J. Jung, S. Oh, B. Nam, B. Park, Y. Kwon, and D. Jung. Numerical study on flow characteristics around curved riser. = *Journal of ocean engineering and technology*, 33(2):123–130, 2019. ISSN 1225-0767.

G. E. Karniadakis and George S. Triantafyllou. Three-dimensional dynamics and transition to turbulence in the wake of bluff objects. *Journal of Fluid Mechanics*, 238(1):1–30, 1992. ISSN 0022-1120.

T Leweke and M Provansal. The flow behind rings - bluff-body wakes without end effects. *Journal Of Fluid Mechanics*, 288:265–310, 1995. ISSN 0022-1120.

H. Lomax, T.H. Pulliam, and D.W. Zingg. Fundamentals of computational fluid dynamics, 2001.

Eckart Meiburg. *Vortex Methods: Theory and Practice*, volume 44. Society for Industrial and Applied Mathematics, Philadelphia, 2002.

A. Miliou, A. De Vecchi, S. J. Sherwin, and J. M. R. Graham. Wake dynamics of external flow past a curved circular cylinder with the free stream aligned with the plane of curvature. *Journal of Fluid Mechanics*, 592:89–115, 2007. ISSN 0022-1120.

NUMECA. Numeca online documentation platform. *https://portal.numeca.be/docs/FINEMarine/UserGuide*.

Md Mahbubar Rahman, Md. Mashud Karim, and Md Abdul Alim. Numerical investigation of unsteady flow past a circular cylinder using 2-d finite volume method. *Journal of Naval Architecture and Marine Engineering*, 4(1), 2008. ISSN 1813-8535.

A. Roshko. On the development of turbulent wakes from vortex streets. *National Advisory Committee for Aeronautics*, 1953.

H. Tennekes and J. L. Lumley. A first course in turbulence. 1972.

M. Thompson, K. Hourigan, and J. Sheridan. Three-dimensional instabilities in the wake of a circular cylinder. *Experimental Thermal and Fluid Science*, 12(2):190–196, 1996. ISSN 0894-1777.

D. J. Tritton. Experiments on the flow past a circular cylinder at low reynolds numbers. *Journal of Fluid Mechanics*, 6(4):547–567, 1959. ISSN 0022-1120.

Frank. M White. Viscous fluid flow. *McGraw-Hill*, 2006.

C. H. K. Williamson. Defining a universal and continuous strouhal–reynolds number relationship for the laminar vortex shedding of a circular cylinder. *Physics of Fluids*, 31(10), 1988a. ISSN 00319171.

C. H. K. Williamson. The existence of two stages in the transition to three-dimensionality of a cylinder wake. *Physics of Fluids*, 31, 1988b. URL `http://handle.dtic.mil/100.2/ADA205539`.

C.H.K. Williamson. The natural and forced formation of spot-like vortex dislocations in the transition of a wake. *Journal Of Fluid Mechanics*, 243:393–+, 1992. ISSN 0022-1120.

C.H.K. Williamson. Three-dimensional wake transition. *Journal Of Fluid Mechanics*, 328:345–407, 1996. ISSN 0022-1120.

M.M Zdravkovich. Flow around circular cylinders : a comprehensive guide through flow phenomena, experiments, applications, mathematical models, and computer simulations. vol. 1 - fundamentals, 1997.

Appendices

A   Additional plots, straight cylinder simulations

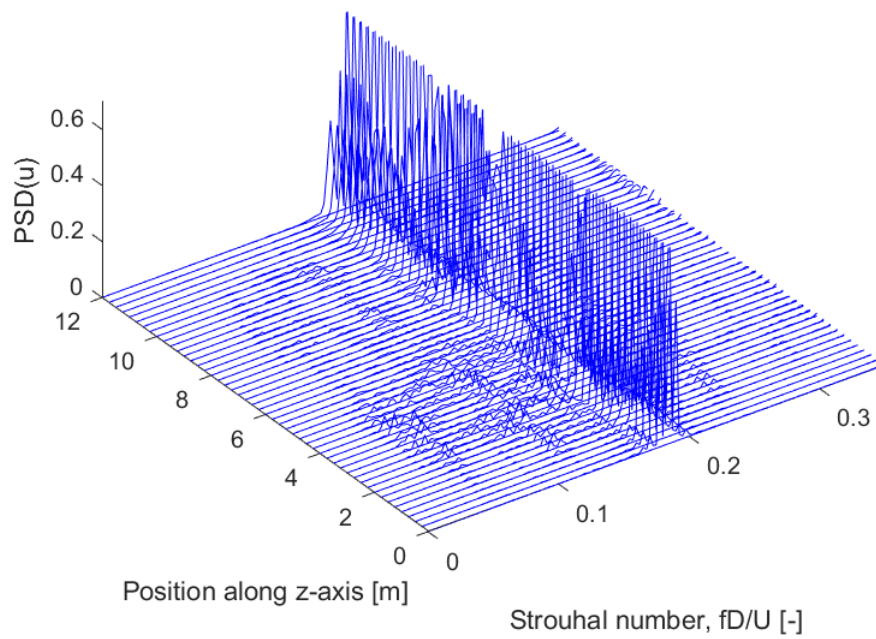### A.1   Frequency spectra

Figure 48: Frequency spectrum from the time series of u-velocity component, L_Z=12D simulation at Re = 200

B   Additional plots, curved cylinder simulations

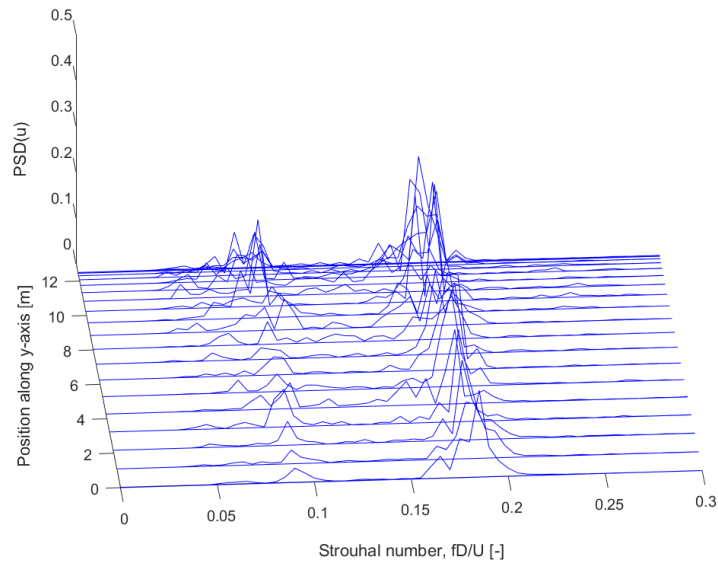## B.1   Frequency spectra, curved cylinder simulations

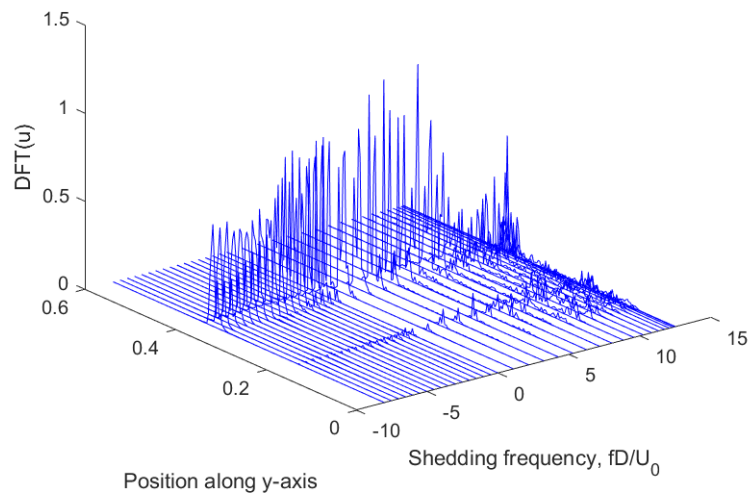Figure 49: Frequency spectrum from the time series of u-velocity component, L_E=0D simulations, Re = 200

Figure 50: Frequency spectrum from the time series of u-velocity component, L_E=0D simulations, Re = 200.The frequency component was not divided by 2 in this plot, like it has been for the other displayed frequency spectra in the report

B.2   Pressure distributions on cutting planes

For references to labelled cutting planes, see Figure 40 in Section 7.
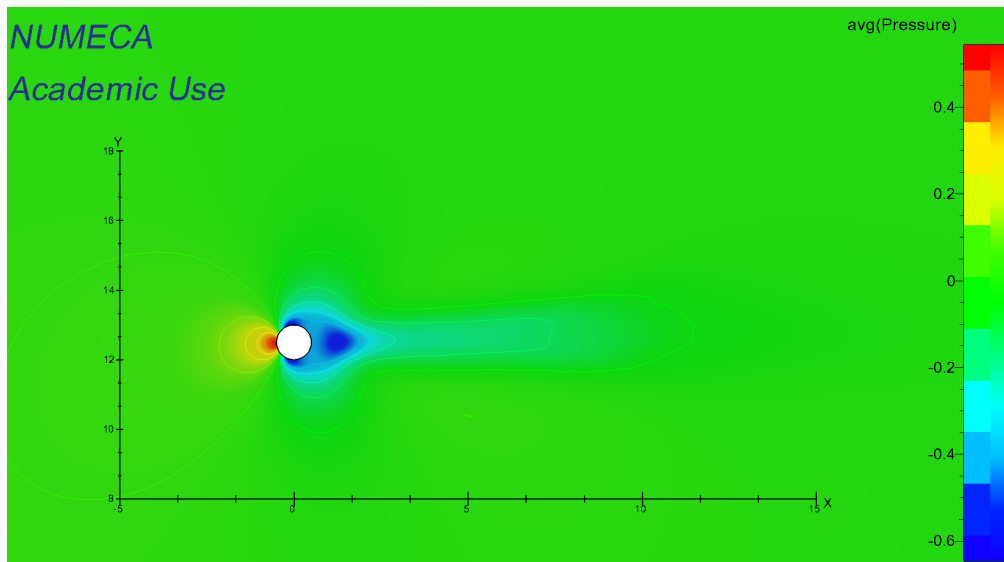
Figure 51: Average pressure distribution in cutting plane 1, 16D simulation Re = 200
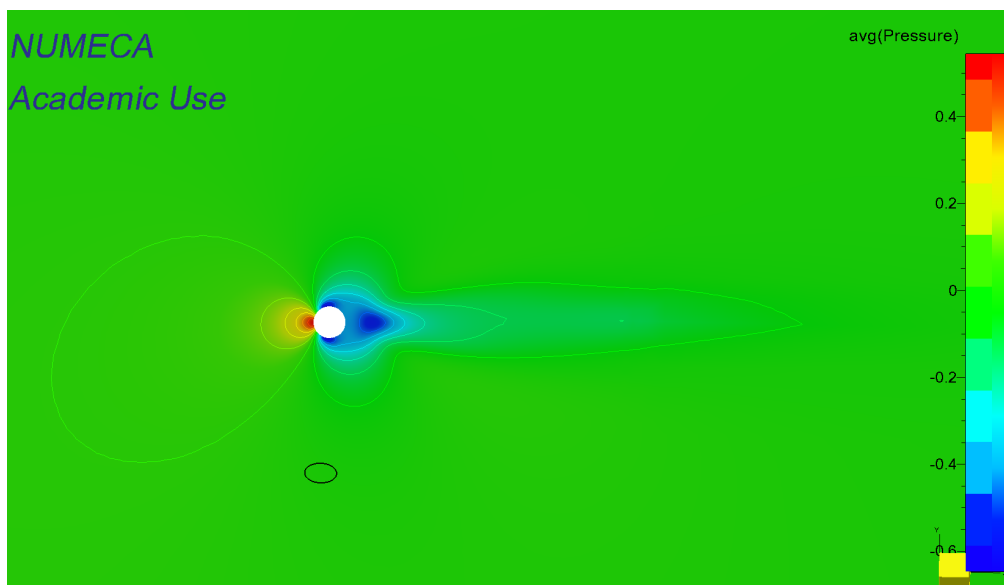
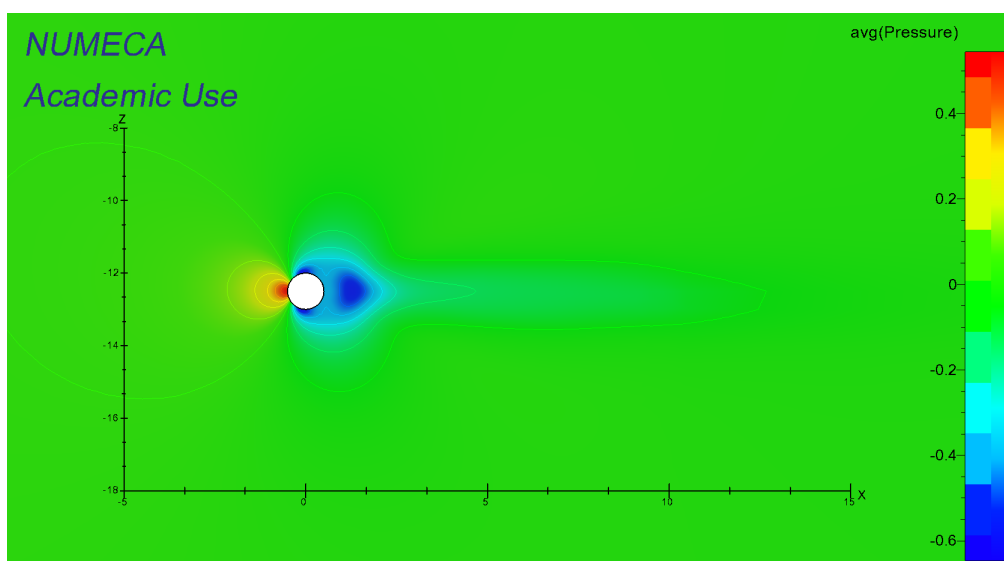Figure 52: Average pressure distribution in cutting plane 2, 16D simulation Re = 200

Figure 53: Average pressure distribution at cutting plane 3, 16D simulation Re = 200
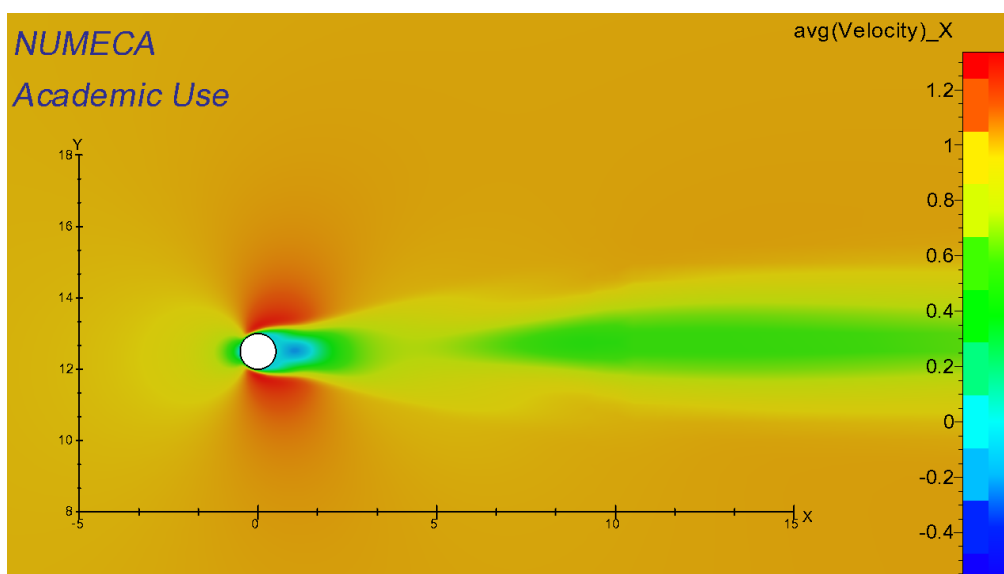
B.3   Velocity distributions on cutting planes

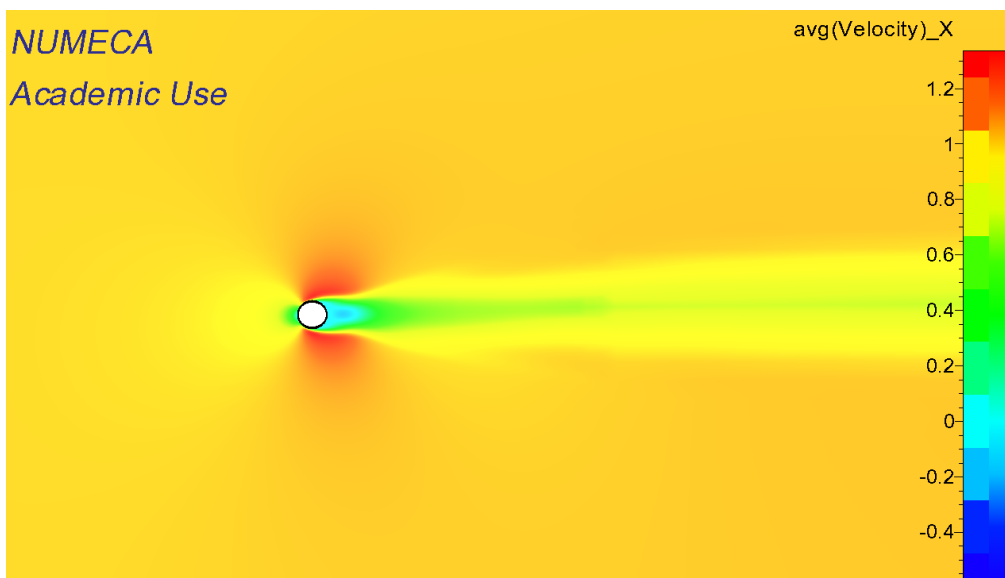Figure 54: Average velocity distribution at cutting plane 1, 16D simulation Re = 200

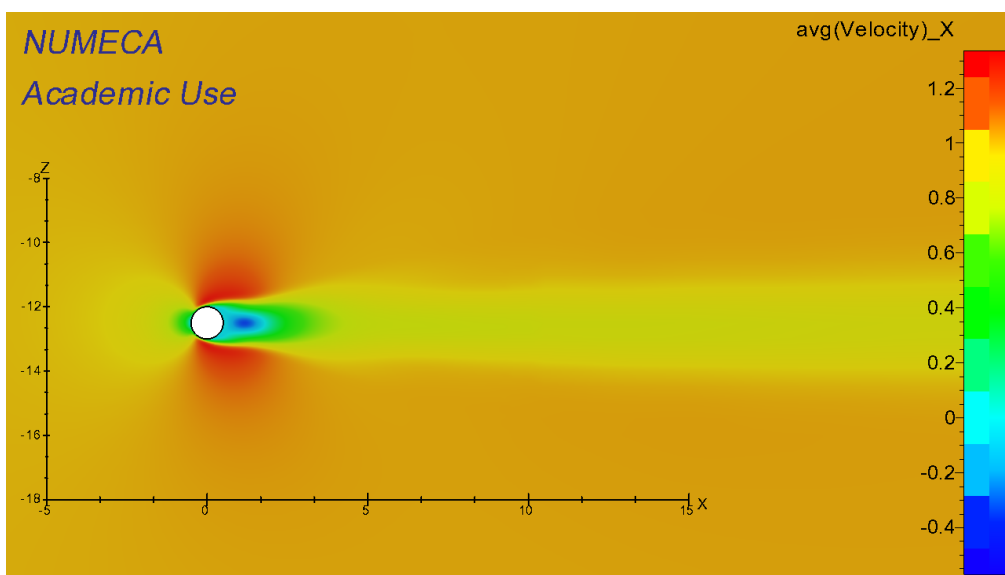Figure 55: Average velocity distribution at cutting plane 2, 16D simulation Re = 200

Figure 56: Average velocity distribution at cutting plane 3, 16D simulation Re = 200